

A Comparison of Two Acoustic Techniques for the Measurement of Bubble Distributions in the Ocean

by

Victor Yi-Xin Mao

B.Eng., Shanghai Jiaotong University, Shanghai, China, 1982

A Thesis Submitted in Partial Fulfillment of the
Requirements for the Degree of

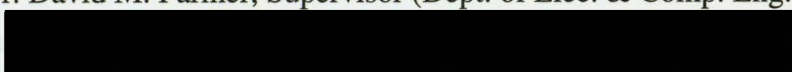
MASTER OF APPLIED SCIENCE


in the Department of
Electrical and Computer Engineering

We accept this thesis as conforming
to the required standard

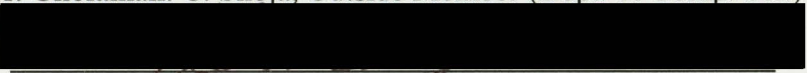


Dr. David M. Farmer, Supervisor (Dept. of Elec. & Comp. Eng.)


Dr. Peter F. Driessen, Supervisor (Dept. of Elec. & Comp. Eng.)


Dr. Jens Bornemann, Departmental Member (Dept. of Elec. & Comp. Eng.)


Dr. Gholamali. C. Shoja, Outside Member (Dept. of Comp. Sci.)


Dr. N. Ross Chapman, External Examiner (School of Earth & Ocean Sci.)

© Victor Yi-Xin Mao, 1995

UNIVERSITY OF VICTORIA

*All rights reserved. This thesis may not be reproduced
in whole or in part by mimeograph or other means,
without the permission of the author.*

Supervisors: Dr. David M. Farmer and Dr. Peter F. Driessen

ABSTRACT

This thesis undertakes part of the work of developing a novel system consisting of an acoustical resonator sensor and a sound speed sensor for measuring bubble populations in the water. The principles of the sound speed sensor and the acoustical resonator are presented. To estimate sound speed anomaly, which can be used to infer bubble populations in bubbly water, some data processing techniques are used and prove to be very effective. Besides presenting a series of laboratory tests of the instrumentation, a successful field experiment conducted in the ocean is reported, in which the newly developed instrument was used. The results obtained from both sensors are compared. As one of the most important contributions of this thesis, a clear analysis has been given of the propagation of a short acoustical pulse in bubbly water. Some new equations are derived, which provide a useful theory to improve the accuracy of bubble population estimates. Field results are interpreted with the aid of the theory.

Abstract

iii

Examiners

Dr. David M. Farmer, Supervisor (Dept. of Elec. & Comp. Eng.)

Dr. Peter F. Driessen, Supervisor (Dept. of Elec. & Comp. Eng.)

Dr. Jens Bornemann, Departmental Member (Dept. Elec. & Comp. Eng.)

Dr. Gholamali C. Shoja, Outside Member (Dept. of Comp. Sci.)

Dr. N. Ross Chapman, External Examiner (School. of Earth & Ocean Sci.)

Table of Contents

Glossary of Terms

List of Symbols

List of Tables

List of Figures

Acknowledgments

1 Introduction

1.1 Bubbles in the Ocean

1.2 Historical Background

1.2.1 Acoustical Attenuation

1.2.2 Acoustical Backscatter

1.2.3 Bubble Trapping

1.2.4 Photographic Techniques

1.3 Acoustical versus Optical Techniques

1.4 The Thesis Work

2 Underwater Sound Propagation	9
2.1 Bubble Resonance	10
2.2 Damping	11
Table of Contents	16
2.3.1 Sound Speed in Bubbly Water	16
2.3.2 Sound Speed in Bubble-free Water	19
2.4 Wood's Theory	20
3 Acoustical Resonator Theory	22
Abstract	ii
3.1 Total Scattering Cross Section	22
Table of Contents	iv
Glossary of Terms	viii
List of Symbols	ix
List of Tables	xii
List of Figures	xiii
Acknowledgments	xviii
1 Introduction	1
1.1 Bubbles in the Ocean	1
1.2 Historical Background	2
1.2.1 Acoustical Attenuation	3
1.2.2 Acoustical Backscatter	5
1.2.3 Bubble Trapping	6
1.2.4 Photographic Techniques	6
1.3 Acoustical versus Optical Techniques	7
1.4 The Thesis Work	7

2 Underwater Sound Propagation	9
2.1 Bubble Resonance	10
2.2 Damping	11
2.3 Sound Speed in the Water	16
2.3.1 Sound Speed in Bubbly Water	16
2.3.2 Sound Speed in Bubble-free Water	19
2.4 Wood's Theory	20
3 Acoustical Resonator Theory	22
3.1 Total Scattering Cross Section	22
3.2 Extinction Cross Section	23
3.3 Sound Attenuation by Bubbles	24
3.4 Acoustical Resonator Theory	26
4 Hardware Implementation	29
4.1 General System Description	29
4.2 The Sound-speed Sensor	31
4.2.1 Compromising among Acoustic Frequency, Pulse Length, Distance between the Hydrophones and Depth	31
4.2.2 The Sound-speed Sensor	33
4.3 Resonator Sensor	36
5 Basic Data Processing Techniques	39
5.1 General Description of Data Processing for Bubble Distribution Estima- tion	39
5.2 Basic Signal Processing Considerations	41
5.2.1 Sampling	41
5.2.2 Pulse Shaping and Windows	42

7.4 5.2.3	Trend Removal	43
5.3	Time-delay Estimation	47
5.3.1	Demodulation	47
5.3.2	Cross Correlation	47
5.3.3	Complex Cross Correlation	51
5.3.4	The Use of Phase Information	52
5.3.5	Interpolation of Sound-speed Anomaly Estimates Between Sources	54
5.4	Inference of Bubble Size Distribution	58
8.2.2	Sound-speed Anomaly at Different Depths	107
6	Propagation of Short Acoustic Pulses in Bubbly Water	60
6.1	Preliminary	60
6.2	The Transient Process	63
6.3	The Effect of Transient Process on Sound Propagation	66
7	Laboratory Experimental Results	72
7.1	The Acoustic Signals	72
7.1.1	Multi-frequency Pulse	73
7.1.2	Single-frequency Pulse and the Template for Cross-correlation	76
7.1.3	Trend Removal.	77
7.2	Effective Distance and Sound Speeds at Different Temperatures.	79
7.2.1	Effective Distance and Total Delay Discussion	79
7.2.2	Thermometer Calibration.	80
7.2.3	Measurement of Effective Distance and Sound Speeds at Different Temperatures	82
7.3	Cramer-Rao Lower Bound on Time Delay Estimation	85
7.3.1	Cramer-Rao Lower Bound	85
7.3.2	Standard Deviation of Sound Speed Estimate	86
7.3.3	Signal to Noise Ratio of Acoustical Pulses	88

7.4	Laboratory Test of Sound Speed in Bubbly Water	90
7.5	Summary	93
8	Field Experimental Results	95
8.1	About the Field Experiment	95
8.2	Sound-speed Anomaly in Bubbly Water	96
8.2.1	Comparison of Sound-speed Anomaly Estimates Between Sound-speed Sensor and Resonator Sensor.	96
8.2.2	Sound-speed Anomaly at Different Depths.	107
8.3	Under-estimate of Attenuation when Using a Short Acoustic Pulse in Bubbly Water	111
9	Conclusions and Future Work	117
9.1	Summary and Conclusions	117
9.2	Suggestions for Future Work	118
	Bibliography	120

Langmuir circulation: The organization of ocean surface wind driven circulation into counter rotating vortices, approximately aligned with the wind, first identified by Irving Langmuir (1938) [14, 15].

Phase unwrapping: a process to recover the total phase which could be larger than 2π by adding or subtracting 2π to or from the current estimate of the phase.

unwrapped phase.

Sound speed anomaly: The change of the sound speed in bubbly water from that in bubble-free water, caused by a bubble.

Sound speed sensor: Apparatus to measure sound speed by estimating the travel time or time delay for a sound wave to travel from a transmitting transducer to a receiving transducer.

Resonator sensor: Apparatus to measure the change of sound speed and attenuation according to the change of an acoustical standing wave field between two plates, where one plate is used as a transmitter and the other one is used as a reflector.

Glossary of Terms

Langmuir circulation: The organization of ocean surface wind driven circulation into counter rotating vortices, approximately aligned with the wind, first identified by Irving Langmuir (1938) [14, 15].

Phase unwrapping: a process to recover the total phase which could be larger than 2π by adding or subtracting 2π to or from the current estimate of the phase. The addition and subtraction are determined by the estimate of the previous unwrapped phase.

Sound speed anomaly: The change of the sound speed in bubbly water from that in bubble-free water.

Sound speed sensor: Apparatus to measure sound speed by estimating the travel time or time delay for a sound wave to travel from a transmitting transducer to a receiving transducer.

Resonator sensor: Apparatus to measure the change of sound speed and attenuation according to the change of an acoustical standing wave field between two plates, where one plate is used as a transmitter and the other one is used as a reflector.

List of Symbols

R	Radius of a bubble
c	Sound speed
c_0	Sound speed in bubble free water
C_p	Specific heat at constant pressure of the enclosed gases in a bubble
C_v	Specific heat at constant volume of the enclosed gases in a bubble
g	Gravity
f	Frequency of an incident sound wave
f_R	Resonant frequency of a bubble
I_p	Intensity of an incident sound wave
I_s	Intensity of the scattered sound wave
J	Extinguished intensity of a sound wave
α_b	Attenuation per unit distance due to bubbles
γ	Ratio of the specific heats of the enclosed gases in a bubble, C_p/C_v
δ_R	Damping constant of a bubble at resonance
δ_{Rt}	Damping constant of a bubble at resonance due to thermal conductivity
δ_{Rv}	Damping constant of a bubble at resonance due to shear viscosity
δ_{Rr}	Damping constant of a bubble at resonance due to reradiation
ζ	Radial displacement of a bubble during oscillation
λ	Wave length of a sound wave
μ	Shear viscosity of the water
Δv	Change in volume of a bubble
Π_a	Power absorbed by a bubble
Π_e	Power scattered and absorbed by a bubble
Π_s	Total power scattered over all angles
σ_D	Standard deviation of time-delay estimates
σ_C	Standard deviation of sound-speed estimates
σ_a	Absorption cross section
σ_e	Extinction cross section, $\sigma_s + \sigma_a$
σ_s	Scattering cross section
ω	Radian frequency of an incident sound wave
ω_R	Radian frequency of a bubble at resonance
ρ_A	Density of the ambient water
ρ_g	Density of gas
ρ_{gA}	Density of gas at sea level
τ_s	Surface tension

a	Radius of a bubble
c	Sound speed of a bubble, $4\pi a^2$
c_0	Sound speed in bubble free water
C_p	Specific heat at constant pressure of the enclosed gases in a bubble
C_v	Specific heat at constant volume of the enclosed gases in a bubble
g	Gravity <i>surface in the water</i>
f	Frequency of an incident sound wave
f_R	Resonant frequency of a bubble
I_p	Intensity of an incident sound wave
I_s	Intensity of the scattered sound wave
I_e	Extinguished intensity of a sound wave
G_{xy}	Cross spectrum of two sequences, x and y
G_{xyi}	Cross spectrum of the inphase part of two sequences, x and y
G_{xyq}	Cross spectrum of the quadrature part of two sequences, x and y
k	Propagation constant of a sound wave
k_{im}	Image part of the propagation constant of a sound wave
k_{re}	Real part of the propagation constant of a sound wave
K	Compressibility
K_0	Compressibility due to bubble-free water
K_1	Compressibility due to bubbles
K_g	Thermal conductivity of gas
$n(a)$	Bubble size distribution function
m	Effective mass of bubble due to surrounding fluid
P_a	Gauge pressure due to water column
P_A	Pressure of the ambient water
P_p	Root mean square pressure of an incident plan wave
P_s	Root mean square pressure of a scattered sound wave
P_x	Extinguished pressure of a plane wave after traversing distance x
R_M	Mechanical damping constant represents energy losses caused by sound reradiation, shear viscosity, and thermal conductivity
\hat{R}_{xy}	Cross correlation function of two sequences, x and y
\hat{R}_{xyi}	Cross correlation function of the inphase part of the two sequences, x and y
\hat{R}_{xyq}	Cross correlation function of the quadrature part of the two sequences, x and y

s	Stiffness constant
S	Surface area of a bubble, $4\pi a^2$
Sa	Salinity in the water
S_e	Extinction cross section per unit volume
SWH	Significant wave height
T	Temperature in the water
t	Time variable
U	Wind speed
V	Volume of the water
x	Distance variable of wave propagation
Y	Frequency ratio, f_R/f
Z, z	Depth in the water

Table 1.1. Review of bubble population data. 3

Table 1.2. Review of bubble population data. (cont.). 4

Table 1.3. Review of bubble population data. (cont.). 5

Table 7.1. The optimized initial phases of multi-frequency pulses 73

Table 7.2. The weights for the amplitudes of multi-frequency pulses 76

Table 7.4. Linear fit parameters 80

Table 7.3. The preliminary calibrations of the higher standard sensors 80

Table 7.5. Calibration parameters of HP2801A 81

Table 8.1. Frequency and transient factor. 113

List of Tables

Table 1.1.	Review of bubble population data. from Eq. (2.3) to that from Eq. (2.3)	3
Table 1.2.	Review of bubble population data. (cont.)	4
Table 1.3.	Review of bubble population data. (cont.). (Depth=1 m)	5
Table 7.1.	The optimized initial phases of multi-frequency pulses	73
Table 7.2.	The weights for the amplitudes of multi-frequency pulses	76
Table 7.4.	Linear fit parameters	80
Table 7.3.	The preliminary calibrations of the higher standard sensors	80
Table 7.5.	Calibration parameters of HP2801A	81
Table 8.1.	Frequency and transient factor.	113
Figure 2.4	Sound speed at appearance of single size bubbles (when sound speed in bubble-free water is 1487m/s).	18
Figure 2.5	Sound speed in bubble-free ocean water (salinity=35 ppt).	20
Figure 3.1	Extinction cross sections (solid lines) and total scattering cross sections (dashed lines) at four frequencies as a function of bubble radius. Air bubble in water at sea level.	25
Figure 3.2	Resonance spectrum with and without bubbles.	27
Figure 4.1	Diagram of showing prototype of the sound-speed and acoustical resonator system developed at IOS.	30
Figure 4.2	Final structure of the sound-speed sensor and resonator sensor head	31
Figure 4.3	Relationship between frequency, depth and hydrophone separation for	

List of Figures

Figure 2.1	pulses with a duration of 2 cycles.	34
Figure 4.4	Block diagram of the sound-speed sensor.	35
Figure 4.3	Schematic diagram of the acoustical resonator.	37
Figure 5.1	Flow chart of data processing used to obtain bubble distribution.	40
Figure 5.2	Demonstration of Nyquist Sample ratio.	41
Figure 5.3	Rectangular window and side-lobes.	42
Figure 5.4	Frequency response of Hamming window.	43
Figure 5.5	Illustration of linear trend removal.	46
Figure 2.1	Ratio of the resonant frequency from Eq. (2.3) to that from Eq. (2.1)	9
Figure 5.6	Schematic diagram of demodulation.	48
Figure 5.7	Demonstration of cross correlation.	49
Figure 2.2	Resonant frequency versus bubble radius. (Depth=1 m)	11
Figure 5.8	Computation diagram for cross-correlation function.	50
Figure 2.3	Damping constants at 1, 10, 50 and 100kHz for air bubbles in water at sea level. The contributing terms due to viscosity, thermal conductivity, and acoustic radiation are shown for the 10-kHz case. The resonance radii and the damping constants at resonance are indicated by arrows. Subscript R indicates resonance.	13
Figure 5.9	Schematic diagram of complex cross correlation.	52
Figure 5.10	Demonstration of demodulation.	54
Figure 5.11	Conversion of the complex cross correlation function.	57
Figure 2.4	Sound speed at appearance of single size bubbles (when sound speed in bubble-free water is 1487m/s).	18
Figure 5.12	Damping constant at resonance versus bubble radius when the incident phase of the complex cross correlation function.	59
Figure 2.5	Sound speed in bubble-free ocean water (salinity=35 ppt).	20
Figure 3.1	Extinction cross sections (solid lines) and total scattering cross sections (dashed lines) at four frequencies as a function of bubble radius. Air bubble in water at sea level.	25
Figure 6.2	Relationship between frequency, depth and hydrophone separation for waves.	63
Figure 3.2	Resonance spectrum with and without bubbles.	27
Figure 4.1	Diagram of showing prototype of the sound-speed and acoustical resonator system developed at IOS.	30
Figure 6.4	Relationship between frequency, depth and hydrophone separation for waves.	65
Figure 4.2	Final structure of the sound-speed sensor and resonator sensor head	31
Figure 4.3	Relationship between frequency, depth and hydrophone separation for waves.	65

Figure 7.1	pulses with a duration of 2 cycles.	34
Figure 4.4	Block diagram of the sound-speed sensor.	35
Figure 4.5	Schematic diagram of the acoustical resonator.	37
Figure 5.1	Block diagram of data processing used to obtain bubble distribution.	40
Figure 5.2	Demonstration of Nyquist Sample ratio.	41
Figure 5.3	Rectangular window and side-lobes.	42
Figure 5.4	Frequency response of Hamming window.	43
Figure 5.5	Illustration of linear trend removal.	46
Figure 5.6	Schematic diagram of demodulation.	48
Figure 5.7	Demonstration of cross correlation.	49
Figure 5.8	Computation diagram for cross-correlation function.	50
Figure 5.9	Schematic diagram of complex cross correlation.	52
Figure 5.10	Demonstration of delay estimation.	54
Figure 5.11	Demonstration of quadratic fitting of $ R_{xy} $	55
Figure 5.12	Demonstration of cubic spline fitting for inphase and quadrature cross-correlation function, R_{xyi} and R_{xyq} . Eight points are used for the fit.	56
Figure 5.13	Converted phase of the complex cross-correlation function.	57
Figure 6.1	Damping constant at resonance versus bubble radius when the frequency of incident sound wave is equal to bubble resonant frequency.	64
Figure 6.2	Ring damping constant versus the frequency of an incident sound wave.	65
Figure 6.3	Time needed to reach four different ringing amplitudes, Q , at different frequencies.	68
Figure 6.4	Number of cycles of incident sound waves at four different ringing amplitudes, Q	69
Figure 6.5	Demonstration of transient process.	70

Figure 7.1	Multi-frequency pulse with the same initial phases	72
Figure 7.2	Received multi-frequency pulse with optimized phase.	74
Figure 7.3	Energy spectrum of a multi-frequency pulse.	74
Figure 7.4	Carrier signals filtered from multi-frequency pulse.	75
Figure 7.5	Comparison of templates.	77
Figure 7.6	Demonstration of trend in real data.	78
Figure 7.7	Demonstration of higher order trend removal	78
Figure 7.8	Temperature deviation of calibrated HP2801A	81
Figure 7.9	Demonstration of temperature test in a small tank	82
Figure 7.10	Estimated delay versus temperature	83
Figure 7.11	Variation of estimated effective distance versus temperature.	84
Figure 7.12	Comparison of measured sound speeds with the calculated sound speeds at different temperatures.	84
Figure 7.13	Cramer-Rao lower bound on the standard deviation of the time delay estimate (observation time $T=0.4$ ms; signal bandwidth $B=12$ kHz).	86
Figure 7.14	Time-series of received acoustic pulses and their energy spectra. Recorded in the open ocean with a wind speed of about 6 m/s.	88
Figure 7.15	Time-series of a multi-frequency acoustic pulse and its energy spectrum. Recorded at open sea with wind speed about 4 m/s.	89
Figure 7.16	Schematic diagram of bubble distribution test.	90
Figure 7.17	Sound speeds vs. time at different frequencies (laboratory study using electrolytically generated bubbles; Data: Nov22/94).	91
Figure 7.18	Sound speeds at different frequencies (laboratory study using electrolytically generated bubbles. Data: Nov.22/94).	92
Figure 7.19	Comparison of sound speeds in bubbly water with two different frequencies (from Figure 7.18).	94

Figure 8.1	Wind speed during the experiment in January 1995.	95
Figure 8.2	Comparison of sound-speed anomalies from a resonator sensor and a sound-speed frequencies at different frequencies; Depth=1.4 m.	98
Figure 8.3	Comparison of sound-speed anomalies from a resonator sensor and a sound-speed sensor at different sensors; Depth=1.4 m, cont'd.	99
Figure 8.4	Comparison of sound-speed anomalies from a resonator sensor and a sound-speed sensor at different frequencies; Depth=1.4m. cont'd.	100
Figure 8.5	Comparison of sound-speed anomalies from a resonator sensor and sound-speed sensor at different frequencies; Depth=1.4m. cont'd.	101
Figure 8.6	Comparison of sound-speed anomalies from a resonator sensor and a sound-speed sensor at different frequencies; Depth=1.4m. cont'd.	102
Figure 8.7	Comparison of sound-speed anomalies from a resonator sensor and a sound-speed sensor at different frequencies; Depth=1.4m. cont'd.	103
Figure 8.8	A short enlarged segment of the time-series shown in Figure 8.2. For the results from a sound-speed sensor, dotted line: original estimates; solid line: lowpass filtered estimates.	104
Figure 8.9	Sound-speed anomalies from a sound-speed sensor at different frequencies; Depth=1.4m.	105
Figure 8.10	Sound-speed anomaly versus frequency (depth=1.4 m, the events refer to Figure 8.2.)	106
Figure 8.11	Sound-speed anomaly at different depths. Wind speed=17m/s.	108
Figure 8.12	Sound-speed anomaly at different depths. Wind speed=17m/s.	109
Figure 8.13	Short enlarged segments of the time-series shown in Figure 8.11 and Figure 8.12. Dotted line: original estimates; solid line: lowpass filtered estimates. Darsi1: 1.4m; Darsi2: 3.2m; Darsi3: 0.5 m.	110
Figure 8.14	A short enlarged segment of the time-series shown in Figure 8.11 for the sound-speed anomalies at different depths. Dotted line: original	

estimates; solid line: lowpass filtered estimates. Darsi1: 1.4m; Darsi2: 3.2m; Darsi3: 0.5m. 111

Figure 8.15 Sound-speed anomaly versus frequency at different depths (the events refer to Figure 8.11). 112

Figure 8.16 Attenuation at various frequencies obtained by band-pass filtering a 20 min. record of composite pulse data acquired at a depth of 0.5 m. The various band-pass frequencies are indicated on the plots. The wind speed and the SWH were 8 m/s and 0.46 m. respectively. From Lamarre's thesis [20]. 114

Figure 8.17 Transient factor versus transient time at different frequencies. . . 115

Acknowledgments

I wish to express my gratitude to my supervisor, Dr. David Farmer for his persistent encouragement, guidance, support and advice during the course of this thesis work. His undivided motivation and endeavour have been the major driving factors in the success of this project.

I thank my co-supervisor Dr. Peter Driessen for his valuable comments and for aiding me with text books and technical papers during the progress of this research. I would also like to extend my thankfulness to Dr. Lynn Kirlin for the valuable discussions.

I would like to thank Drs. Jens Bornemann, Dr. Gholamali. C. Shoja for their services as my supervisory committee members, and Dr. Ross Chapman for his valuable comments and services as the external examiner in my M.A.Sc. oral examination

I am very grateful to all the friends at the Acoustic Group at the Institute of Ocean Sciences for creating the friendly atmosphere in which I have had the pleasure to work. In particular, I wish to thank Dr. Svein Vagle for his unforgettable help and suggestions which make this thesis as such a success. Besides, I wish to thank Grace Kamitakahara and Willi Weichselbaumer for their computer support. My thanks also go to Ron Teichrob for the design of the electronics and to Alan Adrian for the design and implementation of the instrument platform. I am also grateful to Nick Hall-Patch who did a marvellous job at implementing and looking after the hardware used

Acknowledgments

Finally, a word of gratitude to my parents, Mindeng Zhou and Zhaoxian Mao, my sisters, Yijia Mao and Yinci Mao for their moral support, motivation and encouragement. Also, I would thank my dear wife, Haibo Ma for her giving me love and sup-

I wish to express my gratitude to my supervisor, Dr. David Farmer for his perpetual encouragement, guidance, support and advice during the course of this thesis work.

His undivided motivation and endeavour have been the major driving factors in the success of this project.

This work received support from the U.S. office of Naval Research ocean acoustics program, under the direction of Drs. M. Bardey and J. Simmens.

I thank my co-supervisor Dr. Peter Driessen for his valuable comments and for aiding me with text books and technical papers during the progress of this research. I would also like to extend my thankfulness to Dr. Lynn Kirilin for the valuable discussions.

I would like to thank Drs. Jens Bornemann, Dr. Gholamali. C. Shoja for their services as my supervisory committee members, and Dr. Ross Chapman for his valuable comments and services as the external examiner in my M.A.Sc. oral examination

I am very grateful to all the friends at the Acoustic Group at the Institute of Ocean Sciences for creating the friendly atmosphere in which I have had the pleasure to work. In particular, I wish to thank Dr. Svein Vagle for his unforgettable help and suggestions which make this thesis as such a success. Besides, I wish to thank Grace Kamitakahara and Willi Weichselbaumer for their computer support. My thanks also go to Ron Teichrob for the design of the electronics and to Alan Adrian for the design and implementation of the instrument platform. I am also grateful to Nick Hall-Patch who did a marvellous job at implementing and looking after the hardware used

throughout my experiments.

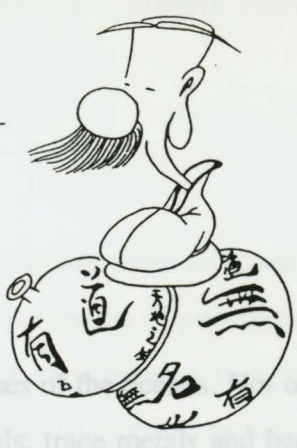
Finally, a word of gratitude to my parents, Mindeng Zhou and Zhaoxian Mao, my sisters, Yijia Mao and Yimei Mao for their moral support, motivation and encouragement. Also, I would thank my dear wife, Haibo Ma for her giving me love and support without which my studies would not have crystallized. I would like to dedicate this thesis to my wife and to my parents.

This work received support from the U.S. office of Naval Research ocean acoustics program, under the direction of Drs. M. Bardey and J. Simmens.



IF YOU SAY THAT YOU UNDERSTAND IT
THEN IT IS WRONG

「道」可道，非常
 「道」。「名」可名，非
 常「名」。「无」，名天
 地之始；「有」，名万
 物之母。故常「无」，
 欲以观其妙；常「有」，
 欲以观其微。此
 两者，同出而异
 名，同谓之玄。
 玄之又玄，众
 妙之门。



IF YOU SAY THAT YOU UNDERSTAND IT
 THEN IT IS WRONG

waves gives us information about wind, including wind speed and wind stress [10]. Also through knowledge of the bubble distribution in the surface layer, we can predict the best performance of a ship's sonar.

Chapter 1

In general, the knowledge of spatial distribution of bubbles in the ocean is important to help us understand many oceanographic phenomena and to solve many practical problems related to the oceans.

Introduction

1.2 Historical Background

1.1 Bubbles in the Ocean

Bubbles play an important role in physical processes of the oceans. Not only are the bubbles scavengers of ocean detritus, organic materials, trace metals and bacteria, they also scatter and absorb sound waves. In fact, the formation, movement and bursting of bubbles at the surface are generating a significant portion of the high frequency ambient sound field in the ocean [10, 11].

Breaking waves generate large amounts of air bubbles in the ocean surface boundary layer. These bubbles formed directly below the surface, are entrained into deeper water by turbulence and Langmuir circulation [15, 16, 34]. The penetration depth depends on the size of wind-waves and may reach several tens of metres in high waves [19]. But usually the depth is of the order of metres [40].

The mixed layer (also called surface layer) is the layer near the ocean surface, where temperature, salinity and other properties are almost uniformly distributed. The mixed layer plays a significant role in the exchange of heat, mass and momentum between the atmosphere and the interior of the ocean. Bubbles are largely involved in those exchange processes.

Bubbles have been used as tracers of fluid motion to study turbulence and Langmuir circulation in the ocean [15, 16, 34]. The number of bubbles made by breaking

waves gives us information about wind, including wind speed and wind stress [10]. Also through knowledge of the bubble distribution in the surface layer, we can predict the best performance of a ship's sonar.

In general, the knowledge of spatial distribution of bubbles in the ocean is important to help us understand many oceanographic phenomena and to solve many practical problems related to the oceans.

1.2 Historical Background

Several studies have been conducted over the past twenty years to investigate the bubble population in the ocean surface layer. Comprehensive results of population and size spectra of bubbles have been obtained using different experimental techniques. Generally, these techniques can be classified into two categories: acoustic techniques and optical techniques [6, 19]. Optical techniques include bubble traps, laser and photographic methods [17, 19, 23, 24]. Tables 1.1, 1.2 and 1.3 are from [20] to summarize results accumulated by various investigators since 1970 and to give a good review of bubble population literature.

Acoustic techniques are based on the investigation of the scattering and attenuation of acoustic signals at various frequencies. Acoustic backscatter and attenuation measurements [24, 28, 35, 36], as well as sound speed dispersion [20, 21] all fall into this category. Bubbles of different sizes have different resonant frequencies [37] so that the radius of a bubble can be determined by its resonant frequency. A bubble's reradiation makes its scattering cross section much larger than the geometrical cross section so that the bubble population can be determined by its backscattering cross section and can be distinguished from small particles [24, 25, 26]. Sound velocity and attenuation in bubbly water have been studied since the 1950s [12, 32, 13]. The effect of air bubbles on sound velocity and attenuation in the water can also be used to infer the bubble population [26, 20, 21].

Authors	Medwin (1970)	Kolovayev (1977)	Medwin (1977)	Walsh and Mulhearn (1987)	Johson and Cooke (1979)
ranges (μm) and technique	18 to 180 acoustic	14 min. bubble trap	15 to 300 acoustic	50 min. photography	17 min. photography
slopes	a^{-4} $a < 80$ a^{-2} $a > 80$	$a^{-3.5}$	a^{-4} $a < 60$ a^{-2} $a > 60$	a^{-4} $a > 100$	a^{-5}
peak (μm)	no peak	70 to 80	no peak	68	40 to 50
meas. depth & water depth (m)	1.5 to 14 coastal waters	1.5 to 8 open sea	3 to 36 1000	0.5 to 2 120	0.7 to 4 20 to 30
depth dependence of total number of bubbles	$N \sim e^{-e/L}$ $a < 60\mu m$ $L=7m$ $N \sim z^{-1/2}$ $a > 60\mu m$	$N \sim e^{-z}$ $z < 3m$ * $N \sim z^{-2.6}$ $z > 3m$ *	none	observations showed dependence with depth	$N \sim e^{-z}$ $z < 3m$ * $N \sim z^{-2.6}$ $z > 3m$ *
num. of bubbles at $a=100 \mu m$ per m^3	150 $d=1.5m$ $U=1-4 m/s$	350 * $d=1.5m$ $U=11-13 m/s$	250 $d=1.5m$ $U=11-13m/s$	300 $d=1.0m$ $U=9 m/s$	176 $d=1.8m$ $U=11.13 m/s$
wind speed range (m/s)	1 to 4	6 to 13	up to 6	2 to 14	8 to 13
wind speed dependence	N/A	$N \sim U^{-4.5}$ *	N/A	$N \sim U^{3.3}$ $U < 6 m/s$	$U^{4.5}$ *

Table 1.1. Review of bubble population data.^a

a. The (*) refers to Wu's review paper [40]. Peak and slope refer to the shape of the bubble population. The total number of bubbles per m^3 is N and $n(a)$ is the number of bubbles per m^3 in a band da ($1 \mu m$). N/A refers to "not applicable or available" and "none" means no dependence in the data was found.

Table 1.2. Review of bubble population data. (cont.)

1.2.1 Acoustical Attenuation

To measure bubble populations at various sizes, Medwin [24] used a bubble spectrometer where the technique used is based on the investigation of attenuation and scattering of acoustic signals at various frequencies (20-200 kHz). With a wind speed range of 1 ~ 4 m/s, he found that the slope of the logarithm of bubble density versus the logarithm of bubble radius a (μm) was -4 for $a < 80 \mu m$ and -2 for $a > 80 \mu m$ at depths from 1.5 m to 14 m. The total number of bubbles per unit volume, N , was proportional to $e^{-z/7}$ for $a < 60 \mu m$ and $z^{1/2}$ for $a > 60 \mu m$, where z is depth below the sea surface.

Authors	O'hen et al. (1988)	Su (1988)	Baldy (1977)	Medwin and Breitz (1989)	Vagle (1989)
ranges (μm) and technique	18 to 250 holography	20 to 400 optical	30 to 1500 laser laboratory	30 to 240 acoustic	16 to 116 acoustic
slopes	a^{-4} $10 < a < 50$	a^3 $a < 30$ a^{-5} to a^{-6} for $a > 200$	a^{-4} $a < 50$ $a^{-2.6}$ $a > 50$	a^{-4} $a < 60$ $a^{-2.6}$ $a > 60$	a^{-4} to a^{-6} for $a < \text{peak}$
peak (μm)	no peak	40 to 50	no peak	no peak	16 to 37
meas. depth & water depth (m)	3 to 33 200	2 to 15 30	0.05 to 0.25 1	0.25 m 500 m	140 or greater continuous 0.1 to 10m 140 m+
depth dependence of total number of bubbles	N/A	none	$n(a) \sim a^{-3.3}$ at 0.05m	N/A	N/A
num. of bubbles at $a=100 \mu\text{m}$ per m^3	N/A	1000 d=2m U=9.5-10.5 m/s	1000 d=0.25m U=14m/s	1000 d=0.25m U=12 to 15 m/s	200 d=1 m U=11 m/s
wind speed range (m/s)	1 to 4	2 to 18	11 to 14	0.25	0 to 16
wind speed dependence	N/A	$N \sim U^{4.0}$ to $U^{4.6}$	$n(a) \sim a^{-4.8}$ $n(a) \sim a^{-3.3}$	11m/s 14m/s	N/A

Table 1.2. Review of bubble population data. (cont.)

Medwin [28] also used an acoustic technique to measure the attenuation of a broad band acoustic signal travelling through bubbly ocean water. The frequency range was 5 – 160 kHz, which implies radii of bubbles ranging from 15 – 300 μm . He found the slope of the bubble size distribution to be -4 for $a < 60 \mu\text{m}$ and -2 for $a > 60 \mu\text{m}$ at approximately 25 μm and, with wind speeds of 11 m/s, the results indicate a slope in the depths between 3 and 36 m. The acoustic path was 1 – 5 m and the wind speed was at most 6 m/s. The experiment was conducted in Monterey Bay, California.

Breitz and Medwin [4] reported some other experimental results in quiescent sea by using a resonator technique similar to the one described in Chapter 3. Those results are

1.2.3 Bubble Trapping

Authors	Hwang et al. (1990)	Vagle and Farmer (1992)	Su et al. (1993)	Kalvoda (1993)
ranges (μm) and technique	800 to 3000 laser laboratory	8 to 130 acoustic	34 to 1200 acoustic	1 to 5mm video labora- tory
slopes	$n(a) \sim a^{-\alpha}$ $\alpha = 2.8z/Hs + 0.7$ $0.5 < z/Hs < 1.2$	variable a^{-4} to a^{-7} for $a < 25$	a^{-4} $a < 80$ a^{-3} $a > 80$ up to 1200	$a^{-3.8}$
peak (μm)	no peak	25	no peak	N/A
meas. depth & water depth (m)	6,7,9,10 15cm	continuous 0.1 to 10m	6 depths starting 0.24m	in plume 0.75m depth
depth depen- dence of total number of bubbles	0.75m depth $n(a) \sim a^{-\alpha}$ $\alpha = 2.8z/Hs + 0.7$ $0.5 < z/Hs < 1.2$	140m N/A	90m depth N/A	N/A
num. of bub- bles at $a=100$ μm per m^3	N/A	1000 d=0.5m U=11 m/s	2000 d=0.24m U=10m/s	N/A
wind speed range (m/s)	lab 10 to 15	data for 11 m/s	10 to 15 m/s	lab 16 m/s
wind speed dependence	$N \sim \exp(-z/Hs)$	N/A	N/A	N/A

Table 1.3. Review of bubble population data. (cont.)

The results from the photographic method used by Johnson and Cooke [17] show the quite consistent with the results from [28].

1.2.2 Acoustical Backscatter

A multi-frequency acoustical backscatter scheme was used by Vagle [35] and Vagle & Farmer [36], in which they measured the signal intensity backscattered from bubble clouds. They forced the peak of the bubble size distribution to be at a bubble radius of approximately $25 \mu m$ and, with wind speeds of $11 m/s$, the results indicate a slope in the size distribution ranging from -4 to -7 for $a > 25 \mu m$. The depths of their measurements ranged from 0.1 to $10 m$.

Some of the results from previous investigations are quite consistent while others

1.2.3 Bubble Trapping

Among reported experiments using bubble traps, the most comprehensive one has been done by Kolovayev [19]. He used a pipe as a bubble trap, which was 6 cm in diameter and 20 cm long. The open ends of the pipe were sealed following the sample collection at a designated depth, and the pipe was then tilted to the vertical position. Trapped bubbles that had risen and accumulated at the transparent upper end of the trap were photographed. By counting the number of bubbles trapped in a pipe, he found a peak in the number of bubbles at radii around 70–80 μm and a size distribution slope of -3.5 at wind speeds of 6–13 m/s in the subtropical part of the Atlantic Ocean. The measurements were done from the sea surface to a depth of 25 m. The depth dependence of the total number of bubbles, N , was found to be Az^{-2} , where $A = 9 \times 10^4$.

1.2.4 Photographic Techniques

Photographic techniques also involve counting bubbles from photographs. But unlike the bubble trapping methods, photographic methods can be used in open water. The observation volume of water is determined by the camera and the illuminating instrumentation. The results from the photographic method used by Johnson and Cooke [17] show the slope of the bubble size distribution to be about -5 at wind speed ranging from 8 to 13 m/s. They found the depth dependence of the total number of bubbles, N , to be as $N \sim e^{-z}$ for $z < 3$ m and $z^{-2.6}$ for $z > 3$ m. Wu indicated in [40] that rather consistent variations of bubble populations with depth are shown by the two sets of data (Johnson and Cooke's results and Kolovayev's [19]). He further pointed out that this consistency indicates that the discrepancies in absolute bubble populations obtained in Kolovayev's and in Johnson and Cooke's investigations are likely due to differences in either rates of production or systematic error in measurements. Entrainment processes during both investigations are also likely to take place.

Some of the results from previous investigations are quite consistent while others

are not. However, these experiments were conducted at different places and at different times and with different oceanographic and meteorological conditions. This may be the reason for the inconsistency among the results. However, the inconsistency might also be due to some factors which were omitted in some methods while considered by other methods. These factors will be discussed further in the next section.

1.3 Acoustical versus Optical Techniques

Optical techniques such as photography and bubble trapping are *in situ* measurements that involve small volume samples of water (approximately 10 cm^3) at a time. Because the optical scattering cross section (the ratio of the scattered power to the incident intensity) for either a particle or a bubble is, at most, approximately equal to the geometrical cross section, there is some difficulty distinguishing a bubble from a particle. Therefore, light scattering techniques can be very unreliable in the ocean where there are a large number of particles. For photographic techniques, a large number of photographs must be taken to obtain a satisfactory average bubble density for small numbers of larger bubbles. Bubbles with radii less than about 50 microns may have a shield of detritus on their surfaces so that the expected sphericity of the bubbles can not be identified [23].

Compared with optical techniques, acoustical techniques are more efficient and more reliable for measurements of bubble distributions. Bubbles will be forced to pulsate and radiate sound during bubble formation, coalescence, or division; and they will also vibrate when they pass an obstacle or when they encounter sound waves with frequencies close to the resonant frequencies of the bubbles [33].

1.4 The Thesis Work

Even though acoustical techniques have given us some efficient tools to estimate the bubble distribution in the ocean, as discussed above, there are some significant discrepancies in the results. Since all the experiments using different acoustical approaches were conducted in different locations and at different times, the physical conditions could have

been quite different, and thus resulted in the reported differences. Therefore, to better understand these acoustical techniques, it is desirable to do some experiments simultaneously using more than one acoustical method.

This thesis undertakes part of the work to develop a new system consisting of an acoustical resonator sensor and a sound-speed sensor. With this combined instrument we can use both sensors to estimate the bubble distribution simultaneously and then compare the results. This thesis concentrates on the sound-speed sensor part of the system, but includes some comparison of the results from both sensors in Chapter 8. The data processing techniques used in the thesis to estimate sound speeds are proved to be effective. Since a short acoustical pulse was used in our system, the transient process of the bubble resonance is analyzed. Some new equations for the effect of this transient process on sound wave propagation are further derived in Chapter 6, which improves bubble size distribution estimation. The novel aspects of the present work include: (i) the examination of, and implementation of some new signal processing approaches to the measurement of sound speed; (ii) derivation of equations and solutions describing the transient response effects on sound speed and attenuation; (iii) re-interpretation of previously published data analysis in the light of the transient response theory.

In Chapter 2, the theory of acoustic propagation in bubbly water is presented, and the equations to infer the bubble size distribution from sound speed measurements are given. The principles of the resonator sensor are presented in Chapter 3. Then in Chapter 4 the present system is described. Chapter 5 discusses some basic data processing considerations and techniques. The effect of bubbles on short pulse propagation is discussed in Chapter 6. In Chapter 7, the laboratory tests and the results of the calibration of the instrument are presented. Some field experiment results are given in Chapter 8, where short pulse theory presented in Chapter 6 is verified and the results obtained from the sound-speed sensor and the resonator sensor are compared. Chapter 9 concludes the work and presents some thoughts on future work.

Figure 2.1 Ratio of the resonant frequency from Eq. (2.3) to that from Eq. (2.1) versus bubble radius.

2.1 Bubble Resonance

Chapter 2

Underwater Sound Propagation

When a bubble is resonated by a sound wave at or near its natural frequency, it absorbs sound very effectively. At resonance the scattering cross section of a typical bubble is of the order 10^3 times its geometrical cross section. Besides being a source of scattering and absorption, bubbles also compress the air of the water and cause the phase speed of sound to be a function of frequency. During stormy periods the water within 10 meters of the sea surface contains enough bubbles to alter the speed of sound by several hundred meters per second [12] (depending on the frequency), compared to the sound speed in bubble-free water (e.g. 1480 m/s).

Breaking wave processes result in large numbers of bubbles being generated in the surface layer of the ocean. When sound waves penetrate this bubble layer the bubbles will resonate because of their stiffness and inertia. The stiffness of a bubble is due to the gas in it, since the bubble is an elastic system in which stress is proportional to strain. The resonance frequency of a bubble depends both on its radius and its depth. Resonating bubbles can usually be very strong scatterers and absorbers of sound waves. Therefore, bubbles in water have very strong effects on sound waves. This chapter will discuss how the sound velocity and attenuation are affected by bubbles.

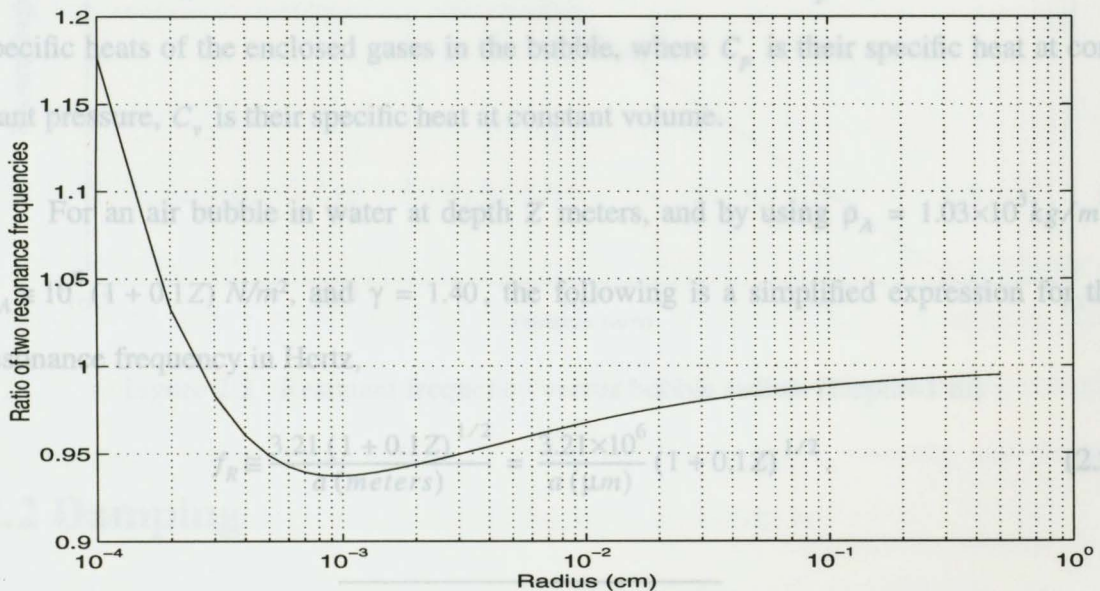


Figure 2.1 Ratio of the resonant frequency from Eq. (2.3) to that from Eq. (2.1) versus bubble radius.

2.1 Bubble Resonance

When a bubble is insonified by a sound wave at or near its natural frequency, it absorbs and scatters the sound very effectively. At resonance the scattering cross section of a typical bubble is of the order 10^3 times its geometrical cross section. Besides being a source of scatter and absorption, bubbles change the compressibility of the water and cause the phase speed of sound to be a function of frequency. During stormy periods the water within 10 meters of the sea surface contains enough bubbles to alter the speed of sound by several hundred meters per second [12] (depending on the frequency), compared to the sound speed in bubble-free water (e.g. 1480 m/s).

With the assumptions that the surface tension can be neglected and that a bubble pulsates adiabatically,¹ the natural frequency f_R can be expressed as follows [39],

$$f_R = \frac{1}{2\pi a} \left[\frac{3\gamma P_A}{\rho_A} \right]^{1/2}. \quad (2.1)$$

The subscript R refers to resonance, a is the mean radius of the bubble, P_A is the static pressure, and ρ_A is the density of the surrounding water. $\gamma = C_p/C_v$ is the ratio of the specific heats of the enclosed gases in the bubble, where C_p is their specific heat at constant pressure, C_v is their specific heat at constant volume.

For an air bubble in water at depth Z meters, and by using $\rho_A = 1.03 \times 10^3 \text{ kg/m}^3$, $P_A \cong 10^5 (1 + 0.1Z) \text{ N/m}^2$, and $\gamma = 1.40$, the following is a simplified expression for the resonance frequency in Hertz,

$$f_R \cong \frac{3.21 (1 + 0.1Z)^{1/2}}{a \text{ (meters)}} = \frac{3.21 \times 10^6}{a \text{ (\mu m)}} (1 + 0.1Z)^{1/2}. \quad (2.2)$$

2.2 Damping

1. Heat exchange between bubble and surrounding water is negligible during a single period of the excitation.

However, when a bubble is small, surface tension cannot be neglected, and the assumption that the gas vibrates adiabatically is also no longer valid. Taking these effects into consideration, (2.1) now becomes

$$f_R = \frac{1}{2\pi a} \left(\frac{3\gamma P_A b \beta}{\rho_A} \right)^{1/2}, \quad (2.3)$$

where b and β are functions for the adiabatic assumption and surface tension, whose formulae will be given in the next section. These two corrections are to some extent mutually counteracting, so the simpler Eq. (2.1) is in error by less than 8% for air bubbles with radii greater than $2\mu\text{m}$ at sea level [8], which can be seen from Figure 2.1 where the ratio of f_R from Eq. (2.3) to that from Eq. (2.2) is plotted versus bubble radius. The relationship between the resonant frequency and the bubble radius using Eq. (2.3) is plotted in Figure 2.2.

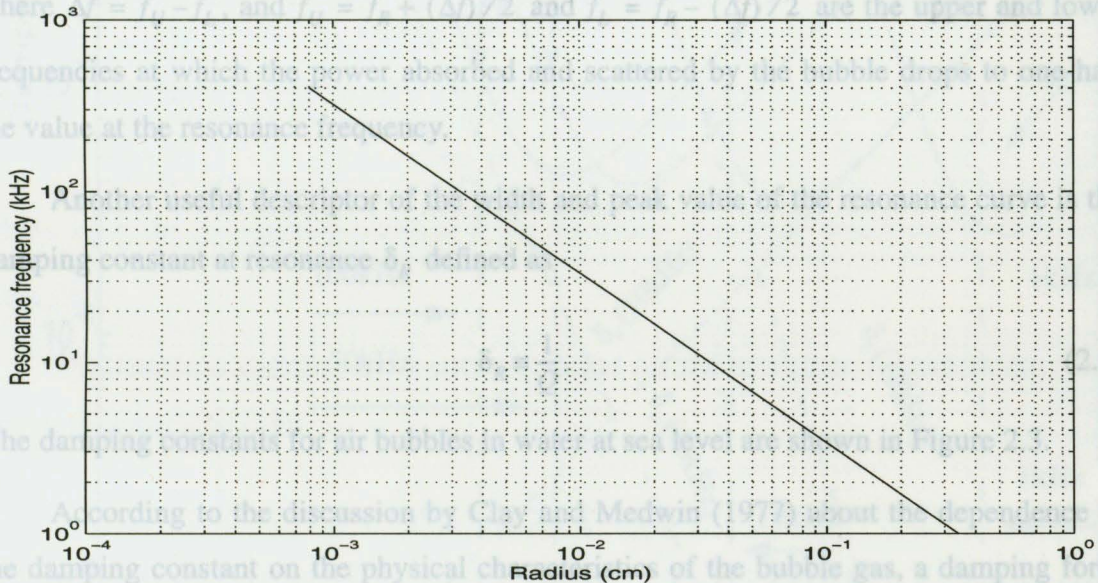


Figure 2.2 Resonant frequency versus bubble radius. (Depth=1 m)

2.2 Damping

A sound wave propagating through bubbly water is attenuated and scattered. The physi-

cal causes of the attenuation are thermal conductivity absorption and shear viscosity together with reradiation (scatter) of sound out of the beam. Theoretically, the absorption of energy caused by thermal conductivity and shear viscosity takes place at the bubble wall. Considering a single bubble, its motion can be described by adding a damping force to the stiffness and inertial forces. Without damping there would be no limit to the amplitude of the bubble pulsation at resonance. With damping, however, the amplitude reaches a maximum at the resonance frequency and has reduced motion at frequencies close to the resonance frequency.

The peakness, or sharpness of the change of amplitude with frequency near resonance, is defined in terms of the Q of the system

$$Q \equiv \frac{f_R}{\Delta f}, \quad (2.4)$$

where $\Delta f = f_U - f_L$, and $f_U = f_R + (\Delta f)/2$ and $f_L = f_R - (\Delta f)/2$ are the upper and lower frequencies at which the power absorbed and scattered by the bubble drops to one-half the value at the resonance frequency.

Another useful descriptor of the width and peak value of the resonance curve is the damping constant at resonance δ_R defined as

$$\delta_R \equiv \frac{1}{Q}. \quad (2.5)$$

The damping constants for air bubbles in water at sea level are shown in Figure 2.3.

According to the discussion by Clay and Medwin (1977) about the dependence of the damping constant on the physical characteristics of the bubble gas, a damping force $R_M \dot{\zeta}$ is assumed, which is proportional to the velocity. The mechanical damping constant R_M represents energy losses caused by sound reradiation, shear viscosity, and thermal conductivity. The equation describing the motion of the bubble is

$$m\ddot{\zeta} + R_M \dot{\zeta} + s\zeta = 4\pi a^2 P_p e^{i\omega t}, \quad (2.6)$$

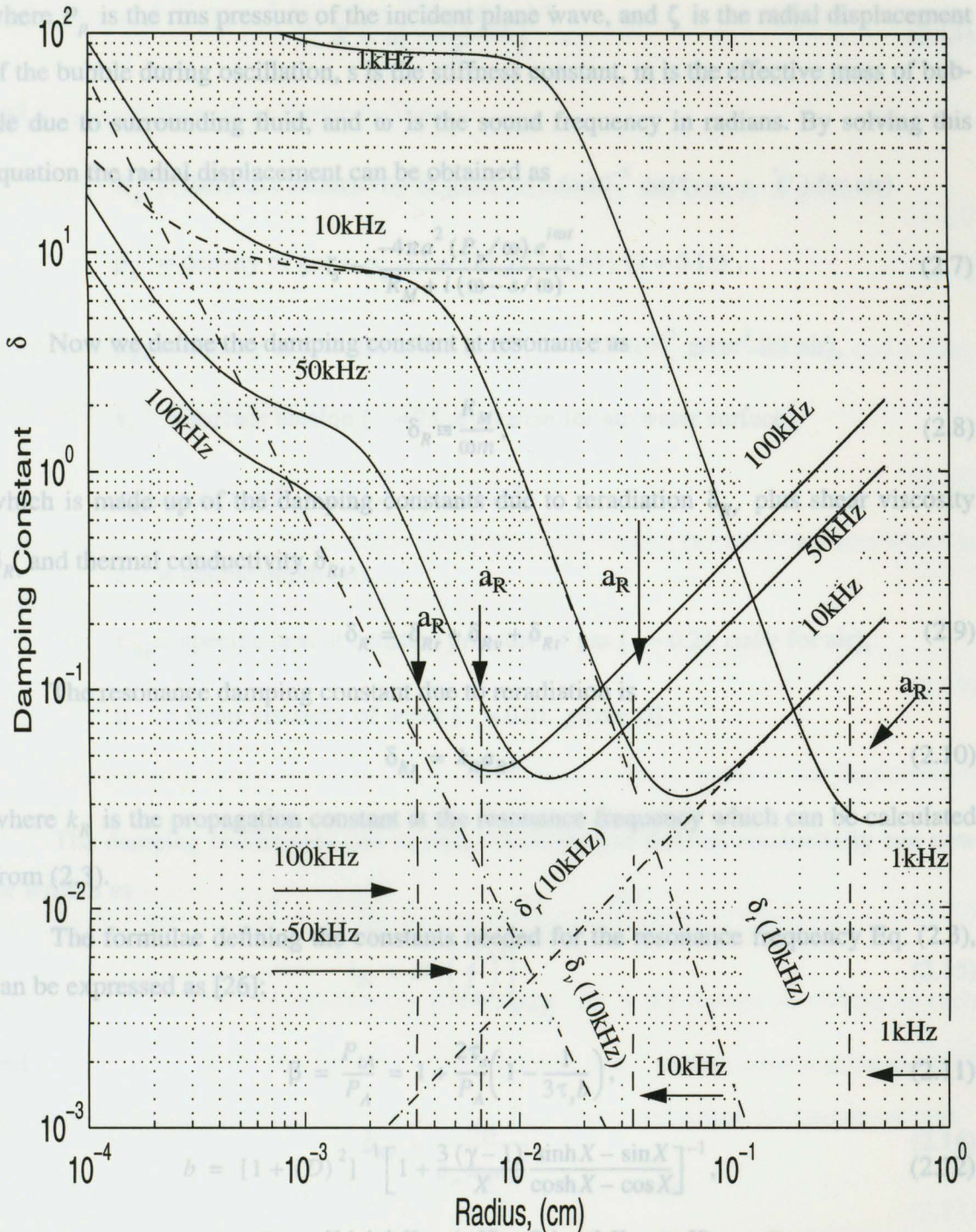


Figure 2.3 Damping constants at 1, 10, 50 and 100kHz for air bubbles in water at sea level. The contributing terms due to viscosity, thermal conductivity, and acoustic radiation δ_v , δ_t and δ_r are shown for the 10-kHz case. The resonance radii and the damping constants at resonance are indicated by arrows. Subscript R indicates resonance.

where P_p is the rms pressure of the incident plane wave, and ζ is the radial displacement of the bubble during oscillation, s is the stiffness constant, m is the effective mass of bubble due to surrounding fluid, and ω is the sound frequency in radians. By solving this equation the radial displacement can be obtained as

$$\zeta = \frac{-4\pi a^2 (P_p/\omega) e^{i\omega t}}{R_M + i(\omega - s/\omega)}. \quad (2.7)$$

Now we define the damping constant at resonance as

$$\delta_R \equiv \frac{R_M}{\omega m}, \quad (2.8)$$

which is made up of the damping constants due to reradiation δ_{Rr} plus shear viscosity δ_{Rv} and thermal conductivity δ_{Rt} ,

$$\delta_R = \delta_{Rr} + \delta_{Rv} + \delta_{Rt}. \quad (2.9)$$

The resonance damping constant due to reradiation is

$$\delta_{Rr} = k_R a_R, \quad (2.10)$$

where k_R is the propagation constant at the resonance frequency which can be calculated from (2.3).

The formulae defining the constants needed for the resonance frequency Eq. (2.3), can be expressed as [26]:

$$\beta = \frac{P_{iA}}{P_A} = 1 + \frac{2\tau_s}{P_A} \left(1 - \frac{1}{3\tau_s b} \right), \quad (2.11)$$

$$b = [1 + (D)^2]^{-1} \left[1 + \frac{3(\gamma-1)}{X} \frac{\sinh X - \sin X}{\cosh X - \cos X} \right]^{-1}, \quad (2.12)$$

$$D = 3(\gamma-1) \left[\frac{X(\sinh X + \sin X) - 2(\cosh X - \cos X)}{X^2(\cosh X - \cos X) + 3(\gamma-1)X(\sinh X - \sin X)} \right], \quad (2.13)$$

where

$$X = a \left(\frac{2\omega\rho_g C_{pg}}{K_g} \right)^{1/2}, \quad (2.14)$$

and **1 Sound Speed in Bubbly Water**

The dependent K_g = thermal conductivity of gas ($\approx 5.6 \times 10^{-5}$ cal/(cm · s · °C) for air)

$$\rho_g = \text{density of gas} = \rho_{gA} [1 + (2\tau_s) / (P_A a)] (1 + 0.1z), \quad (2.17)$$

Here the complex ρ_{gA} = density of free gas at sea level ($\approx 1.29 \times 10^{-3}$ g/cm³ for air), and a complex part due to the bubbles themselves

$$\tau_s = \text{surface tension (} \approx 75 \text{ dynes/cm for air-water surface),} \quad (2.18)$$

$$P_A = 1.013 \times 10^6 (1 + 0.1z) \text{ dynes/cm}^2,$$

where K_0 is expressed in terms of the speed of sound through bubble-free water which is called c_0 given by (2.31) and the ambient density ρ_A

$$C_{pg} = \text{specific heat at constant pressure of gas (} \approx 0.24 \text{ cal/g for air),} \quad (2.19)$$

$$\mu = \text{shear viscosity of water [} \approx 0.01 \text{ g/(cm s)].}$$

The complex compressibility due to the bubbles is found by using the displacement from (2.7)

The damping coefficients due to shear viscosity and thermal conductivity can now be written as

$$K_1 = \frac{\Delta V/V}{\Delta P} = \frac{N\Delta v}{\Delta P} = \frac{NS\zeta}{P_f f \omega} = \frac{NS^2}{m\omega^2 \left[\left(1 + \omega_R^2/\omega^2 \right) + (iR_M)/(\omega m) \right]} \quad (2.20)$$

$$\delta_{Rt} = D \cdot \left(\frac{f}{f_R} \right)^2 \Big|_{f=f_1} \quad (2.15)$$

where N is the number of bubbles per unit volume, Δv is the change in volume of each bubble, $S = 4\pi a^2$ is the surface area of each bubble, and ζ is the radial displacement of the bubble surface. For simplicity, we use $\delta_{Rv} = R_M/(\omega m)$ and define the frequency ratio

$$\delta_{Rv} = \frac{4\mu}{\rho_A \omega_R a_R^2}. \quad (2.16)$$

$$Y = \frac{f_R}{f} = \frac{\omega_R}{\omega}. \quad (2.21)$$

Then

2.3 Sound Speed in the Water

2.3.1 Sound Speed in Bubbly Water

The dependence of the sound speed on the compressibility and density is given by

$$c^2 = \frac{1}{\rho_A K} \quad (2.17)$$

where

Here the compressibility K is made up of a part due to bubble-free water K_0 and a complex part due to the bubbles themselves K_1 ,

$$K = K_0 + K_1, \quad (2.18)$$

where K_0 is expressed in terms of the speed of sound through bubble-free water which is called c_0 given by (2.31) and the ambient density ρ_A

$$K_0 = \frac{1}{\rho_A c_0^2}. \quad (2.19)$$

The complex compressibility due to the bubbles is found by using the displacement from (2.7)

$$K_1 = \frac{\Delta V/V}{\Delta P} = \frac{N \Delta v}{\Delta P} = \frac{NS\zeta}{P_p e^{i\omega t}} = \frac{NS^2}{m\omega^2 \left[\left(-1 + \omega_R^2/\omega^2 \right) + (iR_M)/(\omega m) \right]}, \quad (2.20)$$

where N is the number of bubbles per unit volume, Δv is the change in volume of each bubble, $S = 4\pi a^2$ is the surface area of each bubble, and ζ is the radial displacement of the bubble surface. For simplicity, we use $\delta = R_M/(\omega m)$ and define the frequency ratio

$$Y \equiv \frac{f_R}{f} = \frac{\omega_R}{\omega}. \quad (2.21)$$

Then

$$p_p = P_p \exp [i(\omega t - kx)] \\ = P_p \exp (-k_{im}x) \exp [i(\omega t - k_{re}x)] \quad (2.22)$$

where $k_{im} = k_0 \frac{B}{2}$, $k_{re} = k_0 \left(1 + \frac{A}{2} \right)$.

In this form it is clear that the imaginary part of the complex propagation constant represents the attenuation of the wave in the bubbly region. The real part, k_{re} , is

$$K_1 = \frac{N4\pi a [Y^2 - 1 - i\delta]}{\rho_A \omega^2 [(Y^2 - 1)^2 + \delta^2]}, \quad (2.22)$$

and the speed of sound in a bubbly medium can be written in the form

$$c = \left(\frac{1}{\rho_A \bar{K}} \right)^{1/2} = \frac{c_0}{(1 + A - iB)^{1/2}}, \quad (2.23)$$

where

$$Re\{c\} = \frac{\omega}{k_{re}} = c_0 \left[1 - \frac{2\pi a N c_0^2 (Y^2 - 1)}{\omega^2 [(Y^2 - 1)^2 + \delta^2]} \right], \quad (2.29)$$

and is a function of frequency. The imaginary part of c is dispersive. Sound speed at the appearance of single size bubbles is shown in Figure 2.6, where the bubble radius

$$A = \frac{Y^2 - 1}{(Y^2 - 1)^2 + \delta^2} \frac{4\pi a N c_0^2}{\omega^2}, \quad (2.24)$$

and

$$B = \frac{\delta}{(Y^2 - 1)^2 + \delta^2} \frac{4\pi a N c_0^2}{\omega^2}. \quad (2.25)$$

The interpretation of the complex speed is clearer if we consider the complex propagation constant

$$k = \frac{\omega}{c} = \frac{\omega (1 + A - iB)^{1/2}}{c_0}. \quad (2.26)$$

Since A and B are extremely small in the ambient ocean, the expression, whose square root is extracted, is of the form $(1 + \text{small quantity})$. Therefore, the first terms of the Taylor's expansion for k obey

$a = 0.01 \text{ cm}$ and the number of bubbles $N = 10^9$. From the figure, we can see that the sound speeds increase at the sound frequencies higher than resonant frequency and

$$k \approx k_0 \left(1 + \frac{A}{2} - \frac{iB}{2} \right), \quad (2.27)$$

where $k_0 = \omega/c_0$. frequencies lower than the bubble resonant frequency.

The equation for a plane wave propagating through a bubbly medium is

replacing N by the distribution $n(a) da$, which represents the number of bubbles present with radii between a and $a + da$.

$$p_p = P_p \exp [i(\omega t - kx)] \quad (2.28)$$

$$= P_p \exp (-k_{im} x) \exp [i(\omega t - k_{re} x)]$$

where $k_{im} = k_0 \frac{B}{2}$, $k_{re} = k_0 \left(1 + \frac{A}{2} \right)$. The speed of sound in the bubbly region can be written in terms of the integral over all radii:

In this form it is clear that the imaginary part of the complex propagation constant represents the attenuation of the wave through the bubbly region. The real part, k_{re} , is the wave number for the propagation of constant phase surfaces. The ratio ω/k_{re} is the phase velocity, which we call $Re\{c\}$,

$$Re\{c\} = \frac{\omega}{k_{re}} = c_0 \left[1 - \frac{2\pi a N c_0^2}{\omega^2} \frac{Y^2 - 1}{(Y^2 - 1)^2 + \delta^2} \right], \quad (2.29)$$

and is a function of frequency. The medium is said to be dispersive. Sound speed at the appearance of single size bubbles is plotted in Figure 2.6, where the bubble radius

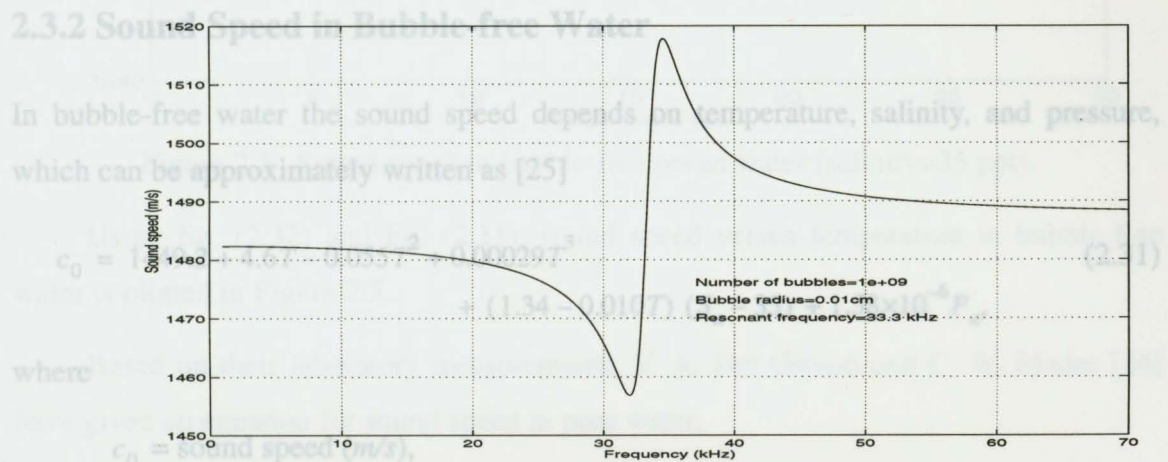


Figure 2.4 Sound speed at appearance of single size bubbles (when sound speed in bubble-free water is 1487m/s).

$a = 0.01\text{cm}$ and the number of bubbles $N = 10^9$. From the figure, we can see that the sound speeds increase at the sound frequencies higher than resonant frequency and decrease at the frequencies lower than the bubble resonant frequency.

The generalization to a medium with bubbles of random radii is accomplished by replacing N by the distribution $n(a) da$, which represents the number of bubbles present with radii between a and $a + da$ at depth z . Because all contributions to the compressibility are very small quantities, they add linearly, and the speed of sound in the bubbly region can be written in terms of the integral over all radii:

$$Re\{c\} = c_0 \left[1 - 2\pi \int_a \frac{aY^2(Y^2-1)n(a)da}{k_R^2(Y^2-1)^2 + \delta_R^2} \right], \quad (2.30)$$

where δ_R is the damping constant at resonance. At very high acoustic frequencies, $f \gg f_R$, $Y^2 \rightarrow 0$, and $Re\{c\} \rightarrow c_0$, implying that for acoustic frequencies in the *MHz* range the presence of micro-bubbles in the water does not affect the sound speed. This result is utilized in acoustic velocimeters that measure the sound speed in water. At the other extreme, $f \ll f_R$, (2.30) is independent of frequency and the sound-speed is only proportional to the amount of gas present in the water, i.e. the medium is no longer dispersive.

2.3.2 Sound Speed in Bubble-free Water

In bubble-free water the sound speed depends on temperature, salinity, and pressure, which can be approximately written as [25]

$$c_0 = 1449.2 + 4.6T - 0.055T^2 + 0.00029T^3 + (1.34 - 0.010T)(S_a - 35) + 1.58 \times 10^{-6}P_a, \quad (2.31)$$

where

c_0 = sound speed (m/s),

$$T = \text{temperature } (^{\circ}\text{C}), \quad (2.33)$$

S_a = salinity (ppt),

P_a = gauge pressure due to water column (N/m^2).

Ignoring compressibility $P_a = \rho_A g z$ and using $\rho_A = (1 + S \times 10^{-3}) \times 10^3 \text{ kg}/\text{m}^3$, $g = 9.8 \text{ m}/\text{s}^2$, $S_a = 35 \text{ ppt}$, and z =depth (m), the last term is now $0.016z$. Therefore, the dependence of sound speed on depth in isothermal water can be typically written as

$$b = \frac{dc}{dz} \approx 0.016 \text{ s}^{-1}. \quad (2.32)$$

and compressibility of the mixture.

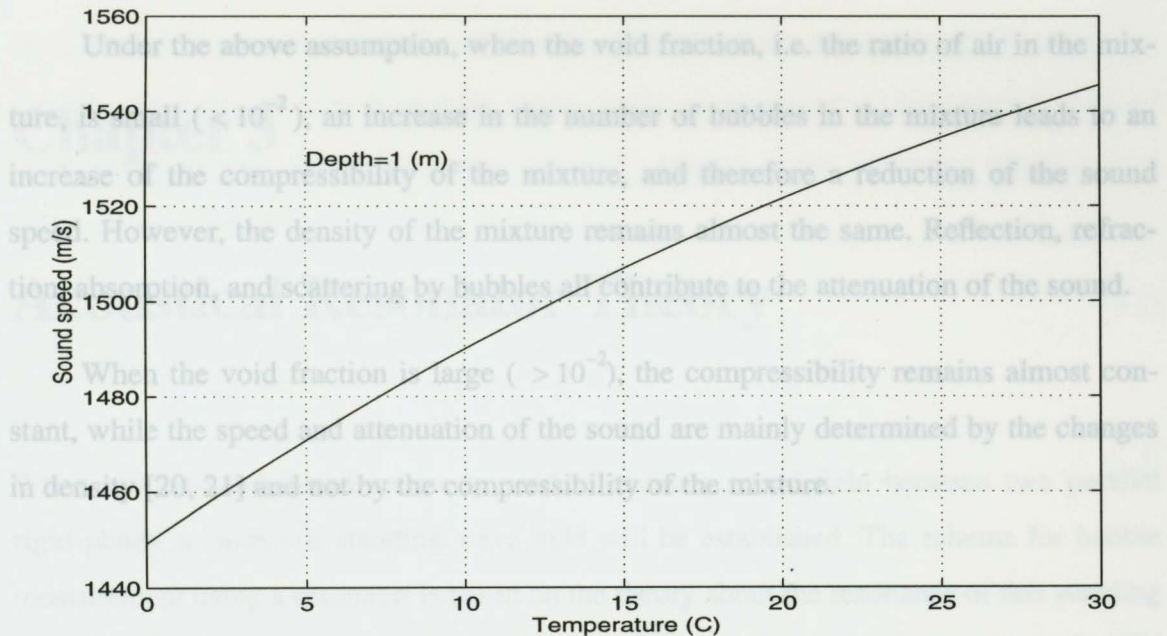


Figure 2.5 Sound speed in bubble-free ocean water (salinity=35 ppt).

Using Eq. (2.32) and Eq. (2.31), sound speed versus temperature in bubble-free water is plotted in Figure 2.5.

Based on their laboratory measurements, V. A. Del Grosso and C. W. Mader [14] have given an equation for sound speed in pure water,

$$c_0 = 0.14023875 \times 10^4 + 0.50371113 \times 10^1 T - 0.58085217 \times 10^{-1} T^2 + 0.33419883 \times 10^{-3} T^3 - 0.14780042 \times 10^{-5} T^4 + 0.31464309 \times 10^{-8} T^5 \quad (2.33)$$

This equation is used here to calibrate the instrument in the laboratory using tap water.

2.4 Wood's Theory

According to Wood's theory [39], when the incident sound frequency is well below the resonant frequency of the largest bubbles in the near surface layer of the ocean, the bubble mixture can be considered as homogeneous with bulk density and compressibility. In other words, the bubbles respond collectively. Therefore, the sound speed of the acoustical signal will not be affected by an individual bubble but determined by the bulk density

and compressibility of the mixture.

Under the above assumption, when the void fraction, i.e. the ratio of air in the mixture, is small ($< 10^{-2}$), an increase in the number of bubbles in the mixture leads to an increase of the compressibility of the mixture, and therefore a reduction of the sound speed. However, the density of the mixture remains almost the same. Reflection, refraction, absorption, and scattering by bubbles all contribute to the attenuation of the sound.

When the void fraction is large ($> 10^{-2}$), the compressibility remains almost constant, while the speed and attenuation of the sound are mainly determined by the changes in density [20, 21] and not by the compressibility of the mixture.

field between two parallel rigid plates, a harmonic standing wave field will be established. The scheme for bubble measurement using a resonator is based on the theory about the resonance of this standing wave field and its interaction with bubbles. The harmonic frequencies depend on the distance between the two plates, and the signal will be attenuated in the presence of bubbles. This can be used to infer the number of bubbles at the different harmonic frequencies which correspond to a given bubble radius. In the following sections of this chapter, the sound attenuation caused by bubbles is discussed before the principles of the resonator is presented.

3.1 Total Scattering Cross Section

A bubble in a sound field with a frequency close to its resonance frequency will be driven into oscillation and reradiate or "scatter" a spherically symmetrical pressure wave (see section 2.1). The concept of total acoustical scattering cross section is used to measure the ability of a body to scatter the sound in all directions. The scattering cross section σ_s has the dimension of an area and is defined as

$$\sigma_s = \frac{\Pi_s}{I_p} = \frac{\int_0^{4\pi} I_s R^2 d\Omega}{I_p} = \int_0^{4\pi} \sigma d\Omega \quad (3.1)$$

Chapter 3

Acoustical Resonator Theory

When a wide-band sound source is used to excite a sound field between two parallel rigid plates, a harmonic standing wave field will be established. The scheme for bubble measurement using a resonator is based on the theory about the resonance of this standing wave field and its interaction with bubbles. The harmonic frequencies depend on the distance between the two plates, and the signal will be attenuated in the presence of bubbles. This can be used to infer the number of bubbles at the different harmonic frequencies which correspond to a given bubble radius. In the following sections of this chapter, the sound attenuation caused by bubbles is discussed before the principles of the resonator is presented.

3.1 Total Scattering Cross Section

A bubble in a sound field with a frequency close to its resonance frequency will be driven into oscillation and reradiate or "scatter" a spherically symmetrical pressure wave (see section 2.1). The concept of total acoustical scattering cross section is used to measure the ability of a body to scatter the sound in all directions. The scattering cross section σ_s has the dimension of an area and is defined as

$$\sigma_s \equiv \frac{\Pi_s}{I_p} = \frac{\int_0^{4\pi} I_s R^2 d\Omega}{I_p} = \int_0^{4\pi} \phi A d\Omega \quad (3.1)$$

where Π_s is the total power scattered over all angles, I_p and I_s are the intensities of the incident and scattered sound waves, R is the distance from the center of the scattering bubble, $d\Omega$ is the increment of solid angle, A the cross section of the projected area of the scatterer viewed from the source, and φ is defined as the scattering function of a body. At long ranges

$$I_p = P_p^2 / (\rho_A c), \quad (3.2)$$

and

$$n(a) da = \frac{\text{number of bubbles of radius between } a \text{ and } a+da}{I_s = P_s^2 / (\rho_A c)}, \quad (3.3)$$

and Eq. (3.1) can be written as [8]

$$\sigma_s = 4\pi \frac{|P_s|^2}{|P_p|^2} = \frac{4\pi a^2}{\left[\left((f_R/f)^2 - 1 \right)^2 + \delta^2 \right]}. \quad (3.4)$$

When the input sound frequency is equal to the resonance frequency, the scattering cross section reaches its maximum, which is

$$\sigma_s = \frac{4\pi a^2}{\delta_R^2}. \quad (3.5)$$

3.2 Extinction Cross Section

Since acoustic energy can be converted to heat during the oscillation of a bubble, a bubble not only scatters the wave but also absorbs the incident acoustic energy. The sum of the power scattered and absorbed by a bubble is the extinguished power, Π_e ,

$$\Pi_e = \Pi_s + \Pi_a. \quad (3.6)$$

The extinction cross section, σ_e , of a bubble is the sum of its absorption and scattering cross sections, which can be given as [8]

From Eq. (3.2) and the analogous $I_s = P_s^2 / (\rho_A c)$, we can further obtain

$$\sigma_e = \sigma_s + \sigma_a = \frac{4\pi a^2 (\delta/\delta_r)}{[(f_R/f) - 1]^2 + \delta^2}, \quad (3.7)$$

where $\delta_r = ka$ is the damping constant due to reradiation. Figure 3.1 shows σ_s and σ_e as functions of radius for four frequencies. The resonance peaks can be clearly seen.

When there are bubbles of various sizes present, the number of bubbles per unit volume must be defined in terms of the range of radii of interest. Since the number depends on the radius increment da , we define

$$n(a) da = \frac{\text{number of bubbles of radius between } a \text{ and } a+da}{\text{volume}}. \quad (3.8)$$

It is common to set da equal to one micron.

The extinction cross section per unit volume S_e for sound traversing a random mixture of noninteracting bubbles is calculated using (3.7) in the integration,

$$S_e = \int_0^{\infty} \sigma_e n(a) da = \int_0^{\infty} \frac{4\pi a^2 (\delta/\delta_r) n(a) da}{[(f_R/f)^2 - 1]^2 + \delta^2}. \quad (3.9)$$

3.3 Sound Attenuation by Bubbles

Assume that the bubbles are far enough apart to prevent interaction effects. Effectively, this will be true when the separation is greater than $\sqrt{\sigma_e}$ [8].

If the incident plane wave intensity is I_p , the power extinguished by all of the bubbles is $I_p S_e$, where S_e is calculated from Eq. (3.9). The change of intensity over a distance dx is

$$dI = -I_p S_e dx, \quad (3.10)$$

and by integrating, one gets

$$I_x = I_p \exp(-S_e x). \quad (3.11)$$

From Eq. (3.2) and the analogous $I_x = P_x^2 / (\rho_A c)$, we can further obtain

traversing distance x , the change in sound pressure level becomes

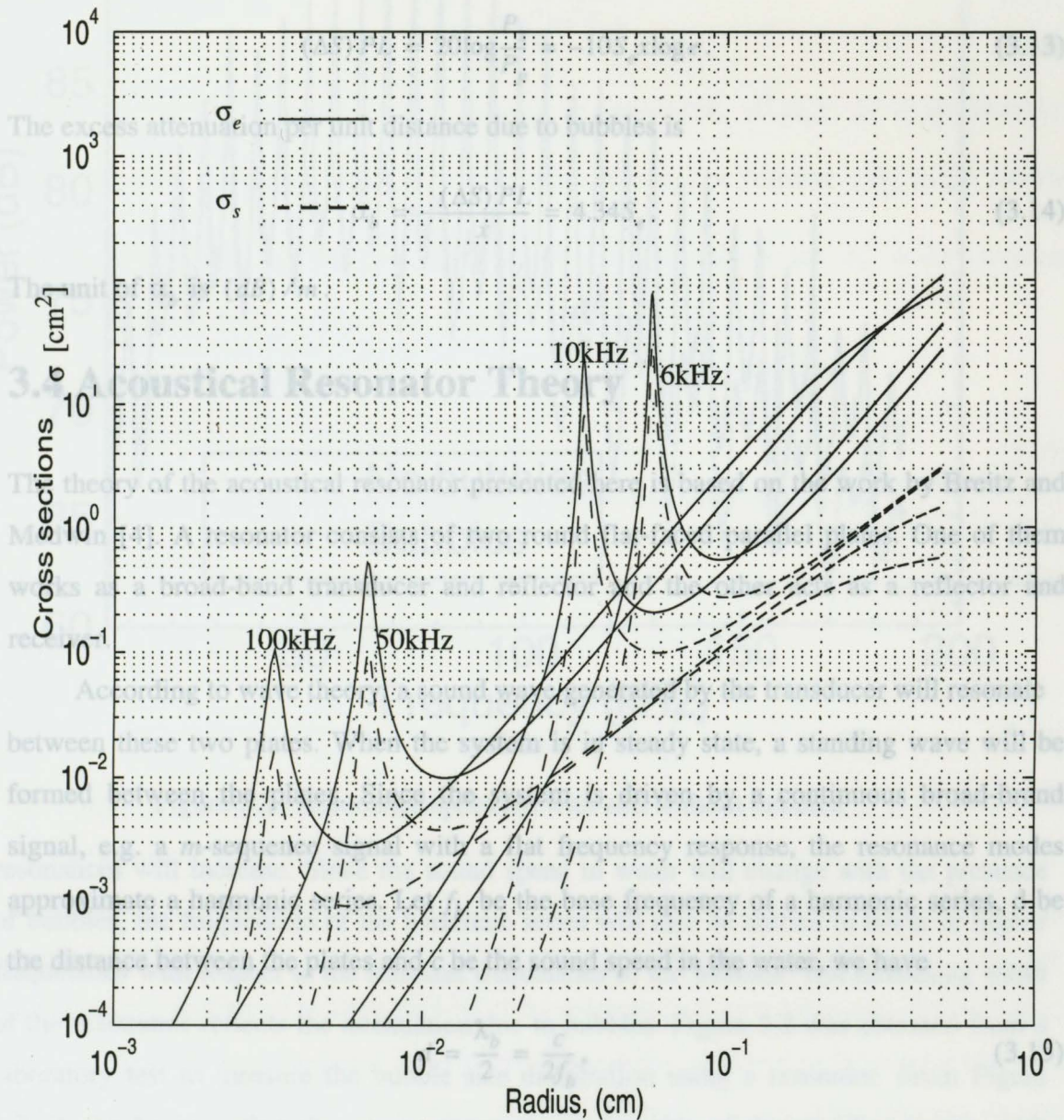


Figure 3.1 Extinction cross sections (solid lines) and total scattering cross sections (dashed lines) at four frequencies as a function of bubble radius. Air bubble in water at sea level.

where λ_0 is the base wavelength of the harmonic series. The half-power bandwidth of the resonance is slightly less than that given in Eq. (3.15) [3]. Figure 3.2 shows the power spectrum of the standing wave $P_x^2 = P_p^2 \exp(-S_e x)$. (3.12)

Note that the subscript x refers to the extinguished pressure (P_x) and intensity (I_x). After

traversing distance x , the change in sound pressure level becomes

$$(\Delta S) PL = 20 \log \frac{P_x}{P_p} = -10 S_e x \log e. \quad (3.13)$$

The excess attenuation per unit distance due to bubbles is

$$\alpha_b = -\frac{(\Delta S) PL}{x} = 4.34 S_e. \quad (3.14)$$

The unit of α_b is (dB)/m.

3.4 Acoustical Resonator Theory

The theory of the acoustical resonator presented here is based on the work by Breitz and Medwin [4]. A resonator consists of two round flat-faced parallel plates. One of them works as a broad-band transducer and reflector and the other acts as a reflector and receiver.

According to wave theory, a sound wave generated by the transducer will resonate between these two plates. When the system is in steady state, a standing wave will be formed between the plates. Since the system is driven by a continuous broad-band signal, e.g. a m -sequence signal with a flat frequency response, the resonance modes approximate a harmonic series. Let f_b be the base frequency of a harmonic series, d be the distance between the plates and c be the sound speed in the water, we have

$$d = \frac{\lambda_b}{2} = \frac{c}{2f_b}, \quad (3.15)$$

where λ_b is the base wavelength of the harmonic series. The half-power bandwidth of the n th mode is proportional to the damping factor of the system. As a result of the non-infinite terminating impedances, the separation of resonance frequencies for lower modes is slightly less than that given in Eq. (3.15) [3]. Figure 3.2 shows the power spectrum of the standing wave in the resonator.

With bubbles, the damping factor of the system will increase, and the width of the

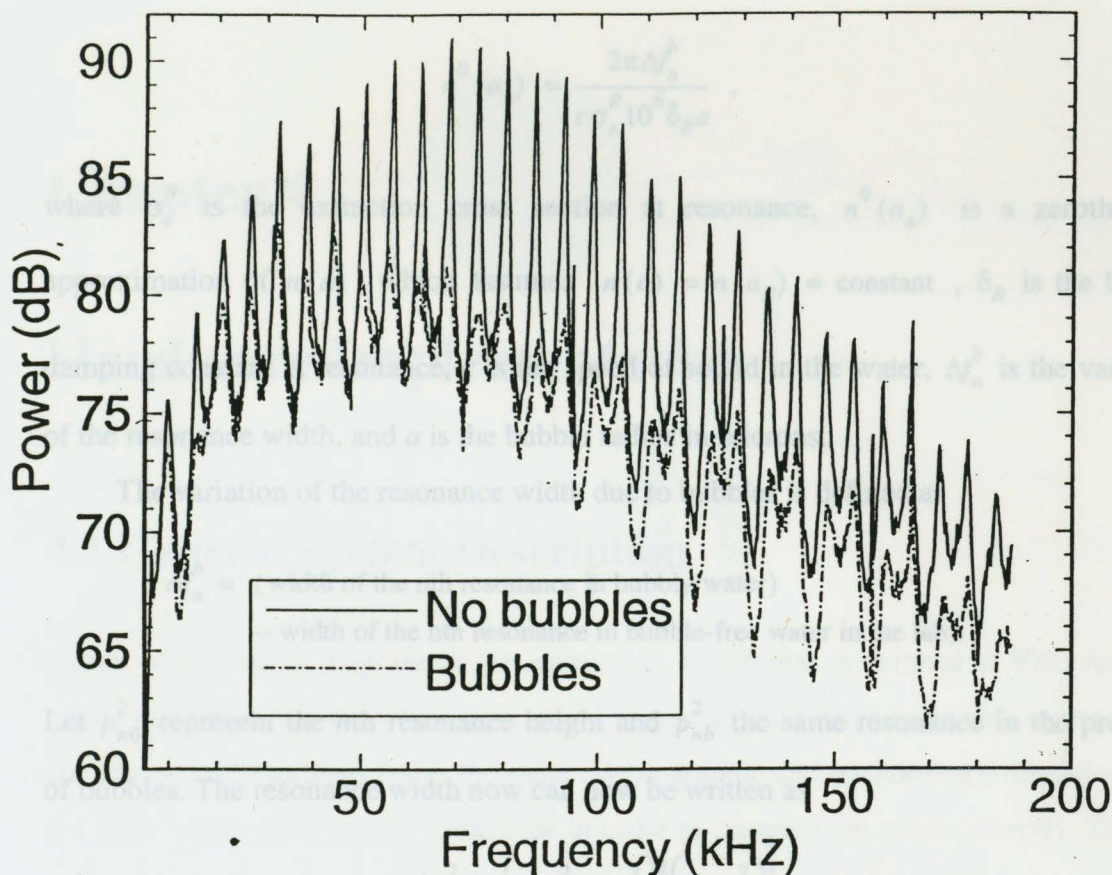


Figure 3.2 Resonance spectrum with and without bubbles.

resonances will increase. Since the sound speed in water will change with the presence of bubbles, the frequencies of the harmonic series will also be shifted to lower or higher frequencies with respect to the resonant frequencies of the bubbles. The increasing width of the resonance reflects the attenuation due to bubbles. Figure 3.2 was obtained from a laboratory test to measure the bubble size distribution using a resonator. From Figure 3.2, it can be seen that the power spectrum components of the standing waves with bubbles present are much smaller than those without bubbles.

The bubble distribution can be obtained by measuring the change of the resonance width or the resonance height. The equation to be used to estimate the bubble distribution is given by [4],

$$n^0(a_n) = \frac{2\pi\Delta f_n^b}{c\sigma_e^R 10^6 \delta_R a}, \quad (3.16)$$

where σ_e^R is the extinction cross section at resonance, $n^0(a_n)$ is a zeroth-order approximation of $n(a)$, which assumes $n(a) = n(a_R) = \text{constant}$, δ_R is the bubble damping constant at resonance, c is the speed of sound in the water, Δf_n^b is the variation of the resonance width, and a is the bubble radius in microns.

The variation of the resonance width due to bubbles is defined as

$$\Delta f_n^b = (\text{width of the } n\text{th resonance in bubbly water}) - (\text{width of the } n\text{th resonance in bubble-free water in the lab}). \quad (3.17)$$

Let p_{n0}^2 represent the n th resonance height and p_{nb}^2 the same resonance in the presence of bubbles. The resonance width now can now be written as

$$(\Delta f_n^b)^2 = \left(p_{no}^2 / p_{nb}^2 \right)^2 \left(\Delta f_{n0}^2 \right)^2, \quad (3.18)$$

showing that the resonance width in the presence of bubbles also can be estimated from the change in resonance height.

The sound speed c in Eq. (3.16) will change significantly when large numbers of bubbles are present. In such a case, if the change of the sound speed is not taken into account, the number of bubbles will be under-estimated or over-estimated, depending on the bubble sizes and resonance frequencies. The results presented in [4] were based on a small number of artificially generated bubbles. In order to get more accurate bubble distribution estimates, optimization techniques are needed. The equation for sound speed in bubbly water was introduced in section 2.3 (Eq. (2.7)).

The resonator consists of two 25 cm diameter piezoelectric transducers mounted approximately 12 cm apart. (See Section 4.3 for more details). The final structure of the sensor head is shown in Figure 4.2.

A digital signal processing chip, DSP32C, is used in the system to perform FFT

Chapter 4

Hardware Implementation

4.1 General System Description

Figure 4.1 shows a diagram of the instrument, which was developed at IOS. As mentioned in Section 1.4, the whole system is designed so as to make it possible to use different acoustical techniques under the same oceanographic and meteorologic conditions, i.e. the same water mass and the same time in order to compare the results directly. The system consists of two parts: a sound-speed sensor and an acoustical resonator.

All the electronics for the complete system is contained within a surface float. A short line (0.5 ~ 2.5 m) connects the float and a steel frame on which the transmitter and receiver hydrophones of the sound-speed sensor and the resonator transducer are mounted. The frame has a horizontal bar welded to a vertical bar. During some experiments, a profiling CTD (conductivity, temperature, density) instrument was mounted to the vertical bar and simultaneously recorded temperature, salinity and pressure where the acoustical sensors were deployed. The horizontal bar with a length of 1 m has the resonator mounted at one end and the sound-speed sensor at the other. The two transducers for the sound-speed sensor are rigidly mounted 0.4 m apart in the horizontal plane. The resonator consists of two 25 cm diameter piezoelectric transducers mounted approximately 12 cm apart. (See Section 4.3 for more details). The final structure of the sensor head is shown in Figure 4.2.

A digital signal processing chip, DSP32C, is used in the system to perform FFT

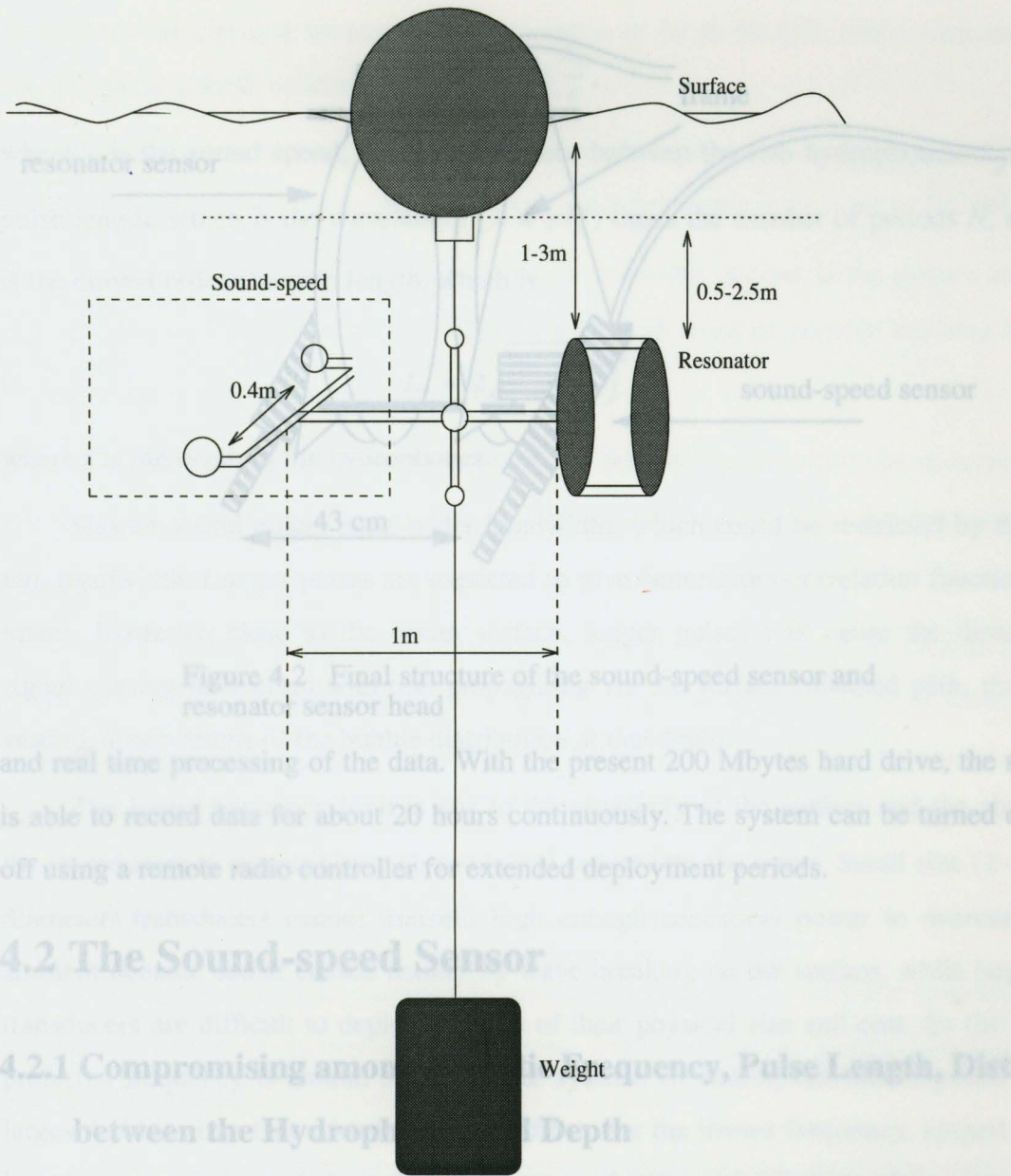


Figure 4.2 Final structure of the sound-speed sensor and resonator sensor head

and real time processing of the data. With the present 200 Mbytes hard drive, the system is able to record data for about 20 hours continuously. The system can be turned on and off using a remote radio controller for extended deployment periods.

4.2 The Sound-speed Sensor

4.2.1 Compromising among Frequency, Pulse Length, Distance

between the Hydrophone and Depth

One of the most important factors in the sound-speed measurements is to avoid multi-path effects which will make it difficult to detect the time delay of interest. Since our measurements are close to the ocean surface, the main concern in this regard is reflections from the ocean surface. The reflections from the edges of the resonator plates are very small and

Figure 4.1 Diagram of showing prototype of the sound-speed and acoustical resonator system developed at IOS.

travels from the transmitting hydrophone to the receiving hydrophone via direct path has

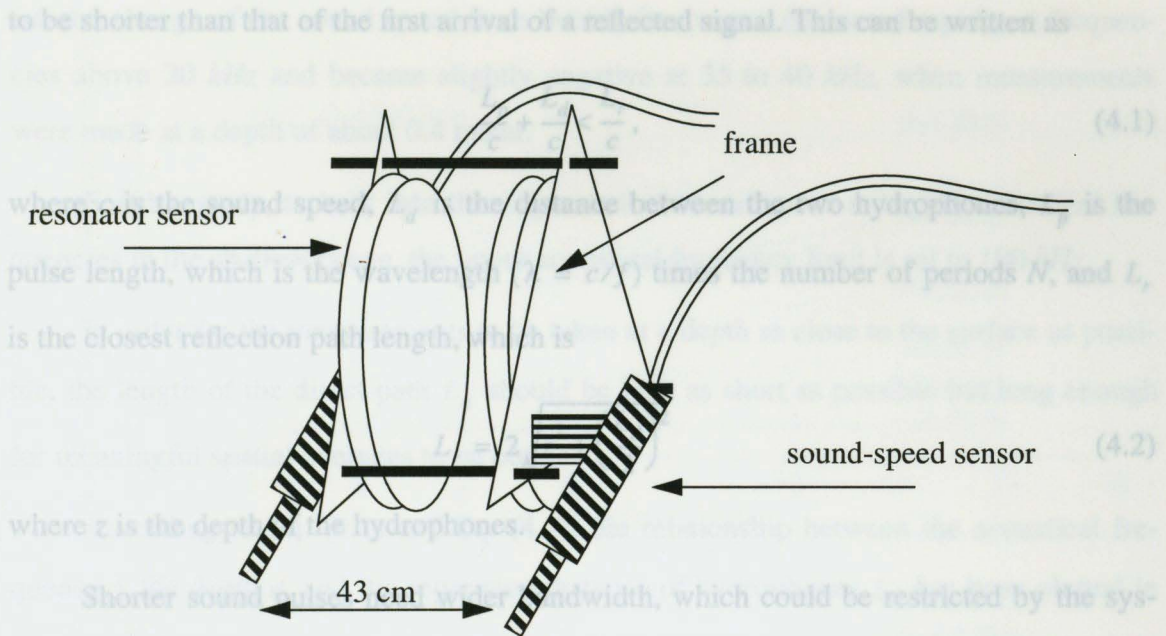


Figure 4.2. Final structure of the sound-speed sensor and resonator sensor head

and real time processing of the data. With the present 200 Mbytes hard drive, the system is able to record data for about 20 hours continuously. The system can be turned on and off using a remote radio controller for extended deployment periods.

4.2 The Sound-speed Sensor

4.2.1 Compromising among Acoustic Frequency, Pulse Length, Distance

between the Hydrophones and Depth

One of the most important factors in the sound-speed measurements is to avoid multipath effects which will make it difficult to detect the time delay of interest. Since our measurements are close to the ocean surface, the main concern in this regard is reflections from the ocean surface. The reflections from the edge of the resonator plates are very small and thus negligible. The time interval during which an entire acoustical pulse travels from the transmitting hydrophone to the receiving hydrophone via direct path has

to be shorter than that of the first arrival of a reflected signal. This can be written as

$$\frac{L_p}{c} + \frac{L_d}{c} < \frac{L_r}{c}, \quad (4.1)$$

where c is the sound speed, L_d is the distance between the two hydrophones, L_p is the pulse length, which is the wavelength ($\lambda = c/f$) times the number of periods N , and L_r is the closest reflection path length, which is

$$L_r = 2\sqrt{z^2 + \left(\frac{L_d}{2}\right)^2} \quad (4.2)$$

where z is the depth of the hydrophones.

Shorter sound pulses need wider bandwidth, which could be restricted by the system bandwidth. Longer pulses are expected to give better cross-correlation function estimates. However, close to the ocean surface, longer pulses will cause the direct path signal passing to overlap with that propagating via the surface reflected path, thus preventing observations of the bubble distribution at that depth.

The lower frequency limit is due to the proximity of the surface and the ability of the transducers to transmit enough acoustical power into the water. Small size (2 ~ 3 cm diameter) transducers cannot transmit high enough acoustical power to overcome the ambient oceanic sound caused mainly by wave breaking on the surface, while large size transducers are difficult to deploy because of their physical size and cost. So the lowest preferred frequency is around 5 kHz for our system. Of course, this also depends on the largest bubble sizes that contribute to the effect. For the lowest frequency, longest wavelength, two or three periods is the minimum to obtain good estimates of the time delay. This determines the shortest pulse lengths one can use.

The upper acoustical frequency limit can be determined by the lower bound of the bubble sizes in the shallow water of the ocean in which we are interested. Medwin et al. [25] have estimated from their field measurements of the sound speed at sea that the cut-off of the dispersive frequencies is at about 25 kHz. Their measurements were made at depths greater than 3 m. Eric Lamarre [20, 21] reported that the sound-speed anomaly,

i.e. the change of the sound speed from bubble free water, decreased rapidly at frequencies above 20 kHz and became slightly negative at 35 to 40 kHz, when measurements were made at a depth of about 0.4 meter.

For this study, to look into the dispersion of sound speed at higher acoustical frequencies in the shallow ocean, the upper acoustical frequency limit is set to 100 kHz.

In order for the measurements to be taken at a depth as close to the surface as possible, the length of the direct path L_d should be kept as short as possible but long enough for meaningful spatial averages to be obtained.

According to Eq. (4.1) and Eq. (4.2), the relationship between the acoustical frequency f , the depth d , and the separation distance of hydrophones L_d has been plotted in Figure 4.3, where the number of periods N is set to two.

From the plot, by adjusting the acoustical frequency, the depth, as well as the distance between the transmit and receiver hydrophones, the depth d can be as small as 0.4 m if the separation distance of the two hydrophones, L_d , is 0.4 m and the frequency is 6 kHz.

4.2.2 The Sound-speed Sensor

The sound-speed sensor is designed to obtain sound-speeds at different acoustical frequencies by using cross correlation techniques. Figure 4.4 shows a block diagram of the sound-speed sensor.

An acoustical system, including transmitter, receiver and the bubbly water, has a limited bandwidth. When a wide bandwidth acoustical pulse, e.g. a square wave, passes through the system, it will be distorted. Therefore, the shape of the pulse should be carefully selected to reduce this distortion. In this study, a Hanning window is used to shape the output pulse.

A short shaped acoustical pulse generated by a 386 personal computer is used to modulate carrier signals ranging from 5 kHz to 96 kHz. The bubbly water has a response

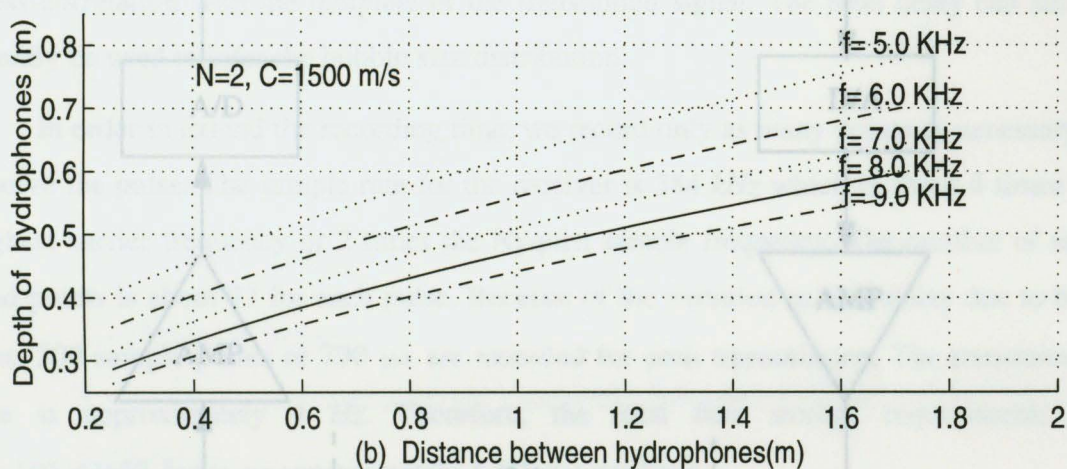
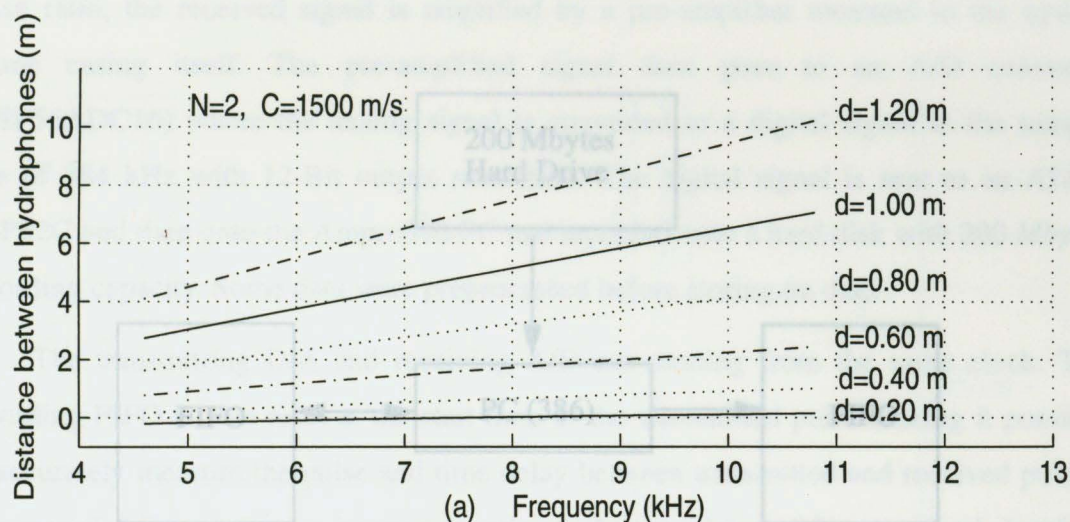


Figure 4.3 Relationship between frequency, depth and hydrophone separation for pulses with a duration of 2 cycles.

that depends on carrier frequency. The carrier signal can be a single frequency signal or a multi-frequency signal. The total pulse length is about 2 cycles of the lowest carrier frequency, and is approximately $200 \mu\text{s}$ for 5 kHz . The output waveform is then passed to a repeatable FIFO (IDT72104). The output digital sequence from the FIFO is converted to an analog signal by a D/A converter (AD558). The analog signal is then amplified and sent to the transmitting hydrophone. Usually, a transmitting transducer has a narrow bandwidth. To obtain a wide bandwidth, a modified EDO hydrophone model 6104 is

noise ratio, the received signal is amplified by a pre-amplifier mounted in the hydrophone casing itself. The pre-amplified signal then goes to an A/D converter (DSP56ADC16) where the analog signal is converted to a digital signal at the sample rate of 384 kHz with 12-Bit output. The digital signal is sent to an AT&T DSP32C and then onto the Ampro PC which records onto a hard disk with 200 Mbytes recording capacity. Some data were preprocessed before storing on disc.

The transmitting D/A and receiving D/A are running from the same clock. The recording FIFO runs at the start of the transmitted pulse making it possible to accurately measure the pulse and time delay between transmitted and received pulses. The recorded time series can be used to estimate the time delay of the acoustical signal by cross-correlation with the template of the transmitted signal. The time delay can subsequently be used to estimate the bubble size distribution.

In order to extend the recording time, we record only as many points as necessary to resolve the pulse. The sample rate for the receiver is 384 kHz which is about 4 times the highest carrier frequency or 2 times the Nyquist sample frequency. The number of sampled points is about 77 for each pulse. Because of the variation in time delay due to bubbles, 300 samples or 790 μ s are recorded for each transmission. The transmission rate is approximately 4 Hz. Therefore, the total data storage requirements are 4 \times 300 \times 3600 bytes, or approximately 4 Mbytes per hour.

4.3 Resonator Sensor

A block diagram of the resonator sensor is shown in Figure 4.5. A white noise generator consisting of a series of shift registers generates an m -sequence which has a flat power spectrum from 0 to more than 200 kHz. This white noise signal is sent to a power amplifier to generate a high power signal. The signal is then sent to a transmitting transducer. The receiver is also an EDO hydrophone model 6104. In order to increase signal to

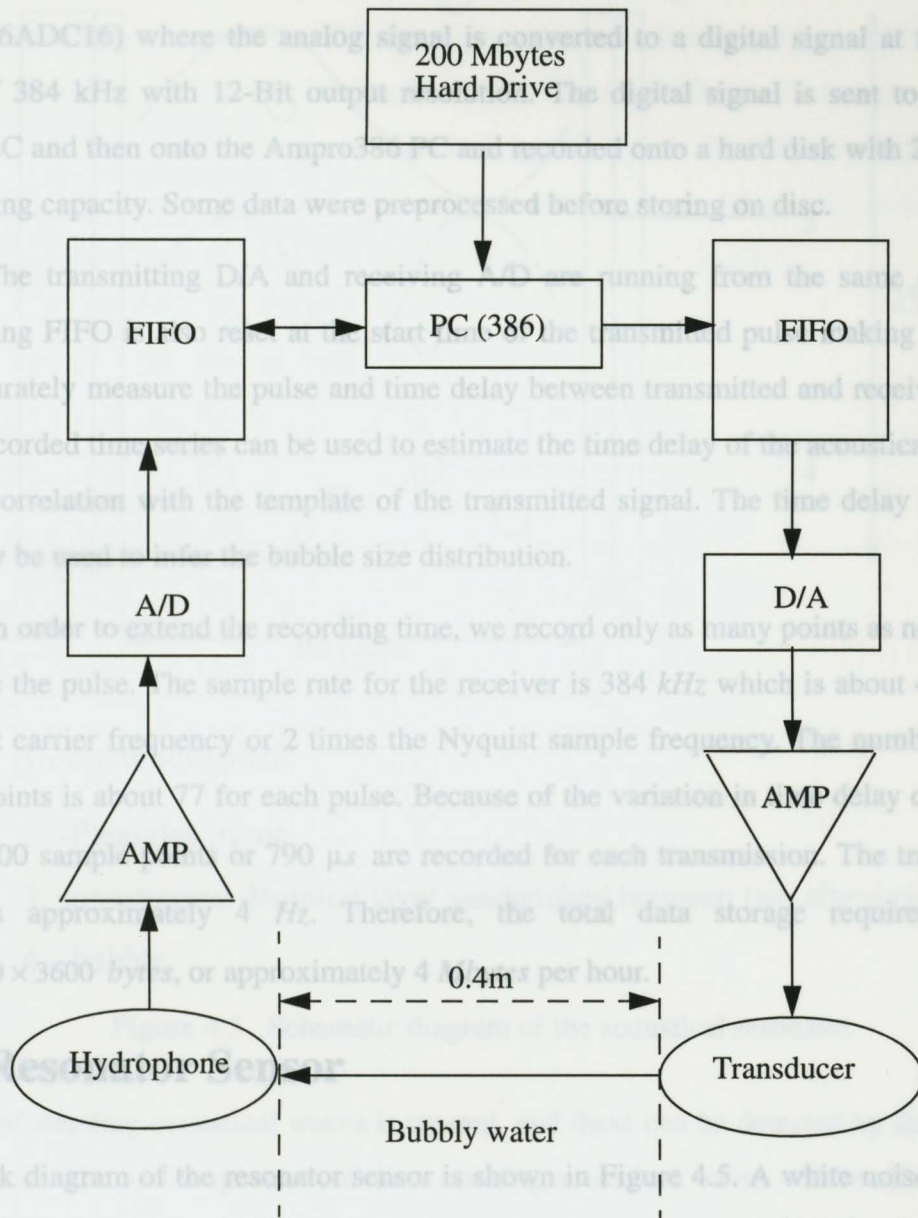


Figure 4.4 Block diagram of the sound-speed sensor.

used as a transmitting transducer.

The receiver is also an EDO hydrophone model 6104. In order to increase signal to

noise ratio, the received signal is amplified by a pre-amplifier mounted in the hydrophone casing itself. The pre-amplified signal then goes to an A/D converter (DSP56ADC16) where the analog signal is converted to a digital signal at the sample rate of 384 kHz with 12-Bit output resolution. The digital signal is sent to an AT&T DSP32C and then onto the Ampro386 PC and recorded onto a hard disk with 200 *Mbytes* recording capacity. Some data were preprocessed before storing on disc.

The transmitting D/A and receiving A/D are running from the same clock. The recording FIFO is also reset at the start time of the transmitted pulse making it possible to accurately measure the pulse and time delay between transmitted and received pulses. The recorded time series can be used to estimate the time delay of the acoustical signal by cross-correlation with the template of the transmitted signal. The time delay can subsequently be used to infer the bubble size distribution.

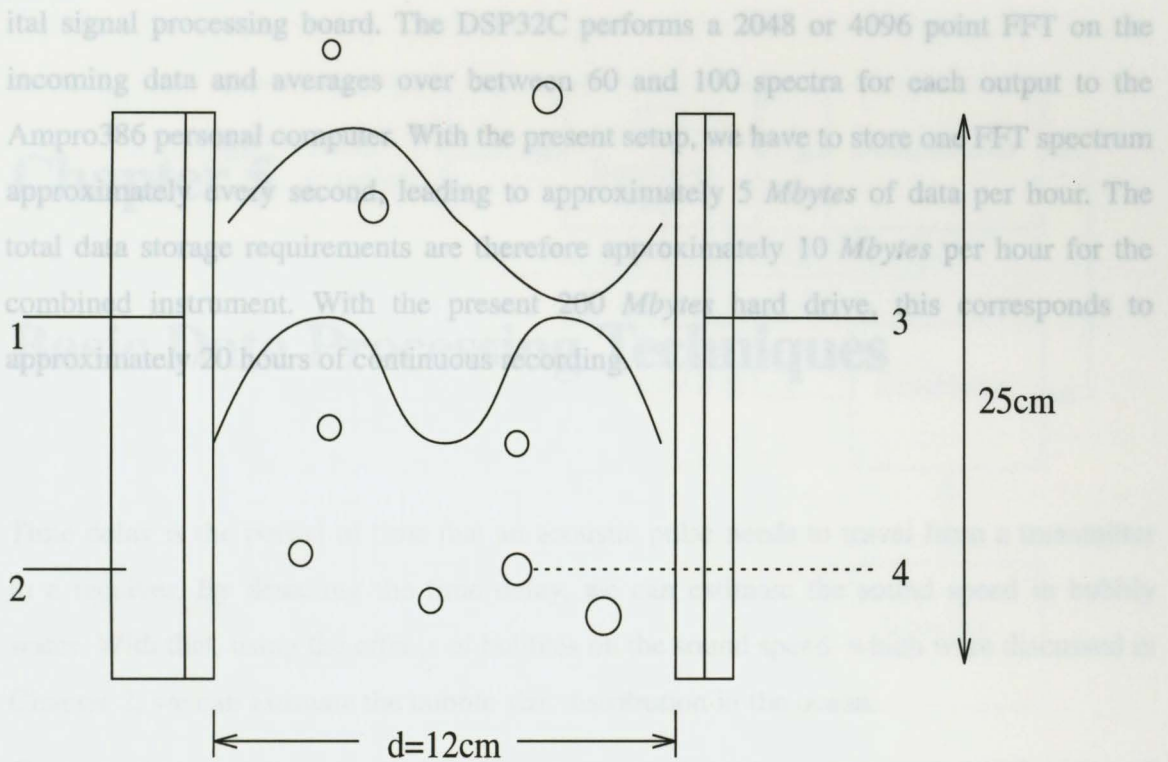
In order to extend the recording time, we record only as many points as necessary to resolve the pulse. The sample rate for the receiver is 384 *kHz* which is about 4 times the highest carrier frequency or 2 times the Nyquist sample frequency. The number of sampled points is about 77 for each pulse. Because of the variation in time delay due to bubbles, 300 sample points or 790 μs are recorded for each transmission. The transmission rate is approximately 4 *Hz*. Therefore, the total data storage requirements are $4 \times 300 \times 3600$ *bytes*, or approximately 4 *Mbytes* per hour.

Figure 4.5 Schematic diagram of the acoustical resonator.

4.3 Resonator Sensor

A block diagram of the resonator sensor is shown in Figure 4.5. A white noise generator consisting of a series of shift registers generates an *m*-sequence which has a flat power spectrum from 0 to more than 200 *kHz*. This white noise signal is sent to a power amplifier to generate enough power to drive the transmitting transducer.

The acoustical resonator consists of two 25 *cm* diameter piezoelectric transducers being mounted parallel with a separation of 12 *cm*. One transducer acts as a transmitter and the other as a receiver. From the white noise signal transmitted into the cavity, a



- 1.--aluminum plate;
- 2.--Plexiglas frame;
- 3.--constrained damping layer sandwiched between two aluminum plates;
- 4.--bubble

Figure 4.5 Schematic diagram of the acoustical resonator.

series of standing acoustical waves is created, and these can be detected by the receiving transducer. The power spectrum of these standing acoustical waves will be affected by the presence of bubbles in the volume between the plates. A preamplifier mounted next to the receiving transducer is used to increase the signal strength and reduce electrical noise which could be introduced through the cable connecting the sensor head and the receiver electronics.

The amplified signal is sent to an A/D converter (56ADC16). The A/D converter has a digitizing rate of 396 kHz and the digitized signal is routed to a AT&T DSP32C dig-

ital signal processing board. The DSP32C performs a 2048 or 4096 point FFT on the incoming data and averages over between 60 and 100 spectra for each output to the Ampro386 personal computer. With the present setup, we have to store one FFT spectrum approximately every second, leading to approximately 5 *Mbytes* of data per hour. The total data storage requirements are therefore approximately 10 *Mbytes* per hour for the combined instrument. With the present 200 *Mbytes* hard drive, this corresponds to approximately 20 hours of continuous recording.

Time delay is the period of time that an acoustic pulse needs to travel from a transmitter to a receiver. By detecting the time delay, we can estimate the sound speed in bubbly water. With that, using the effects of bubbles on the sound speed, which were discussed in Chapter 2, we can estimate the bubble size distribution in the ocean.

The time delay can be estimated by locating the peak of the cross-correlation function of the received pulse and the transmitted pulse. In this chapter some basic data processing principles related to detecting the time delay are presented.

5.1 General Description of Data Processing for Bubble Distribution Estimation

When an acoustic signal is received, it is first low-pass filtered and then digitized by an A/D converter as shown in Figure 4.4. This digitized acoustic signal is now ready for processing so as to estimate the bubble size distributions. Figure 5.1 is a block diagram showing the procedure used for the bubble distribution estimation.

The recorded signal is sent to a trend-remover to remove any unwanted trends, i.e. low-frequency components whose wavelengths are longer than those of the received signal. Trends are usually caused by ambient noise and can not be removed simply by high pass filtering because of the transient process of the high pass filter. The most commonly used technique for trend removal is to fit a low-order polynomial to the data and then

Chapter 5

Basic Data Processing Techniques

Time delay is the period of time that an acoustic pulse needs to travel from a transmitter to a receiver. By detecting the time delay, we can estimate the sound speed in bubbly water. With that, using the effects of bubbles on the sound speed, which were discussed in Chapter 2, we can estimate the bubble size distribution in the ocean.

The time delay can be estimated by locating the peak of the cross-correlation function of the received pulse and the transmitted pulse. In this chapter some basic data processing principles related to detecting the time delay are presented.

5.1 General Description of Data Processing for Bubble Distribution Estimation

When an acoustic signal is received, it is first low-pass filtered and then digitized by an A/D converter as shown in Figure 4.4. This digitized acoustic signal is now ready for processing so as to estimate the bubble size distributions. Figure 5.1 is a block diagram showing the procedure used for the bubble distribution estimation.

The recorded signal is sent to a trend-remover to remove any unwanted trends, i.e. low-frequency components whose wavelengths are longer than those of the recorded signal. Trends are usually caused by ambient noise and can not be removed simply by high pass filtering because of the transient process of the high pass filter. The most commonly used technique for trend removal is to fit a low-order polynomial to the data using least-

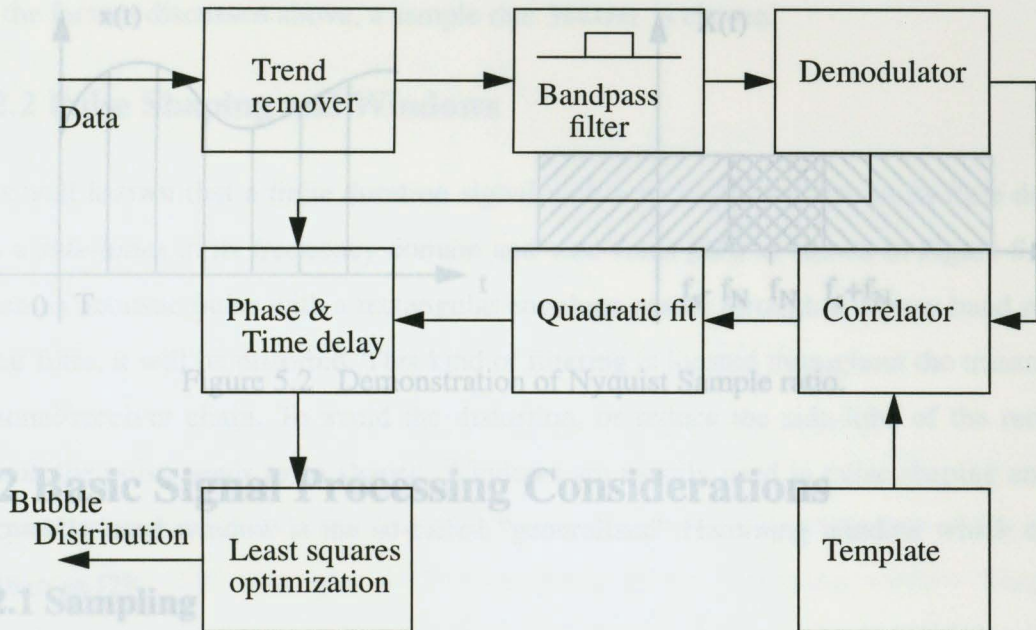


Figure 5.1 Block diagram of data processing used to obtain bubble distribution.

squares. The signal is then bandpass filtered to eliminate noise outside the signal band. When a multi-tone signal is used, this filter block becomes a bank of filters to recover each single tone signal. In order to get better time-delay estimation, each single-tone signal is decomposed into in-phase and quadrature components by a demodulator. The envelope of each single-tone signal, which is the output of the demodulator, is cross-correlated with the envelope of a template. The template is obtained by an ensemble average of the received acoustic pulses recorded in bubble-free water. To improve the accuracy of the time-delay estimations a quadratic curve is used to fit the cross-correlation function by a least-squares procedure. The time-delay estimation is improved further by using the phase information determined by the in-phase and quadrature components (See sections 5.3.3 and 5.3.4). Thus the variance of the estimated delay can be reduced significantly. Bubble distributions can now be inferred, using the estimated sound speed and the equations introduced in section 2.3, with suitable optimization techniques.

research, the highest frequency of interest is up to $100kHz$. Taking into consideration of all the factors discussed above, a sample rate $384kHz$ is chosen.

5.2.2 Pulse Shaping and Windows

It is well known that a finite duration signal with a rectangular shape in its time domain has a *side-lobes* in its frequency domain and vice versa [30], as shown in Figure 5.3. So, when an acoustic pulse with a rectangular envelope passes through a narrow band rectangular filter, it will be distorted. This kind of filtering is located throughout the transmitter/channel/receiver chain. To avoid the distortion, or reduce the side-lobe of the received signal, the pulse needs to be shaped. Windows are usually used in pulse shaping and one frequently used window is the so-called “generalized” Hamming window which can be written as [2]

$$W_H = \begin{cases} \alpha + (1 - \alpha) \cos\left(\frac{2\pi n}{N}\right) & -\left(\frac{N-1}{2}\right) \leq n \leq \left(\frac{N-1}{2}\right) \\ 0 & \text{elsewhere} \end{cases} \quad (5.1)$$

where α is in the range $0 \leq \alpha \leq 1.0$. If $\alpha = 0.54$, the window is called a Hamming window; if $\alpha = 0.5$, it is called a Hanning window.

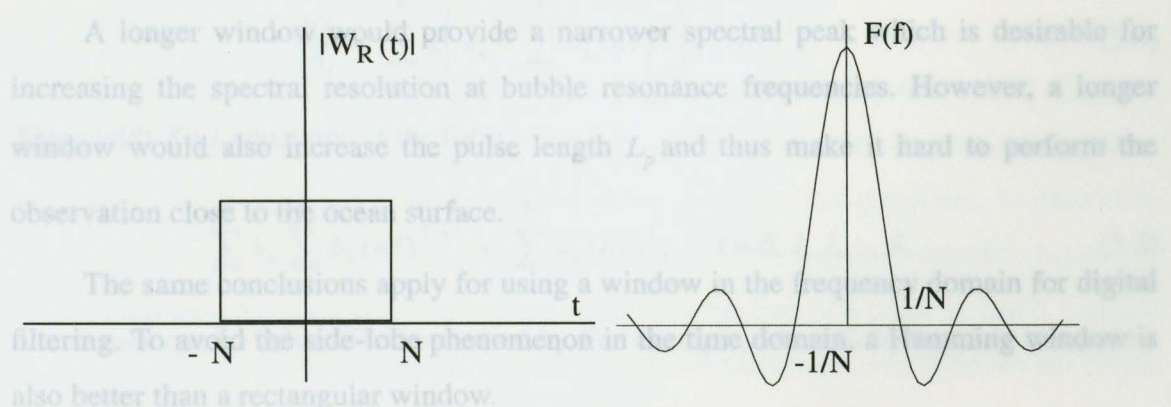


Figure 5.3 Rectangular window and side-lobes.

5.2.3 Trend Removal

The frequency response of a Hamming window is shown in Figure 5.4. A comparison of Figure 5.3 and Figure 5.4 shows that the main lobe of the frequency response of

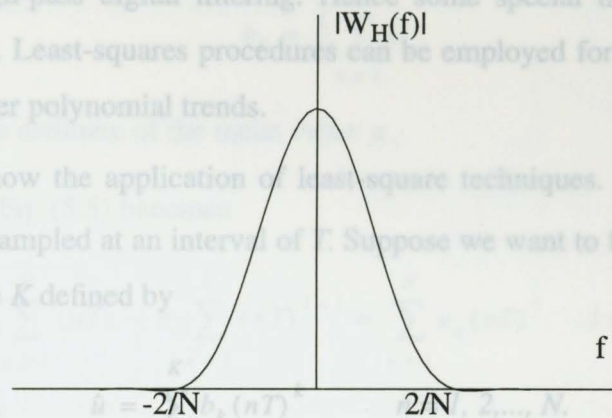


Figure 5.4 Frequency response of Hamming window.

the Hamming window is twice the width of the main lobe of the frequency of the rectangular window. The side lobe of the amplitude of the Hamming window frequency response is considerably smaller, however, than the side lobe amplitudes of the rectangular window frequency response. For $\alpha = 0.54$, i.e. the conventional Hamming window, 99.96% of the spectral energy is in the main lobe and the peak side lobe ripple is down about 40 dB from the main lobe peak. In contrast, for the rectangular window, the spectral side lobes are down only about 13 dB from the main lobe peak.

A longer window would provide a narrower spectral peak which is desirable for increasing the spectral resolution at bubble resonance frequencies. However, a longer window would also increase the pulse length L_p and thus make it hard to perform the observation close to the ocean surface.

The same conclusions apply for using a window in the frequency domain for digital filtering. To avoid the side-lobe phenomenon in the time domain, a Hamming window is also better than a rectangular window.

5.2.3 Trend Removal

Trends are defined as any frequency component whose period is longer than the recorded data length. These components may need to be removed. However, they cannot be

removed by high-pass digital filtering. Hence some special trend removal techniques must be applied. Least-squares procedures can be employed for the removal of linear as well as high-order polynomial trends.

Consider now the application of least-square techniques. Let u_n , $n=1, 2, \dots, N$, be the data values sampled at an interval of T . Suppose we want to fit these data with a polynomial of degree K defined by

$$\hat{u} = \sum_{k=0}^K b_k (nT)^k \quad n = 1, 2, \dots, N. \quad (5.2)$$

In a least-squares fit, the set of coefficients b_k are chosen so as to minimize the expression,

$$Q(b) = \sum_{n=1}^N (u_n - \hat{u}_n)^2 = \sum_{n=1}^N \left[u_n - \sum_{k=0}^K b_k (nT)^k \right]^2, \quad (5.3)$$

which is always non-negative for any choice of b_0, b_1, \dots, b_K . The desired coefficients can be obtained by taking partial derivatives of Eq. (5.3) with respect to b_l and letting them equal zero,

$$\frac{\partial Q}{\partial b_l} = \sum_{n=1}^N 2 \left(u_n - \sum_{k=0}^K b_k (nT)^k \right) [-(nT)^l]. \quad (5.4)$$

This yields $K+1$ equations of the form

$$\sum_{k=0}^K b_k \sum_{n=1}^N b_k (nT)^{k+l} = \sum_{n=1}^N u_n (nT)^l, \quad l = 0, 1, 2, \dots, K, \quad (5.5)$$

which now can be solved for the desired b_k . For example, when $K=0$, Eq. (5.5) becomes

$$b_0 \sum_{n=1}^N (nT)^0 = \sum_{n=1}^N u_n (nT)^0, \quad (5.6)$$

giving the result

$$b_0 = \frac{1}{N} \sum_{n=1}^N u_n. \quad (5.7)$$

Note that b_0 is an estimate of the mean value μ .

For $K = 1$, Eq. (5.5) becomes

$$b_0 \sum_{n=1}^N (nT)^l + b_1 \sum_{n=1}^N (nT)^{1+l} = \sum_{n=1}^N u_n (nT)^l \quad l = 0, 1. \quad (5.8)$$

giving the results

$$b_0 = \frac{2(2N+1) \sum_{n=1}^N u_n - 6 \sum_{n=1}^N nu_n}{N(N-1)}, \quad (5.9)$$

$$b_1 = \frac{12 \sum_{n=1}^N nu_n - 6(N+1) \sum_{n=1}^N u_n}{TN(N-1)(N+1)}, \quad (5.10)$$

providing a least-square method to remove a linear trend in data. Second and third-order polynomials are also practical with this method. A case of linear trend removal is illustrated in Figure 5.5.

Trend removal is an important step in the digital processing of random data and should be given its due consideration. If trends are not eliminated in data, large distortions can occur in the later processing of correlation and spectral quantities. In particular, trends in data can completely nullify the estimation of low-frequency spectral content. In some situations, knowledge of these trends may be a desired end result in itself. Caution is advised here, however, that trend removal should be performed only if trends are physically expected or clearly apparent in the data.

5.3 Time-delay Estimation

5.3.1 Demodulation

By finding the location of the peak of a cross-correlation function, which will be discussed in section 5.3.2, we can estimate the time delay of a received signal. Because of the relatively low sampling rate, which is 384kHz in our case, compared to the highest acoustic frequency we are interested in, which is near 100kHz, it is hard to use direct interpolation techniques to increase the resolution of the time-delay estimation (refer to section 5.3.5). Also a high frequency component in a cross-correlation function will increase the variation of the time-delay estimation [7]. In fact, the high frequency component in a pulse is just a carrier, which carries a shaped pulse from the transmitter to the receiver. After the pulse has been received, the carrier signal is no longer useful in the cross correlation. The time for the pulse to travel from the transmitter to the receiver can be determined by finding the peak of the cross correlation function of the transmitted signal and the received signal, or that of the cross correlation function of the envelopes of these signals. Since the cross-correlation function of the envelope is much smoother than the direct cross-correlation of the transmitted and the received signals, using interpolation, as introduced in section 5.3.5, will be more efficient.

A schematic diagram of demodulation is shown in Figure 5.6, where a signal is decomposed into two orthogonal parts, i.e. $\hat{u}(t) = b_0 + b_1 t$ and quadrature, and the envelope of the signal is then obtained by summing the squared in-phase and quadrature components. The in-phase and quadrature components contain phase information of the pulse, which can be used to reduce the variation of the time-delay estimation. Use of the phase information will be discussed in section 5.3.4.

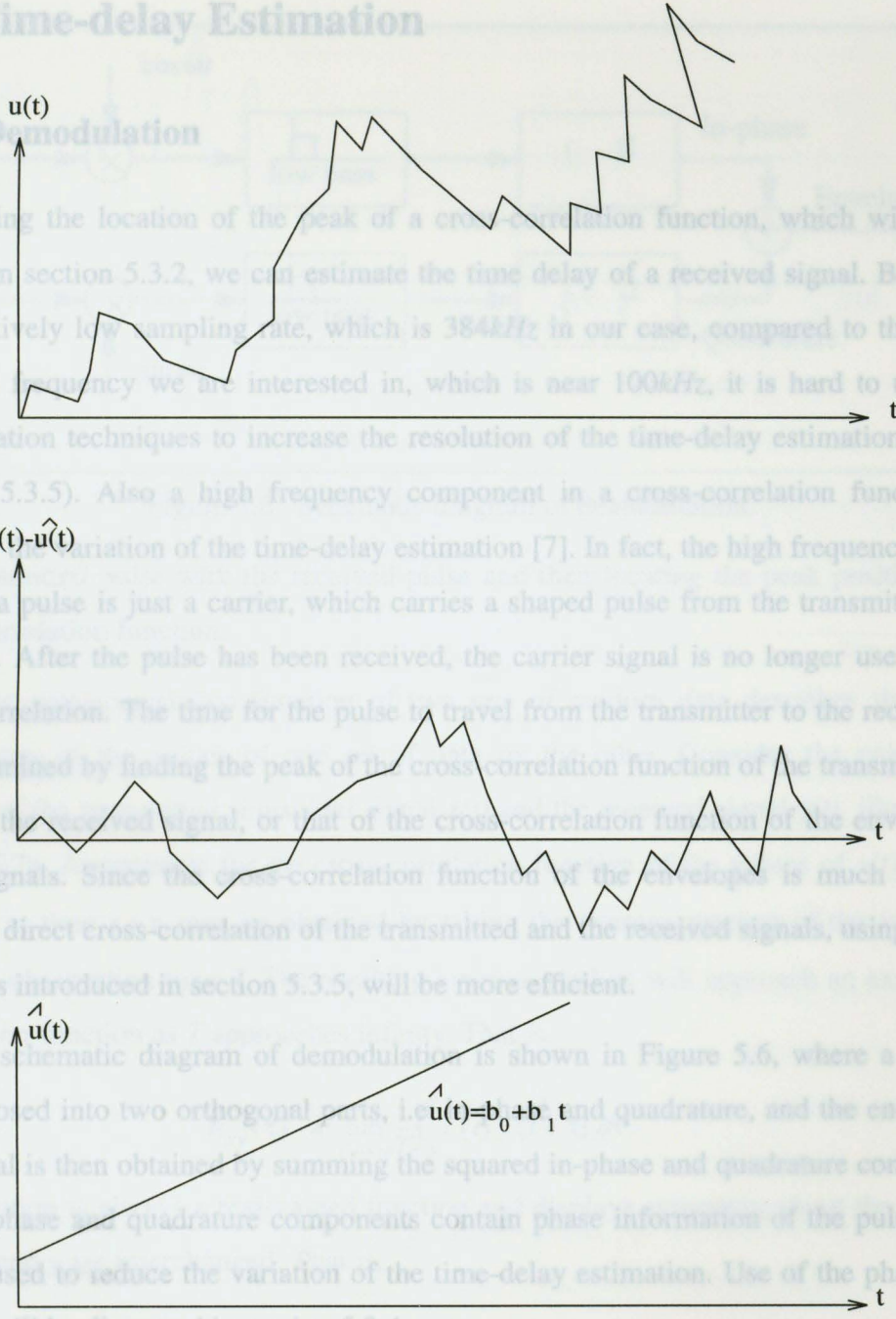


Figure 5.5 Illustration of linear trend removal.

5.3.2 Cross Correlation

Sound speed can be estimated by detecting the time during which a sound wave travels from the transmitter to the receiver. The time delay can be obtained by cross-correlating

5.3 Time-delay Estimation

5.3.1 Demodulation

By finding the location of the peak of a cross-correlation function, which will be discussed in section 5.3.2, we can estimate the time delay of a received signal. Because of the relatively low sampling rate, which is 384kHz in our case, compared to the highest acoustic frequency we are interested in, which is near 100kHz , it is hard to use direct interpolation techniques to increase the resolution of the time-delay estimation (refer to section 5.3.5). Also a high frequency component in a cross-correlation function will increase the variation of the time-delay estimation [7]. In fact, the high frequency component in a pulse is just a carrier, which carries a shaped pulse from the transmitter to the receiver. After the pulse has been received, the carrier signal is no longer useful in the cross correlation. The time for the pulse to travel from the transmitter to the receiver can be determined by finding the peak of the cross-correlation function of the transmitted signal and the received signal, or that of the cross-correlation function of the envelopes of these signals. Since the cross-correlation function of the envelopes is much smoother than the direct cross-correlation of the transmitted and the received signals, using interpolation, as introduced in section 5.3.5, will be more efficient.

A schematic diagram of demodulation is shown in Figure 5.6, where a signal is decomposed into two orthogonal parts, i.e. in-phase and quadrature, and the envelope of the signal is then obtained by summing the squared in-phase and quadrature components. The in-phase and quadrature components contain phase information of the pulse, which can be used to reduce the variation of the time-delay estimation. Use of the phase information will be discussed in section 5.3.4.

5.3.2 Cross Correlation

Sound speed can be estimated by detecting the time during which a sound wave travels from the transmitter to the receiver. The time delay can be obtained by cross-correlating

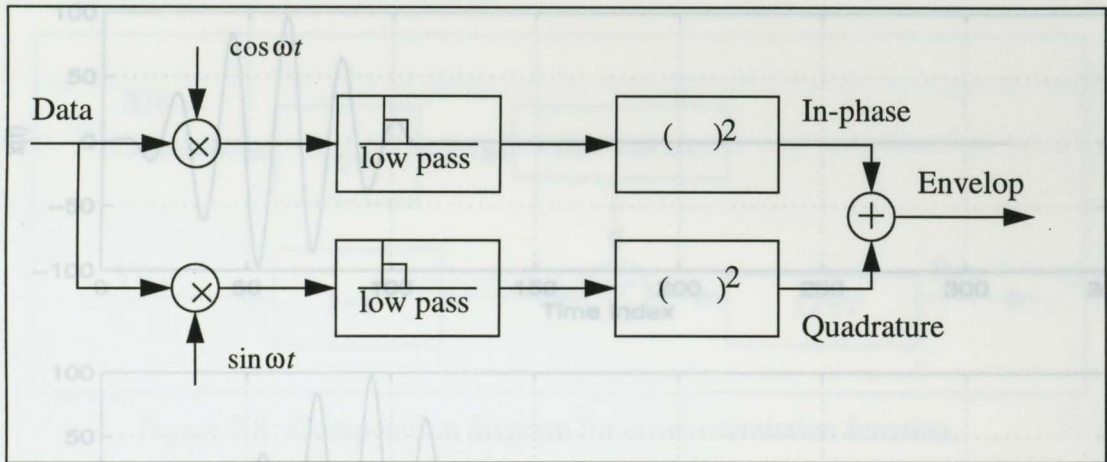


Figure 5.6 Schematic diagram of demodulation.

the transmitted pulse with the received pulse and then locating the peak position of the cross-correlation function.

The cross-correlation function of two sets of random data describes the general dependence of the values of one set of data on the other. Consider the pair of time records of the transmitted sinusoidal signal $x(t)$ and the received signal $y(t)$, illustrated in Figure 5.7a. An estimate for the cross-correlation function of the values of $x(t)$ at time t and $y(t)$ at time $t + \tau$ may be obtained by taking the average product of the two values over the observation time T . The resulting average product will approach an exact cross-correlation function as T approaches infinity. That is,

$$R_{xy}(\tau) = \lim_{T \rightarrow \infty} \frac{1}{T} \int_0^T x(t) y(t + \tau) dt. \quad (5.11)$$

The function is always a real-valued function and displays symmetry about the ordinates when x and y are interchanged. That is,

$$R_{xy}(-\tau) = R_{yx}(\tau). \quad (5.12)$$

When $R_{xy}(\tau) = 0$, $x(t)$ and $y(t)$ are said to be uncorrelated. Further, if $x(t)$ and $y(t)$ are statistically independent, then $R_{xy}(\tau) = 0$ for all time displacements τ . For our considerations here, when the displacement makes the received signal perfectly match the transmitted signal, the cross-correlation function reaches a peak as illustrated in Figure 5.7b.

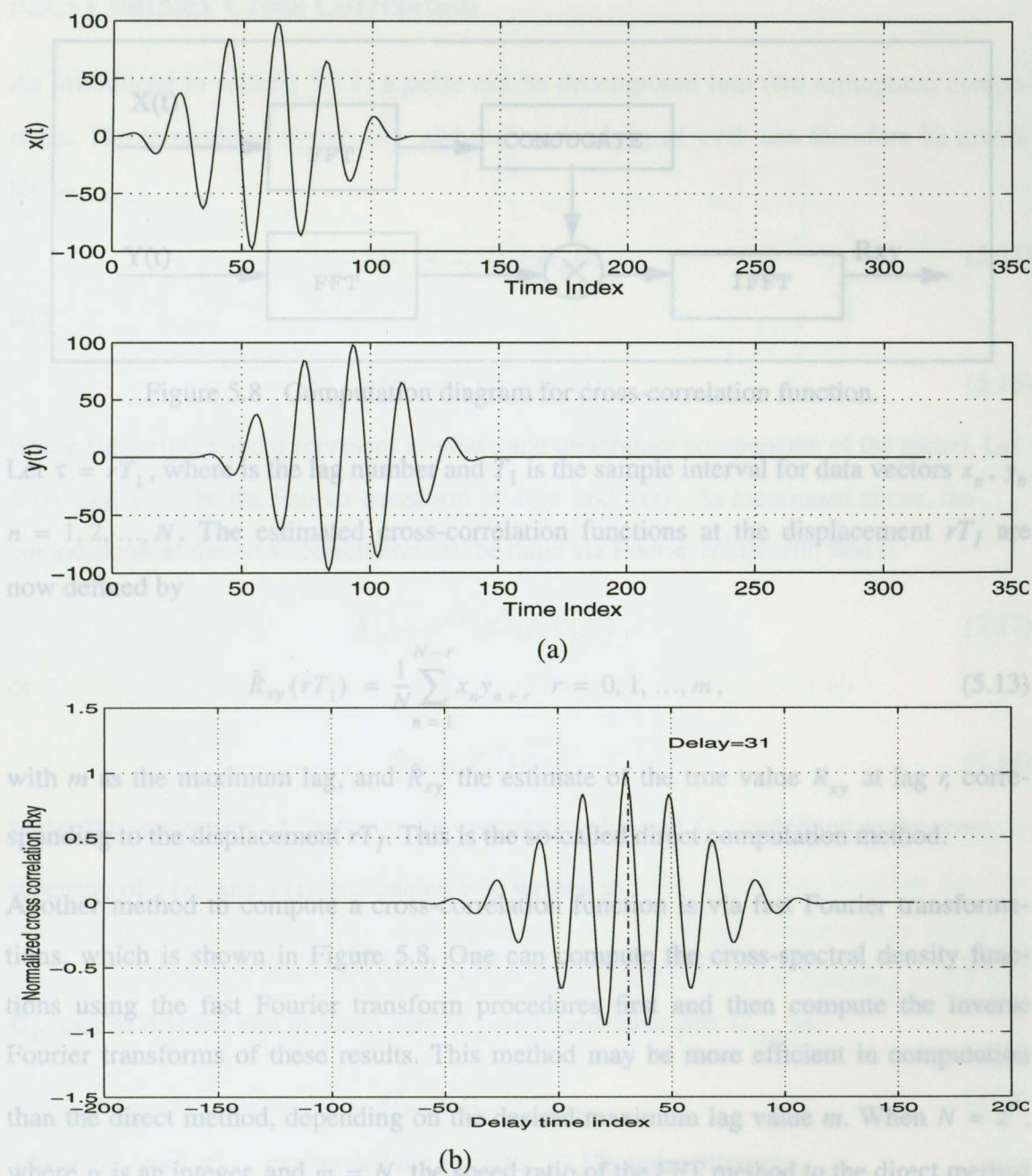


Figure 5.7 Demonstration of cross correlation.

However, in practice, there is always some noise added to the received signal, thus affecting the accuracy of the detected delay.

For digitized signals there are basically two approaches to estimating cross-correlation functions, called the direct computation and the roundabout FFT method.

5.3.3 Complex Cross Correlation

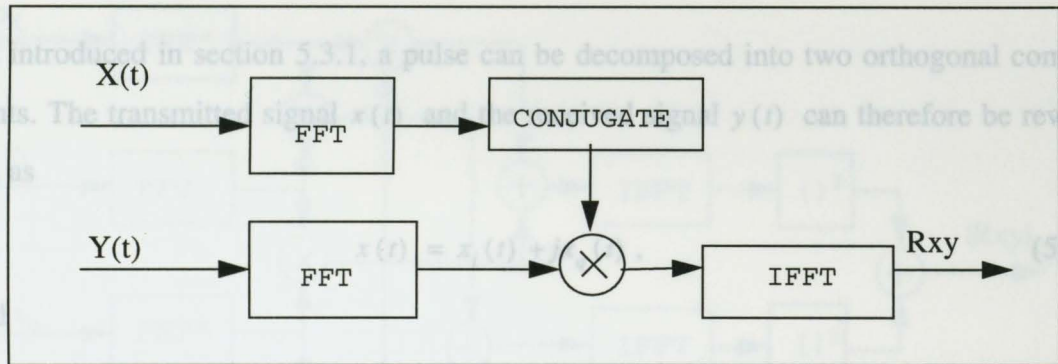


Figure 5.8 Computation diagram for cross-correlation function.

where subscripts i and q represent in-phase and quadrature components of the signal. Let $\tau = rT_1$, where r is the lag number and T_1 is the sample interval for data vectors x_n, y_n . Let $X(f)$ and $Y(f)$ be the Fourier transform of $x(t)$ and $y(t)$. As mentioned above, the computation of the cross correlation can be done via Fourier transforms, that is now defined by

$$\hat{R}_{xy}(rT_1) = \frac{1}{N} \sum_{n=1}^{N-r} x_n y_{n+r} \quad r = 0, 1, \dots, m, \quad (5.13)$$

with m as the maximum lag, and \hat{R}_{xy} the estimate of the true value R_{xy} at lag r , corresponding to the displacement rT_1 . This is the so-called direct computation method.

Another method to compute a cross-correlation function is via fast Fourier transformations, which is shown in Figure 5.8. One can compute the cross-spectral density functions using the fast Fourier transform procedures first and then compute the inverse Fourier transforms of these results. This method may be more efficient in computation than the direct method, depending on the desired maximum lag value m . When $N = 2^p$, where p is an integer, and $m = N$, the speed ratio of the FFT method to the direct method is [5]

$$\text{Speed ratio} = \frac{N^2}{8Np} = \frac{N}{8p}. \quad (5.14)$$

From Eq. (5.18) and Eq. (5.20), \hat{R}_{xy} can be written as

5.3.3 Complex Cross Correlation

As introduced in section 5.3.1, a pulse can be decomposed into two orthogonal components. The transmitted signal $x(t)$ and the received signal $y(t)$ can therefore be rewritten as

$$x(t) = x_i(t) + jx_q(t), \quad (5.15)$$

and

$$y(t) = y_i(t) + jy_q(t), \quad (5.16)$$

where subscripts i and q represent in-phase and quadrature components of the signal. Let $X(f)$ and $Y(f)$ be the Fourier transform of $x(t)$ and $y(t)$. As mentioned above, the computation of the cross correlation can be done via Fourier transform, that is

$$\hat{R}_{xy} = F^{-1} [X^*(f) Y(f)], \quad (5.17)$$

or Now the envelope of the cross-correlation function can be written as

$$|\hat{R}_{xy}| = F^{-1} [G_{xy}], \quad (5.18)$$

where the superscript ' $*$ ' refers to the conjugate value and G_{xy} is defined as the cross spectrum of $x(t)$ and $y(t)$ and can now be written as

$$G_{xy} = (X_i^*(f) - jX_q^*(f)) (Y_i(f) + jY_q(f)). \quad (5.19)$$

G_{xy} can be divided into in-phase part G_{xyi} and quadrature part G_{xyq} as,

$$G_{xy} = G_{xyi} + jG_{xyq} \quad (5.20)$$

where G_{xyi} and jG_{xyq} can be derived from Eq. (5.19) and written as,

$$G_{xyi} = X_i^*(f) Y_i(f) + X_q^*(f) Y_q(f), \quad (5.21)$$

and

$$G_{xyq} = X_i^*(f) Y_q(f) - X_q^*(f) Y_i(f). \quad (5.22)$$

From Eq. (5.18) and Eq. (5.20), \hat{R}_{xy} can be written as

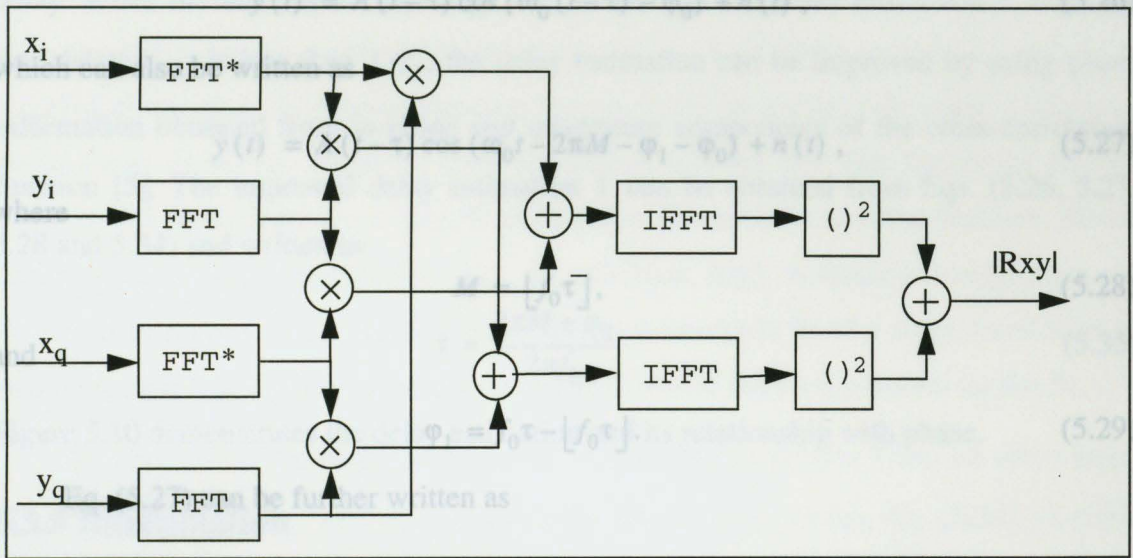


Figure 5.9 Schematic diagram of complex cross correlation.

$$\hat{R}_{xy} = \hat{R}_{xyi} + j\hat{R}_{xyq}. \quad (5.23)$$

Now the envelope of the cross-correlation function can be written as

$$|\hat{R}_{xy}| = \sqrt{\hat{R}_{xyi}^2 + \hat{R}_{xyq}^2}. \quad (5.24)$$

Figure 5.9 illustrates a schematic diagram of this complex cross-correlation method. By locating the peak of the envelope of this cross-correlation function, the time delay can be determined. This delay estimation can be further improved by using the phase information of this complex cross correlation, which will be discussed in the next section.

5.3.4 The Use of Phase Information

Without loss of generalization, a transmitted signal $x(t)$ can be written in the form

$$x(t) = A(t) \cos(\omega_0 t - \varphi_0), \quad (5.25)$$

where $A(t)$ is the envelope of the signal, ω_0 is the carrier frequency of the signal and φ_0 is the initial phase of the signal. After a delay τ , this signal arrives at a receiver with some noise $n(t)$ added during travel. The received signal can be expressed as

delay. When the received signal is $y(t) = A(t - \tau) \cos[\omega_0(t - \tau) - \varphi_0] + n(t)$, (5.26)

which can also be written as

$$y(t) = A(t - \tau) \cos(\omega_0 t - 2\pi M - \varphi_1 - \varphi_0) + n(t), \quad (5.27)$$

where

$$M = \lfloor f_0 \tau \rfloor, \quad (5.28)$$

and

$$\varphi_1 = \frac{2\pi M + \varphi_2}{2\pi f_0} \quad (5.29)$$

Figure 5.10 demonstrates the relationship between φ_1 and τ . (5.29)

Eq. (5.27) can be further written as

$$y(t) = A(t - \tau) \cos(\omega_0 t - \varphi) + n(t), \quad (5.30)$$

where

$$\varphi = \varphi_1 + \varphi_0, \quad (5.31)$$

or alternatively,

$$\varphi_1 = \varphi - \varphi_0. \quad (5.32)$$

From section 5.3.3, φ_1 can be obtained from the angle of a complex cross-correlation function, which can be expressed as

$$\hat{R}_{xy} = |\hat{R}_{xy}| \angle \varphi_1, \quad (5.33)$$

where $|\hat{R}_{xy}|$ has been expressed in Eq. (5.24) and

$$\varphi_1 = \text{atan} \left(\frac{\hat{R}_{xyq}}{\hat{R}_{xyi}} \right). \quad (5.34)$$

The range of φ_1 from Eq. (5.34) is $-\pi - \pi$. Since φ_1 reflects the additional delay after M cycles, it needs to be converted to φ_2 , which has the range of $0 - 2\pi$, depending on the signs of \hat{R}_{xyi} and \hat{R}_{xyq} . Because of the existence of noise, the delay τ estimated by locating the peak of the envelope of a cross-correlation function may not be the true time

delay. When the noise is not too large, i.e. the error of the delay estimation τ from the true delay τ_{true} is less than $1/f_0$, the delay estimation can be improved by using phase information obtained from in-phase and quadrature components of the cross-correlation function [5]. The improved delay estimation $\hat{\tau}$ can be obtained from Eqs. (5.26, 5.27, 5.28 and 5.34) and written as

$$\hat{\tau} = \frac{2\pi M + \varphi_2}{2\pi f_0}. \quad (5.35)$$

Figure 5.10 demonstrates the delay estimation and its relationship with phase.

5.3.5 Interpolation

Because the cross-correlation function is discrete, the resolution of the delay estimated by locating the peak of the cross-correlation function will depend on the sample rate of the signal. A sample rate of 384kHz , which is used in our work, gives a $2.6\mu\text{s}$ resolution. For the location of the cross-correlation peak at around $267\mu\text{s}$ (i.e. 0.4 m path divided by 1500m/s), this sample rate gives a resolution of 1% on the determination of sound speed.

This resolution can be increased by using a quadratic curve to fit the points near the

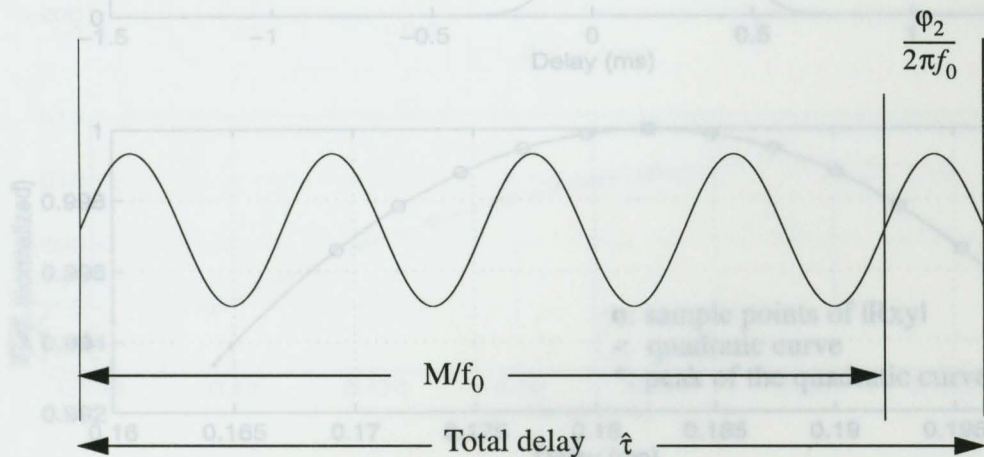


Figure 5.10 Demonstration of delay estimation.

peak of the cross-correlation function. The parameters of the fitted quadratic curve can be computed using the method introduced in section 5.2.3. Then a more accurate peak location of the cross-correlation function can be found by locating the peak of the quadratic curve. However, when the cross-correlation function has high frequency components, it will be difficult to use a quadratic curve to fit a cross-correlation function. So the pulses need to be demodulated first to eliminate high frequency components, as described in section 5.3.1. Figure 5.11 illustrates a quadratic fit of a cross correlation of two pulse envelopes, where eleven points located around the peak are used for the fit.

In order to use the phase information, as described in section 5.3.4, we must determine the values of R_{xyi} and R_{xyq} to calculate the phase ϕ_1 , using Eq. (5.34). A cubic spline interpolation technique is used to fit the sample points of R_{xyi} and R_{xyq} . This is shown in Figure 5.12. Eight points are used in this cubic spline fit. According to the location of the peak of the quadratic curve, which is actually the peak of the cross-correlation

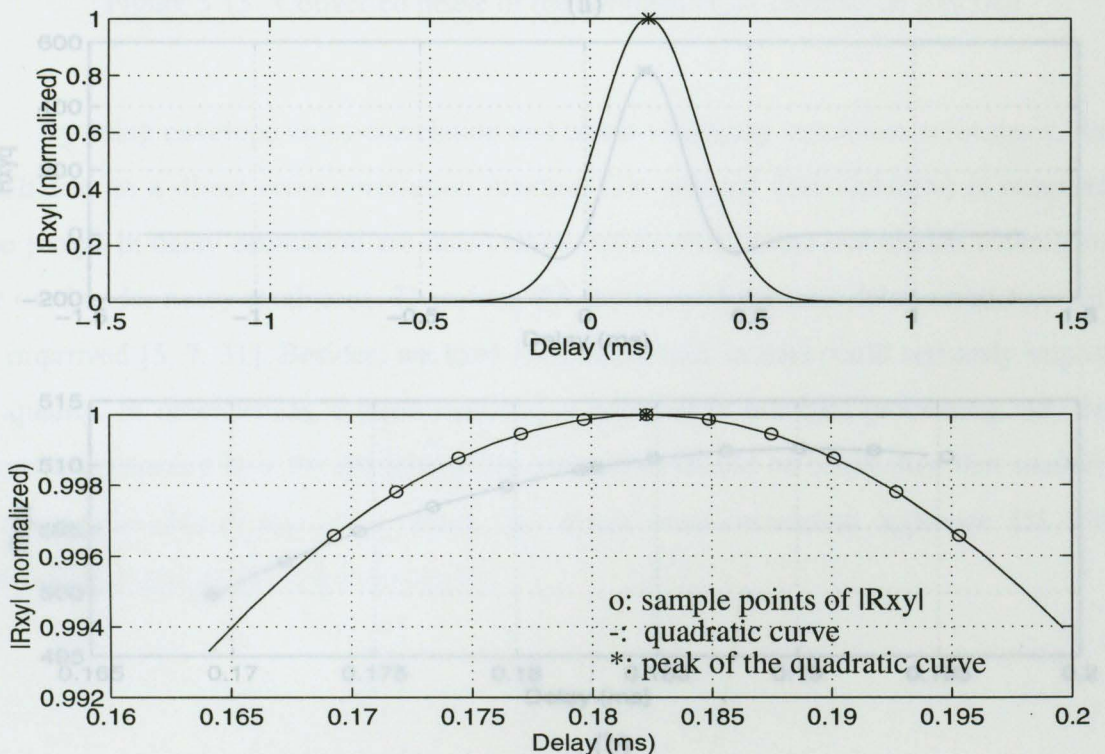
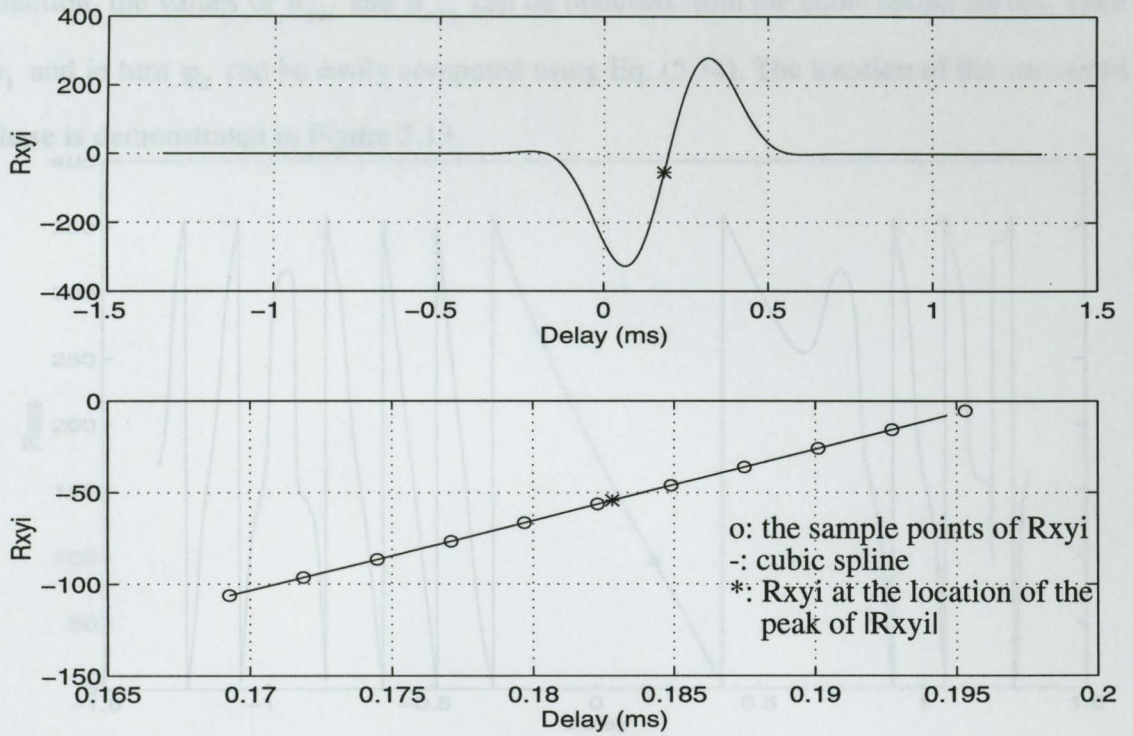
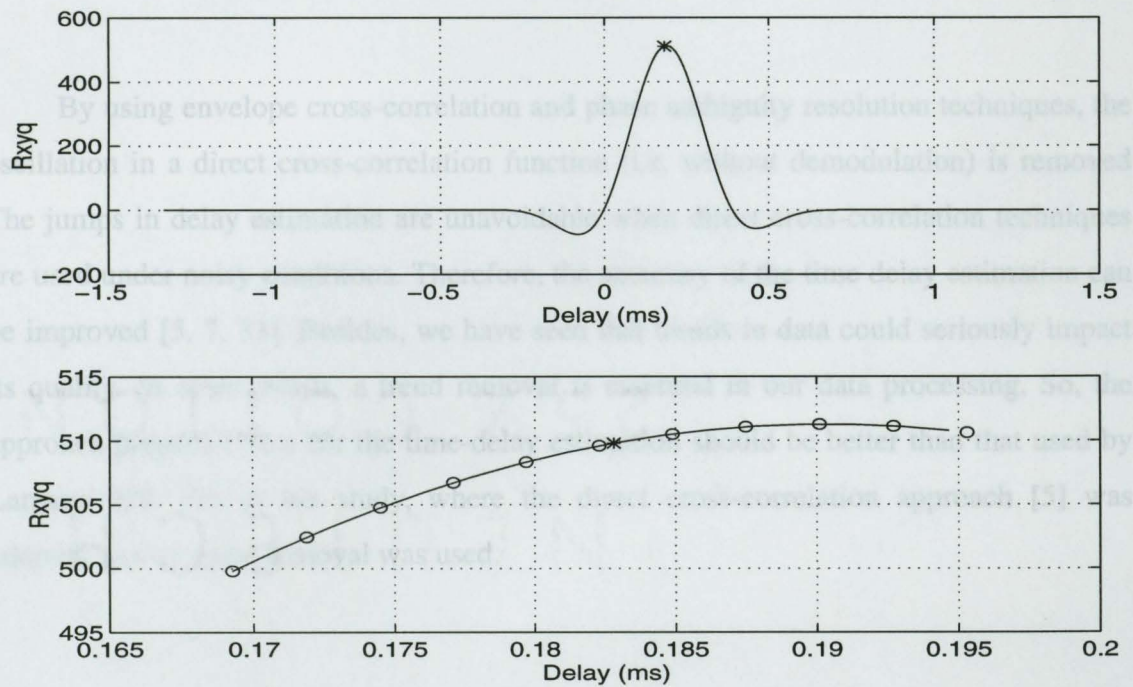


Figure 5.11 Demonstration of quadratic fitting of $|R_{xy}|$.
 cross-correlation function. R_{xyi} and R_{xyq} . Eight points are used for the fit.



(a)



(b)

Figure 5.12 Demonstration of cubic spline fitting for inphase and quadrature cross-correlation function, R_{xyi} and R_{xyq} . Eight points are used for the fit.

function, the values of R_{xyi} and R_{xyq} can be obtained from the cubic spline curves. Then φ_1 and in turn φ_2 can be easily computed using Eq. (5.34). The location of the converted phase is demonstrated in Figure 5.13.

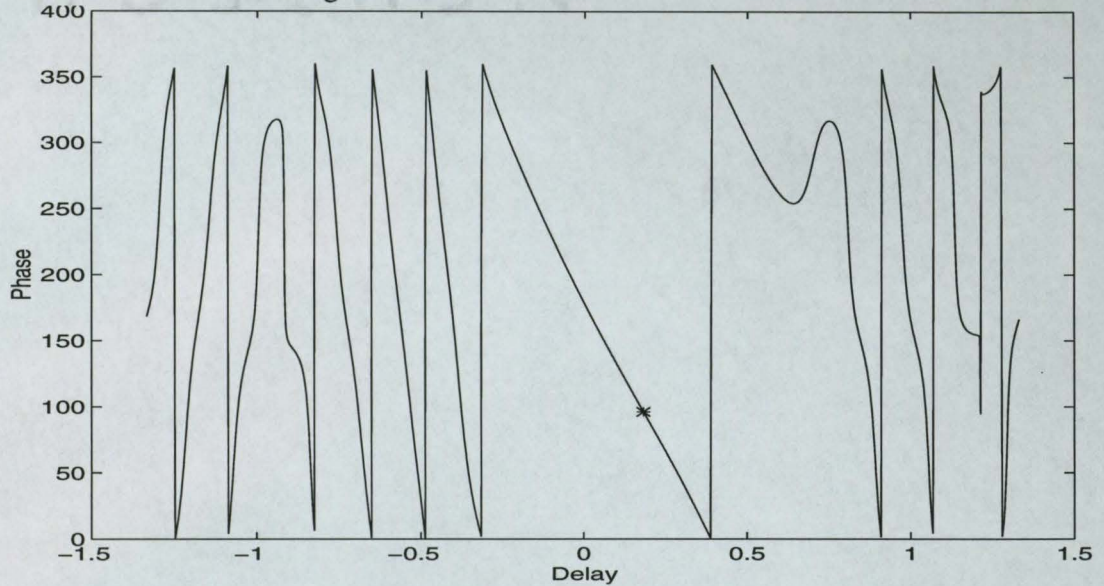


Figure 5.13 Converted phase of the complex cross-correlation function.

By using envelope cross-correlation and phase ambiguity resolution techniques, the oscillation in a direct cross-correlation function (i.e. without demodulation) is removed. The jumps in delay estimation are unavoidable when direct cross-correlation techniques are used under noisy conditions. Therefore, the accuracy of the time delay estimation can be improved [5, 7, 31]. Besides, we have seen that trends in data could seriously impact its quality. In other words, a trend removal is essential in our data processing. So, the approach proposed here for the time-delay estimation should be better than that used by Lamarre [20, 21] in his study, where the direct cross-correlation approach [5] was adopted and no trend removal was used.

5.4 Inference of Bubble Size Distribution

2. Initialize α and β in the model.

Sound speed in bubbly water can be determined by the sound travelling time (or time delay) and the distance between the transmitter and receiver. From the estimated sound speed and the effect of bubbles on the sound speed as introduced in Chapter 2, one can estimate the bubble size distribution by using optimization techniques. One commonly used optimization technique is least-square estimation. First we need to set a bubble distribution model $n(a) da$ and then use this model to compute the sound speed $C_c(f)$, according to the equations introduced in Chapter 2. By minimizing the difference between the estimated sound speed $C_e(f)$ and the computed sound speed $C_c(f)$ from the model, one can optimize the parameters in the model so that the bubble distribution can be decided. The model used in this work is

$$n(a) da = 10^\alpha a^\beta, \quad (5.36)$$

where a in μm is the bubble radius, $n(a) da$ is the number of bubbles per cubic meter with radius increment $a \sim a + da$. α and β [30] are the parameters to be optimized. Note that Eq. (5.36) can be only applied to a certain range of bubble radii a . According to previous reports (refer to Table 1.1), for different ranges of bubble radii, the slopes of bubble size distributions are different. Therefore, more terms may need to be add into Eq. (5.36). For simplicity, we use Eq. (5.36) as our model. So the objective function to be optimized can be written as

$$F(\alpha, \beta) = \sum_{j=1}^m (C_e(\alpha, \beta, f_j) - C_c(\alpha, \beta, f_j))^2, \quad (5.37)$$

where m is the total number of carrier frequencies.

The procedure for bubble size distribution calculations can be summarized as follows:

1. Estimate sound speed $C_e(f)$ in bubbly water;

2. Choose bubble size distribution model, i.e. Eq. (5.36);
3. Initialize α and β in the model;
4. Computer sound speed $C_c(f)$ using equations introduced in Chapter 2;
5. Compute the objective function F in Eq. (5.37);
6. Set new α and β according to chosen optimization technique;
7. Repeat step 4, 5 and 6 to minimize the objective function.

In our work, the simplex method [22] is chosen to optimize α and β .

Bubbly Water

In chapters 2 and 3, the effects of bubbles on sound propagation in water have been discussed. The discussion was based on the steady state of bubble resonance. Because of the damping property of a bubble, there is a period of transient time needed for a bubble to be excited into a fully resonant state by an incident sound wave. When an acoustic pulse is short and comparable to the transient time, the effect of this transient time needs to be considered. This transient process was discussed by Akulichev and Bulanov [1]. However, their work was limited to analysis of the effect of short pulse on back scatter target strength, whereas the interest here is in the effect on sound speed and attenuation. This chapter presents some new results, i.e. the derivation of the equations for the propagation of short acoustic pulses in bubbly water.

6.1 Preliminary

Medwin [27] discussed the distinctive resonance characteristics of a gas bubble in water. He also gave the derivation of sound speed in bubbly water under the steady-state condition.

If a bubble is insonified at or near its natural frequency, it will be excited to resonate. Two basic mechanical requisites are needed to make a bubble resonate. One is the

stiffness and the other is the inertia. The stiffness is a property of the gas enclosed in a bubble, which acts like a spring when the bubble is disturbed from its equilibrium radius. The inertia is due to the mass of water that surrounds the bubble and oscillates with it.

Chapter 6

Propagation of Short Acoustic Pulses in Bubbly Water

$$\frac{dp}{dV} = -\frac{\gamma P_0}{V}, \quad (6.1)$$

where P_0 is the ambient pressure $P_0 = p_i$, and $dV = 4\pi a^2 da$.

In chapters 2 and 3, the effects of bubbles on sound propagation in water have been discussed. The discussion was based on the steady state of bubble resonance. Because of the damping property of a bubble, there is a period of transient time needed for a bubble to be excited into a fully resonant state by an incident sound wave. When an acoustic pulse is short and comparable to the transient time, the effect of this transient time needs to be considered. This transient process was discussed by Akulichev and Bulanov [1]. However, their work was limited to analysis of the effect of short pulse on back scatter target strength, whereas the interest here is in the effect on sound speed and attenuation. This chapter presents some new results, i.e. the derivation of the equations for the propagation of short acoustic pulses in bubbly water.

6.1 Preliminary

$$s_A = 12\pi\gamma P_0 a, \quad (6.3)$$

where the subscript A refers to adiabatic condition. For small bubbles, with radii less than $1\mu\text{m}$, the surface tension becomes important, and the compressions and expansions of the gas in the bubble become isothermal instead of adiabatic [37]. When all these are being considered, P_0 is replaced by an average interior pressure including surface tension.

If a bubble is insonified at or near its natural frequency, it will be excited to resonance. Two basic mechanical requisites are needed to make a bubble resonate. One is the

stiffness and the other is the inertia. The stiffness is a property of the gas enclosed in a bubble, which acts like a spring when the bubble is disturbed from its equilibrium radius. The inertia is due to the mass of water that surrounds the bubble and oscillates with it.

The stiffness restoring force can be derived from the adiabatic gas relation, which can be expressed as $pV^\gamma = \text{constant}$, where p is the instantaneous total pressure within the bubble volume $V = (4/3)\pi a^3$, and $\gamma = C_p/C_v$ is the ratio of the two specific heats of the enclosed gases in a bubble. Differentiating yields,

$$\frac{dp}{dV} = -\frac{\gamma P_0}{V}, \quad (6.1)$$

where P_0 is the ambient pressure $P_0 \gg p_i$ and $dV = 4\pi a^2 da$.

Since the change of pressure, volume and radius are very small, the differential variables can be replaced by their incremental variables. Letting $p_i = p - P_0$ represent the instantaneous incremental pressure ($P_0 \gg p_i$) and $\Delta V = 4\pi a^2 \Delta a$, and rewriting the displacement Δa of a bubble radius as ζ , the stiffness restoring force can be expressed in the form of Hooke's Law, which is

$$F_r = 4\pi a^2 p_i = -(12\pi a \gamma P_0) \zeta. \quad (6.2)$$

Letting s_A represent the quantity in parentheses, which is called the stiffness constant, and we have

$$F_r|_{R=a} = -p_i s_A = 12\pi \gamma P_0 a, \quad (6.3)$$

where the subscript A refers to adiabatic condition. For small bubbles, with radii less than $1\mu m$, the surface tension becomes important, and the compressions and expansions of the gas in the bubble become isothermal instead of adiabatic [37]. When all these are being considered, P_0 is replaced by an average interior pressure including surface tension βP_0 , and γ is replaced by the effective ratio of the specific heats in the presence of

thermal conductivity, γb . Now with s_A replaced by s , we have
 damping constant, that is [27],

$$s = 12\pi a\beta P_0\gamma b. \quad (6.4)$$

The inertial force acting over the bubble surface can be determined by calculating the pressure of the re-radiated sound. Apparently, a major part of the oscillating mass is the liquid adjacent to the bubble rather than the mass of the gas inside the bubble. The complex pressure wave scattered by the resonant bubble is given by

$$p_s = P_s (R_1/R) \exp [i(\omega t - kR)], \quad (6.5)$$

where P_s is the rms scattered pressure when R is equal the reference range R_1 ($=1\text{m}$).

The relation between the fluid velocity v and the pressure gradient $\partial p_s/\partial R$ is given [37] by

$$\rho \frac{\partial v}{\partial t} = -\frac{\partial p_s}{\partial R} \quad (6.6)$$

where ρ is the water density, and

$$\frac{\partial p_s}{\partial R} = \left(-\frac{P_s R_1}{R^2} \right) (1 + ikR) \exp [i(\omega t - kR)]. \quad (6.7)$$

With $ka \ll 1$, we evaluate Eq. (6.7) at $R = a$ to obtain

$$\rho |\ddot{\zeta}| = p_s/a. \quad (6.8)$$

Therefore, the inertial force at the surface is

$$F_m|_{R=a} = -p_s|_{R=a} (4\pi a^2) = -4\pi a^3 \rho \ddot{\zeta}|_{R=a}. \quad (6.9)$$

Eq. (6.9) is identical to Newton's First Law by defining an effective mass of water

as

$$m = 4\pi a^3 \rho, \quad (6.10)$$

which rides with the bubble.

When a bubble is driven by a plane wave at $ka \ll 1$, its motion is described by the

lumped constant approach with mechanical resistance parameter R_M , where δ is the damping constant, that is [27],

$$R_M = m\delta\omega. \quad (6.11)$$

According to Newton's Second Law, we have,

$$m\ddot{\zeta} + R_M\dot{\zeta} + s\zeta = 4\pi a^2 \sqrt{2} P_p \exp(i\omega t), \quad (6.12)$$

and by solving Eq. (6.12), we can obtain the steady-state radial displacement

$$\zeta_1 = \frac{-i4\pi a^2 (\sqrt{2} P_p / \omega) \exp(i\omega t)}{R_M + i(\omega m - s/\omega)}, \quad (6.13)$$

where P_p is the rms pressure of the incident plane wave whose angular frequency is ω .

6.2 The Transient Process

Eq. (6.13) is a steady-state solution of Eq. (6.12) with the assumption that an incident pulse length is long enough to ignore the transient process. However, when a pulse length is not that long, a transient period of natural oscillation must be considered. The natural oscillation component of the solution of Eq. (6.12) can be obtained by solving the characteristic equation

$$D^2 + \frac{R_M}{m}D + \frac{s}{m} = 0. \quad (6.14)$$

The roots of Eq. (6.14) are

$$D_{1,2} = -\left(\frac{R_M}{2m}\right) \pm \sqrt{\left(\frac{R_M}{2m}\right)^2 - \left(\frac{s}{m}\right)}, \quad (6.15)$$

which can also be written as,

$$D_{1,2} = -\frac{\delta\omega}{2} \pm \sqrt{\left(\frac{\delta\omega}{2}\right)^2 - \omega_r^2}, \quad (6.16)$$

where δ is the damping constant of a bubble and $\omega_r = \sqrt{s/m}$ is the resonant frequency of a bubble. The damping constant, δ , is a function of bubble radius and incident fre-

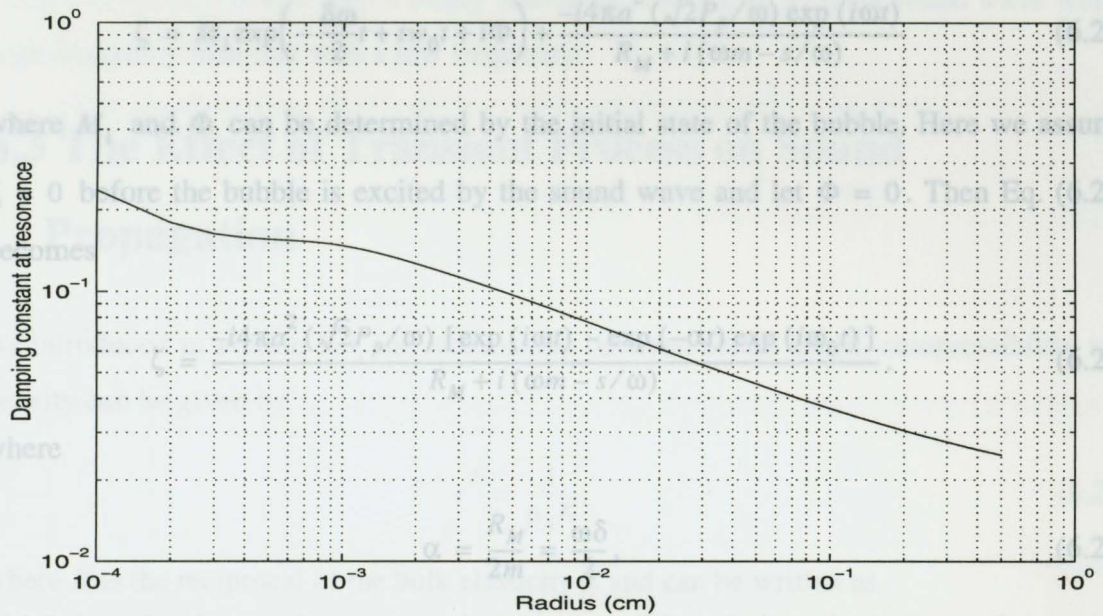


Figure 6.1 Damping constant at resonance versus bubble radius when the frequency of incident sound wave is equal to bubble resonant frequency.

frequency. The relationship between damping constant and bubble radius is plotted in Figure 6.1 where the frequency of an incident sound wave, ω , is equal to the bubble resonant frequency, ω_r . From Figure 6.1, we know that the damping constant $\delta < 0.2$. Thus,

$\left(\frac{\delta\omega}{2}\right)^2 < \omega_r^2$. So, the natural oscillation component of the solution of Eq. (6.12) is

$$\zeta_n = M_1 \exp\left(-\frac{\delta\omega}{2}t + iw_0t + i\Phi\right), \quad (6.17)$$

where Φ is the initial phase and magnitude of the natural oscillation component, and

$$\omega_o = \sqrt{\omega_r^2 - \left(\frac{\delta\omega}{2}\right)^2} = \text{ringing frequency in rad/s.} \quad (6.18)$$

When the frequency of an incident sound wave, ω , is equal to the bubble resonant frequency, ω_r , Eq. (6.18) can be written as

$$\omega_o = \omega_r \sqrt{1 - \left(\frac{\delta}{2}\right)^2} \approx \omega_r. \quad (6.19)$$

Combining Eq. (6.13) and (6.17), the solution of Eq. (6.12) is

$$\zeta = M_1 \exp\left(-\frac{\delta\omega}{2}t + i\omega_0 t + i\Phi\right) + \frac{-i4\pi a^2 (\sqrt{2}P_p/\omega) \exp(i\omega t)}{R_M + i(\omega m - s/\omega)} \quad (6.20)$$

where M_1 and Φ can be determined by the initial state of the bubble. Here we assume $\zeta = 0$ before the bubble is excited by the sound wave and let $\Phi = 0$. Then Eq. (6.20) becomes

$$\zeta = \frac{-i4\pi a^2 (\sqrt{2}P_p/\omega) [\exp(i\omega t) - \exp(-\alpha t) \exp(i\omega_0 t)]}{R_M + i(\omega m - s/\omega)} \quad (6.21)$$

where

$$\alpha = \frac{R_M}{2m} = \frac{\omega\delta}{2}, \quad (6.22)$$

which is defined as a ringing damping constant. The relationship between the ringing damping constant and the frequency of an incident sound wave, which is equal to bubble resonant frequency, is plotted in Figure 6.2. From the figure we can see the ringing damping factor increases when the incident frequency increases, which means less time is

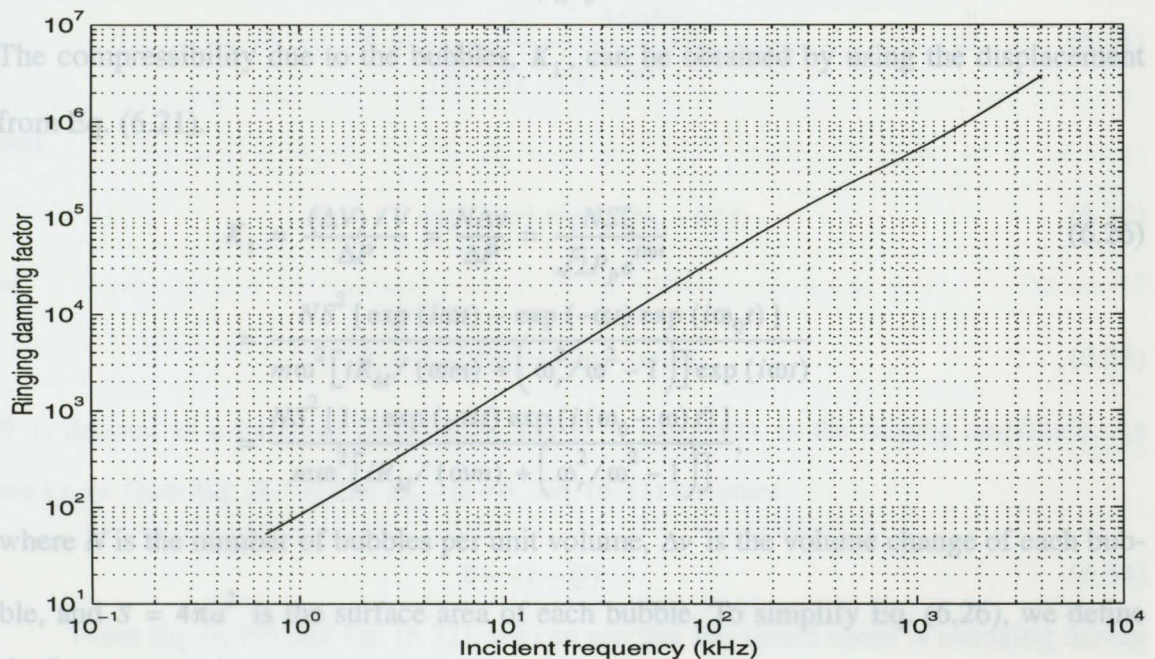


Figure 6.2 Ringing damping constant versus the frequency of an incident sound wave.

needed to excite a bubble into a steady resonance state for an incident sound wave with a high frequency than that with a low frequency.

6.3 The Effect of Transient Process on Sound

Propagation

As introduced in section 2.3, the relationship between sound speed, compressibility and density can be given by Eq. (6.23), a sound speed in the bubbly medium can be written in the form

$$c^2 = \frac{1}{\rho_A K}, \tag{6.23}$$

where K is the reciprocal of the bulk elasticity E and can be written as

$$K = K_0 + K_1, \tag{6.24}$$

where

$$K_0 = \frac{1}{\rho_A c_0^2}. \tag{6.25}$$

The compressibility due to the bubbles, K_1 , can be obtained by using the displacement from Eq. (6.21).

$$K_1 = \frac{(\Delta V) / V}{\Delta P} = \frac{N \Delta v}{\Delta P} = \frac{NS \zeta}{\sqrt{2} P_p e^{i\omega t}} \tag{6.26}$$

$$= \frac{NS^2 [\exp(i\omega t) - \exp(-\alpha t) \exp(i\omega_0 t)]}{m\omega^2 [iR_M / (\omega m) + (\omega_r^2 / \omega^2 - 1)] \exp(i\omega t)} \tag{6.33}$$

$$= \frac{NS^2 [1 - \exp(-\alpha t) \exp(i(\omega_0 - \omega)t)]}{m\omega^2 [iR_M / (\omega m) + (\omega_r^2 / \omega^2 - 1)]}$$

where N is the number of bubbles per unit volume, Δv is the volume change of each bubble, and $S = 4\pi a^2$ is the surface area of each bubble. To simplify Eq. (6.26), we define the frequency ratio

From Eq. (6.29) and Eq. (6.32), we can see that the sound speed is changing during the transient period. So, when a very short acoustic pulse passes through bubbly water, the pulse signal will be distorted. Also note that from Eq. (6.22) and Eq. (6.32), the ring-

$$Y \equiv \frac{f_r}{f} = \frac{\omega_r}{\omega} \quad (6.27)$$

Now, by using Eqs. (6.11), (6.21), (6.22), (6.26) and (6.27), we have

$$K_1 = \frac{4\pi a N [1 - \exp(-\alpha t) \exp(i(\omega_0 - \omega)t)] [Y^2 - 1 - i\delta]}{\rho_A \omega^2 [\delta^2 + (Y^2 - 1)^2]}, \quad (6.28)$$

where ρ_A is the water density.

Now considering Eq. (6.23), a sound speed in the bubbly medium can be written in the form

$$c = \left(\frac{1}{\rho_A K} \right)^{1/2} = \frac{c_0}{(1 + A\theta - iB\theta)^{1/2}}, \quad (6.29)$$

where

$$A = \frac{Y^2 - 1}{(Y^2 - 1)^2 + \delta^2} \frac{4\pi a N c_0^2}{\omega^2}, \quad (6.30)$$

$$B = \frac{\delta}{(Y^2 - 1)^2 + \delta^2} \frac{4\pi a N c_0^2}{\omega^2}, \quad (6.31)$$

and

$$\theta = 1 - \exp(-\alpha t) \exp(i(\omega_0 - \omega)t) \quad (6.32)$$

or Since A and B are extremely small in the ambient ocean and $0 \leq \theta < 1$, the sound

$$\theta = 1 - Q \exp(i(\omega_0 - \omega)t). \quad (6.33)$$

θ is defined as a transient factor here, and $Q = \exp(-\alpha t)$ is the ringing amplitude. As we know from Eq. (6.19) that $\omega_0 - \omega \approx 0$, Eq. (6.33) becomes

$$\theta \approx (1 - Q) \quad (6.34)$$

From Eq. (6.29) and Eq. (6.32), we can see that the sound speed is changing during the transient period. So, when a very short acoustic pulse passes through bubbly water, the pulse signal will be distorted. Also note that from Eq. (6.22) and Eq. (6.32), the ring-

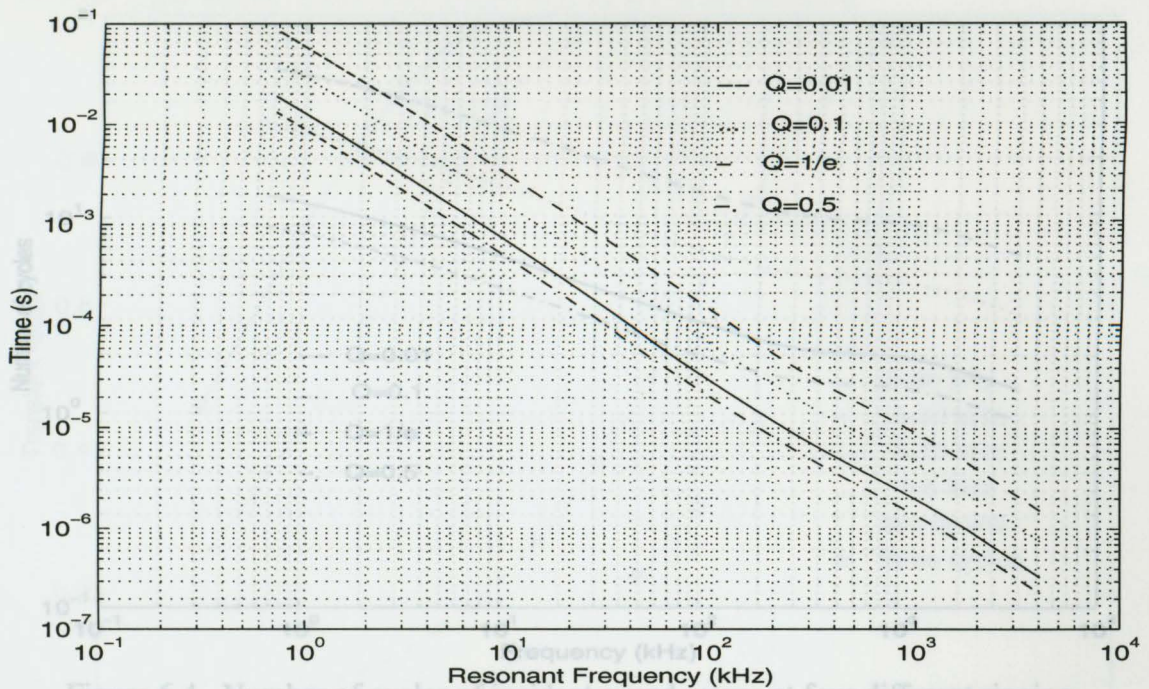


Figure 6.3 Time needed to reach four different ringing amplitudes, Q , at different frequencies.

ing damping factor α of the natural oscillation is proportional to the damping constant δ and the frequency of the incident sound wave, which means the transient time is frequency dependent. The time needed to reach each of four different ringing amplitudes is shown in Figure 6.3. Figure 6.4 shows the time in the number of cycles of an incident sound wave.

Since A and B are extremely small in the ambient ocean and $0 \leq \theta < 1$, the sound speed in bubbly water can be rewritten as

$$c \approx \frac{c_0}{1 + (A/2)\theta - i(B/2)\theta} \quad (6.35)$$

The complex propagation constant, k , can now be expressed as

$$k = \frac{\omega}{c} = \frac{\omega(1 + (A/2)\theta - i(B/2)\theta)}{c_0} \quad (6.36)$$

Rewriting Eq. (6.36) into real and imaginary parts, we have,

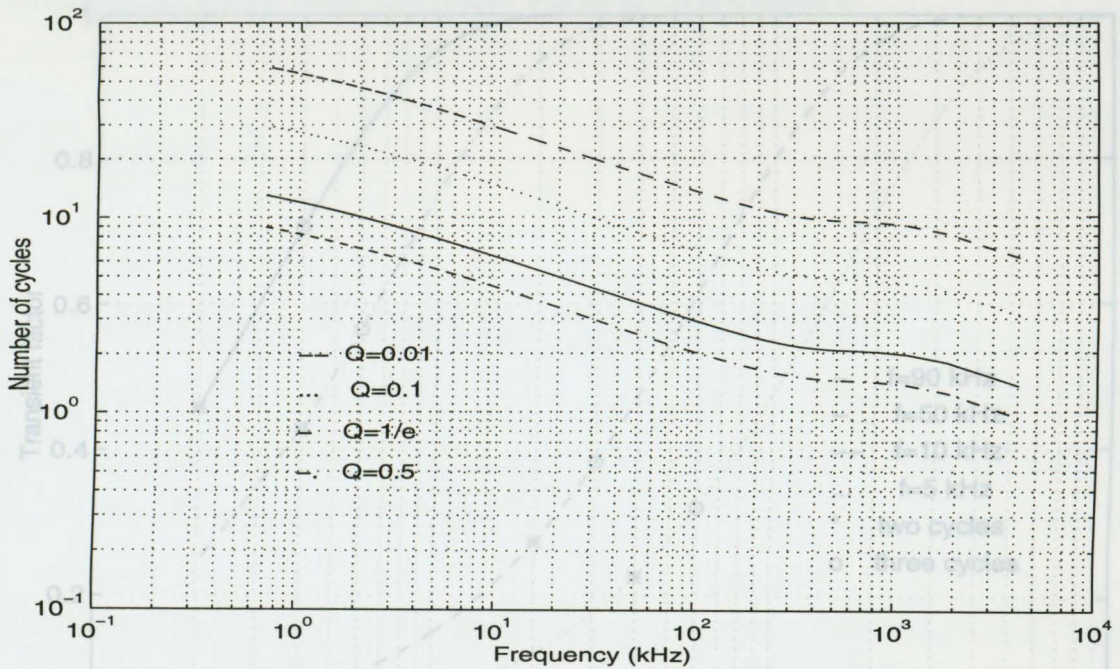


Figure 6.4 Number of cycles of incident sound waves at four different ringing amplitudes, Q .

Figure 6.5 $k_{im} = k_0 \frac{B}{2} \theta;$ of transient process (6.37)

$$k_{re} = k_0 \left(1 + \frac{A}{2} \theta \right). \tag{6.38}$$

The imaginary part k_{im} of the complex propagation constant represents the attenuation of the sound wave passing through bubbly water. The real part k_{re} is the wave number. This implies that it takes less time to change its state. In other words, a small bubble

takes less time to be excited into resonance than a large bubbles does. From Eq. (6.32), we can see that $\theta = 0$ when $t = 0$ and $\theta = 1$ when $t \rightarrow \infty$. So, we can see from Eq. (6.37) that the attenuation increases with θ , which implies that it increases with time. To show transient processes more explicitly, the transient factor, θ , is plotted versus time at four different frequencies in Figure 6.5. From the figure we can see that the transient process at high frequency is shorter than that at low frequency. On the other hand, for the same number of cycles of incident sound waves, a sound wave with higher frequency has larger transient factor than that with lower frequency. This phenom-

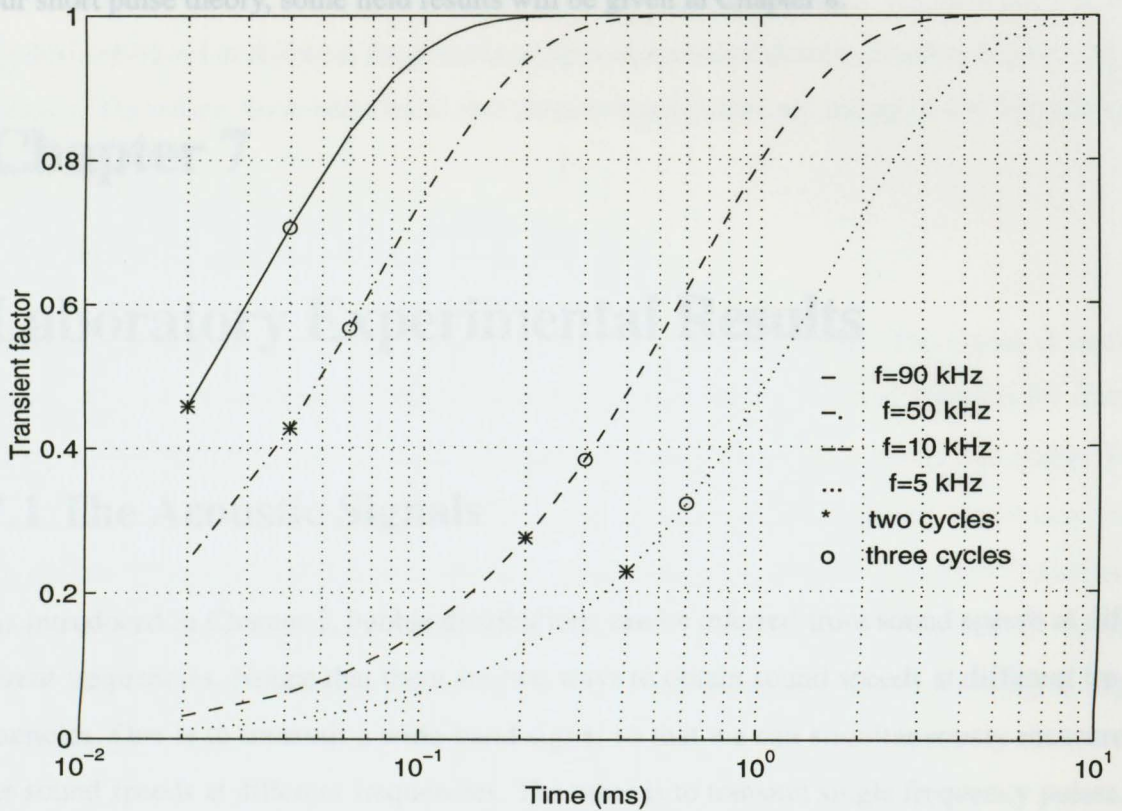


Figure 6.5 Demonstration of transient process

enon can be interpreted in physics as: bubbles with different sizes need different amounts of sound energy to be excited into resonance. A small bubble, which relates to higher resonance frequency, needs less energy to be excited into resonance than a large bubble. Also, from Figure 6.1, we can see that a small bubble has a larger damping constant which implies that it takes less time to change its state. In other words, a small bubble takes less time to be excited into resonance than a large bubbles does.

From Eqs. (6.32, 6.37, 6.38) it is apparent that the propagation of a short acoustical pulse is less effected than that of a long one in the same bubbly water. Thus, with the same attenuation or sound speed change, the steady state equation will predict fewer bubbles than the transient process does, which leads us to our conclusion that the number of bubbles will be under-estimated, when the steady-state equations of sound speed in bubbly water, Eqs. (2.27, 2.29, 2.30), are applied to a very short acoustical pulse. To verify

our short pulse theory, some field results will be given in Chapter 8.

Chapter 7

7.1.1 Multi-frequency Pulse

Laboratory Experimental Results

7.1 The Acoustic Signals

As introduced in Chapter 2, bubble distributions can be inferred from sound speeds at different frequencies. Notice that there are two ways to obtain sound speeds at different frequencies. One is to transmit a wide-band signal so that we can simultaneously measure the sound speeds at different frequencies. The other is to transmit single frequency pulses, i.e. narrow-band signals, one after another. For the second method, the transmitting interval must be short enough so that we can assume that bubble clouds would not be changed during the period when a set of pulses with different frequencies are transmitted. The advantage of using the second method over the first one is that we can obtain larger power at each frequency, i.e. better signal-to-noise ratio, so that the instrument can

The bandwidth of a composite signal is determined by its pulse length. In this case, the pulse length is two cycles of the wave length of the lowest frequency pulse. The bandwidth for each single frequency pulse is about 0.25%.

Figure 7.1. Multi-frequency pulse with the same initial phases

work under worse ambient conditions. However, unlike the first method, the sound speeds measured at different frequencies may not represent identical bubble density conditions. Therefore, both wide-band and narrow-band pulses are tested in our laboratory

Chapter 7

7.1.1 Multi-frequency Pulse

Laboratory Experimental Results

In our study, a multi-frequency pulse is used as a wide band signal. The signal is composed of a set of superposed single frequency pulses, which contains frequencies from 6kHz to 100kHz . So, a multi-frequency pulse can also be called a composite pulse. To

7.1 The Acoustic Signals

As introduced in Chapter 2, bubble distributions can be inferred from sound speeds at different frequencies. Notice that there are two ways to obtain sound speeds at different frequencies. One is to transmit a wide-band signal so that we can simultaneously measure the sound speeds at different frequencies. The other is to transmit single frequency pulses, i.e. narrow-band signals, one after another. For the second method, the transmitting interval must be short enough so that we can assume that bubble clouds would not be changed during the period when a set of pulses with different frequencies are transmitted. The advantage of using the second method over the first one is that we can obtain larger power at each frequency, i.e. better signal-to-noise ratio, so that the instrument can

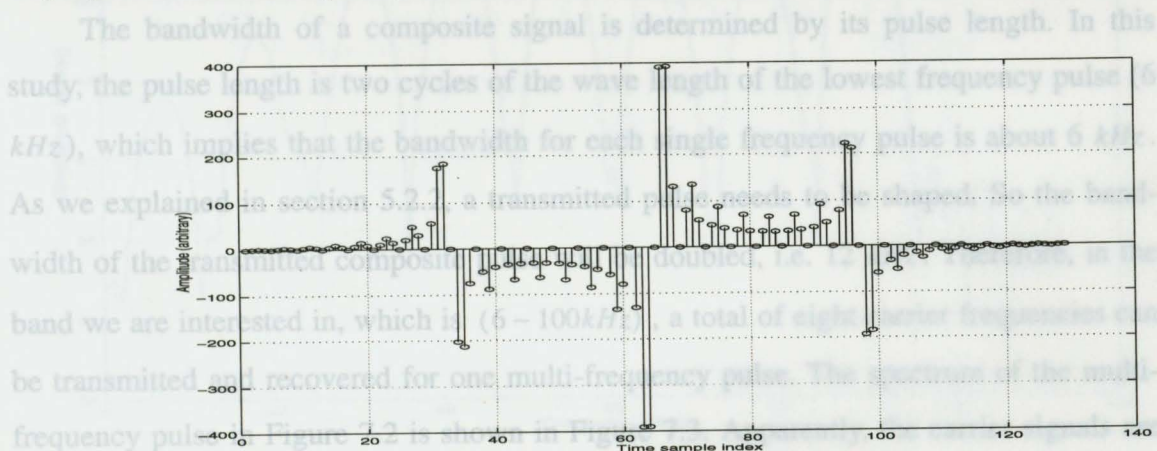


Figure 7.1 Multi-frequency pulse with the same initial phases

work under worse ambient conditions. However, unlike the first method, the sound speeds measured at different frequencies may not represent identical bubble density conditions. Therefore, both wide-band and narrow-band pulses are tested in our laboratory experiments.

7.1.1 Multi-frequency Pulse

In our study, a multi-frequency pulse is used as a wide band signal. The signal is composed of a set of superposed single frequency pulses, which contains frequencies from 6kHz to 100kHz . So, a multi-frequency pulse can also be called a composite pulse. To make the transmission smooth, the initial phase of each single frequency pulse must be optimized. Figure 7.1 shows the peaks in a composite pulse without any phase optimization. The improved composite signal after using phase optimization is shown in Figure 7.2. Table 7.1 gives the initial phases of the two multi-frequency pulses we used in our experiments.

Pulse 1	Frequency (kHz)	10	22	34	46	58	70	82	94
	Phase (rad)	-0.0030	5.8154	-0.0021	5.7299	-0.0006	2.5901	-0.0008	3.4651
Pulse2	Frequency (kHz)	6	18	30	42	54	66	78	90
	Phase (rad)	0.0621	0.8217	0.1175	4.1083	0.1823	1.5465	-0.0108	1.2414

Table 7.1. The optimized initial phases of multi-frequency pulses

The bandwidth of a composite signal is determined by its pulse length. In this study, the pulse length is two cycles of the wave length of the lowest frequency pulse (6kHz), which implies that the bandwidth for each single frequency pulse is about 6kHz . As we explained in section 5.2.2, a transmitted pulse needs to be shaped. So the bandwidth of the transmitted composite pulse will be doubled, i.e. 12kHz . Therefore, in the band we are interested in, which is ($6 \sim 100\text{kHz}$), a total of eight carrier frequencies can be transmitted and recovered for one multi-frequency pulse. The spectrum of the multi-frequency pulse in Figure 7.2 is shown in Figure 7.3. Apparently, the carrier signals are well separated in the spectrum, which makes it possible to filter out each carrier signal

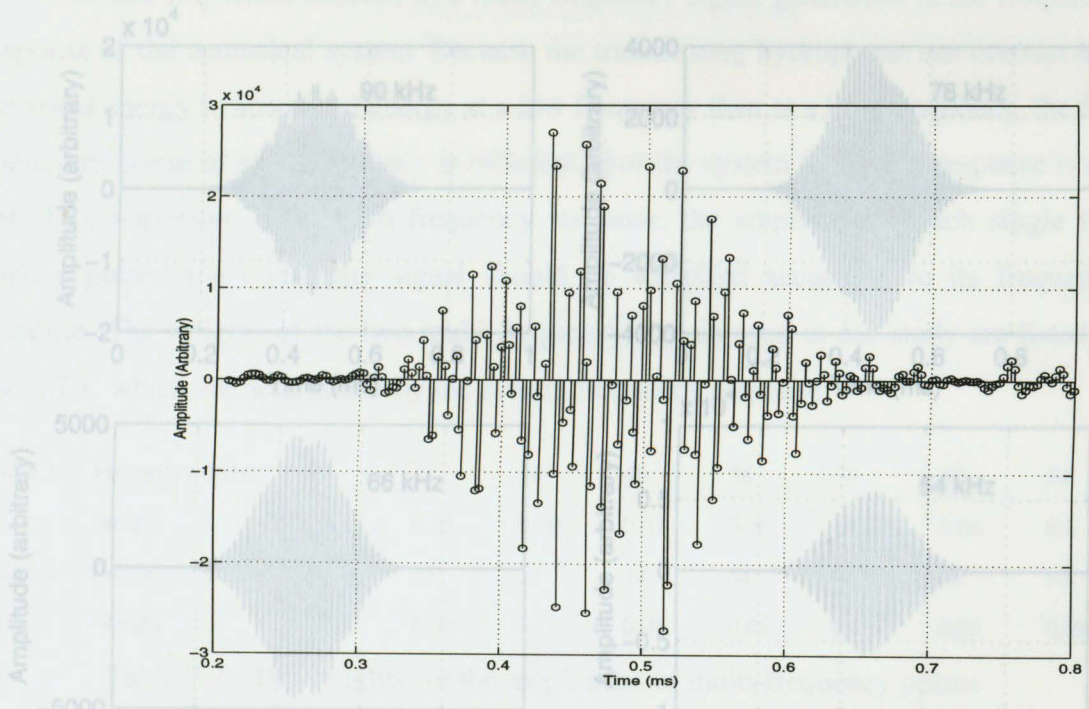


Figure 7.2 Received multi-frequency pulse with optimized phase.

from the others. Figure 7.4 shows the filtered carrier signals by using windows in the frequency domain. The bandwidth of the window is 12kHz .

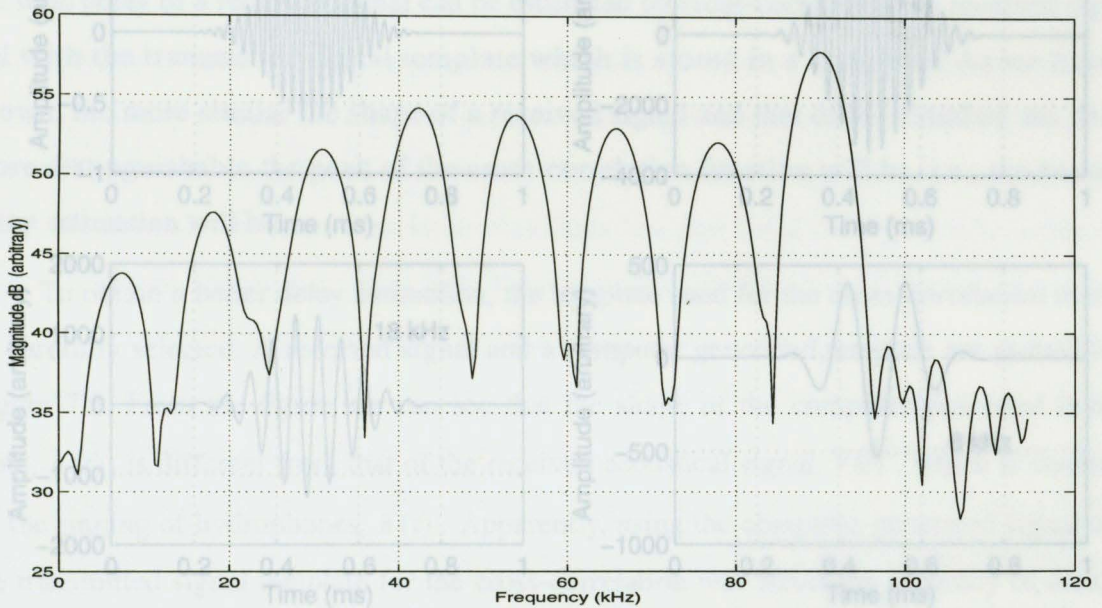


Figure 7.3 Energy spectrum of a multi-frequency pulse.

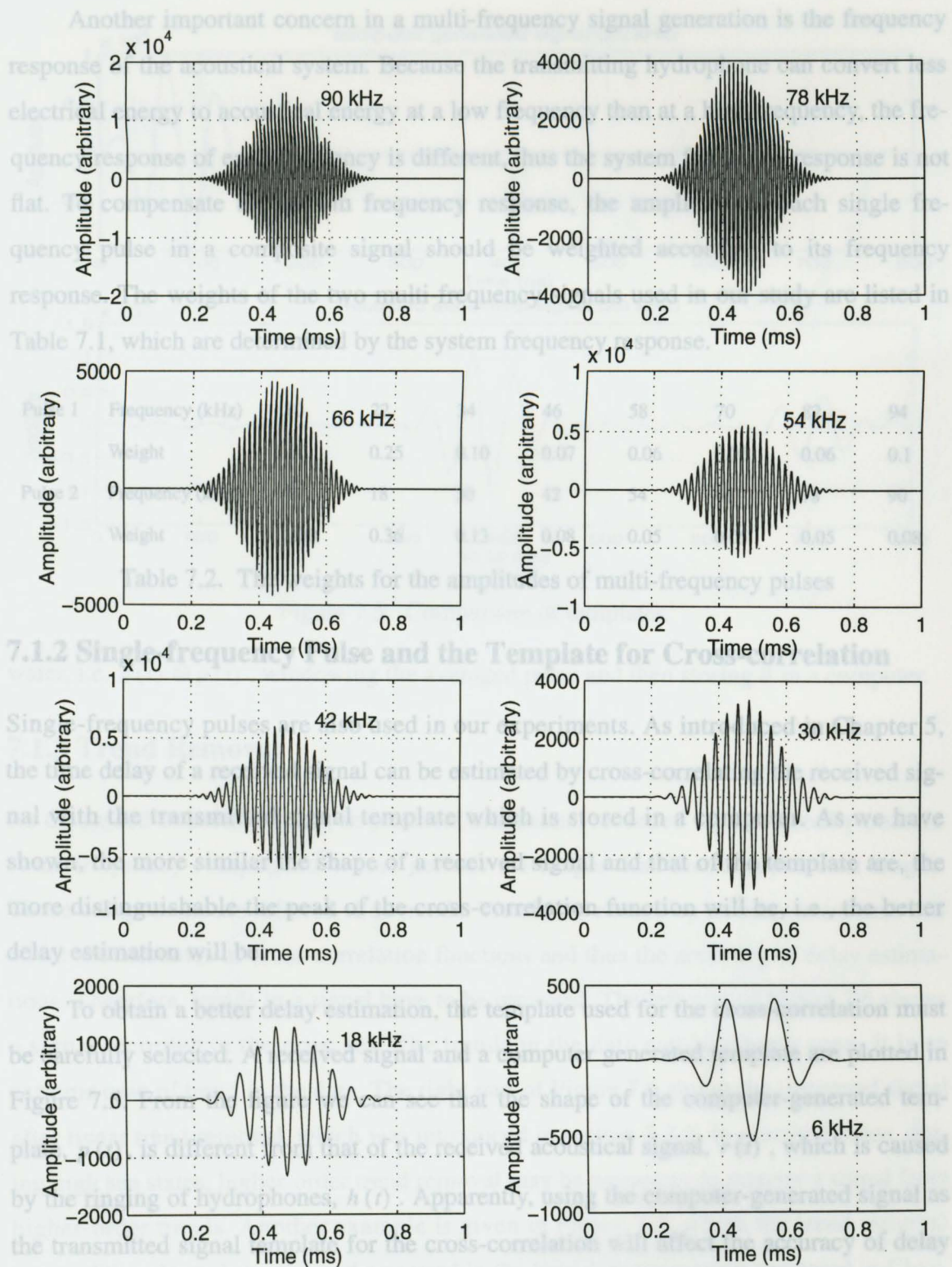


Figure 7.4 Carrier signals filtered from multi-frequency pulse.

Another important concern in a multi-frequency signal generation is the frequency response of the acoustical system. Because the transmitting hydrophone can convert less electrical energy to acoustical energy at a low frequency than at a high frequency, the frequency response of each frequency is different, thus the system frequency response is not flat. To compensate the system frequency response, the amplitude of each single frequency pulse in a composite signal should be weighted according to its frequency response. The weights of the two multi-frequency signals used in our study are listed in Table 7.1, which are determined by the system frequency response.

Pulse 1	Frequency (kHz)	10	22	34	46	58	70	82	94
	Weight	1.00	0.25	0.10	0.07	0.06	0.05	0.06	0.1
Pulse 2	Frequency (kHz)	6	18	30	42	54	66	78	90
	Weight	1.00	0.36	0.13	0.08	0.05	0.05	0.05	0.08

Table 7.2. The weights for the amplitudes of multi-frequency pulses

7.1.2 Single-frequency Pulse and the Template for Cross-correlation

Single-frequency pulses are also used in our experiments. As introduced in Chapter 5, the time delay of a received signal can be estimated by cross-correlating the received signal with the transmitted signal template which is stored in a computer. As we have shown, the more similar the shape of a received signal and that of the template are, the more distinguishable the peak of the cross-correlation function will be, i.e., the better delay estimation will be.

To obtain a better delay estimation, the template used for the cross-correlation must be carefully selected. A received signal and a computer generated template are plotted in Figure 7.5. From the figure we can see that the shape of the computer-generated template, $p(t)$, is different from that of the received acoustical signal, $r(t)$, which is caused by the ringing of hydrophones, $h(t)$. Apparently, using the computer-generated signal as the transmitted signal template for the cross-correlation will affect the accuracy of delay estimation. So, to improve the delay estimation, the template for cross-correlation can be obtained by averaging some received acoustic signal pulses recorded in bubble-free

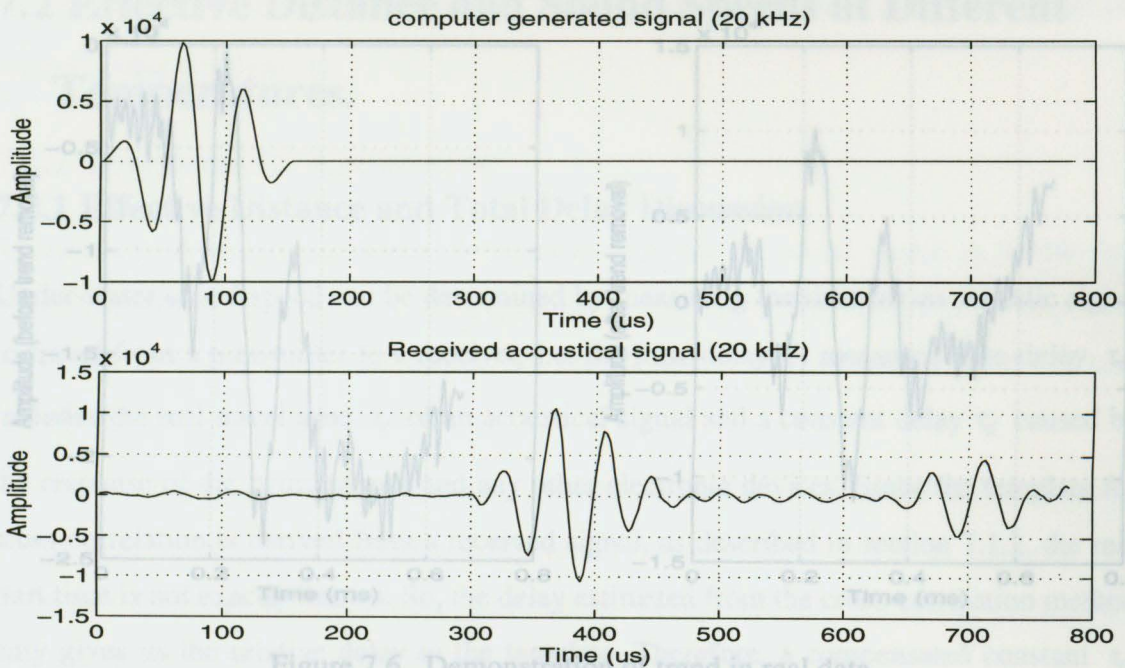


Figure 7.5 Comparison of templates.

water, i.e. $h(t) \otimes p(t)$, windowing the averaged pulse and then storing it in a computer.

7.1.3 Trend Removal

As discussed in section 5.2.3, in practical situations, recorded signals usually contain some frequency components whose periods are longer than the recorded data length. Those components are referred to as trends. Trends are caused by ambient noise and will effect the estimates of cross-correlation functions and thus the accuracy of delay estimations. Therefore, trends in a signal have to be removed. The left part of Figure 7.6 shows a signal recorded in the open sea. The trends in the data can be clearly seen. It is an extreme case of trend in the data. The right part of Figure 7.6 shows the improved signal after linear trend removal, which was introduced in section 5.2.3. In practical cases, during high sea states, higher-order trend removal may be necessary to recover a signal from higher-order trends. Another example is given in Figure 7.7, where the trend removal was an 8th order polynomial and was used in the field data processing presented in Chapter 8.

7.2 Effective Distance and Sound Speeds at Different Temperatures.

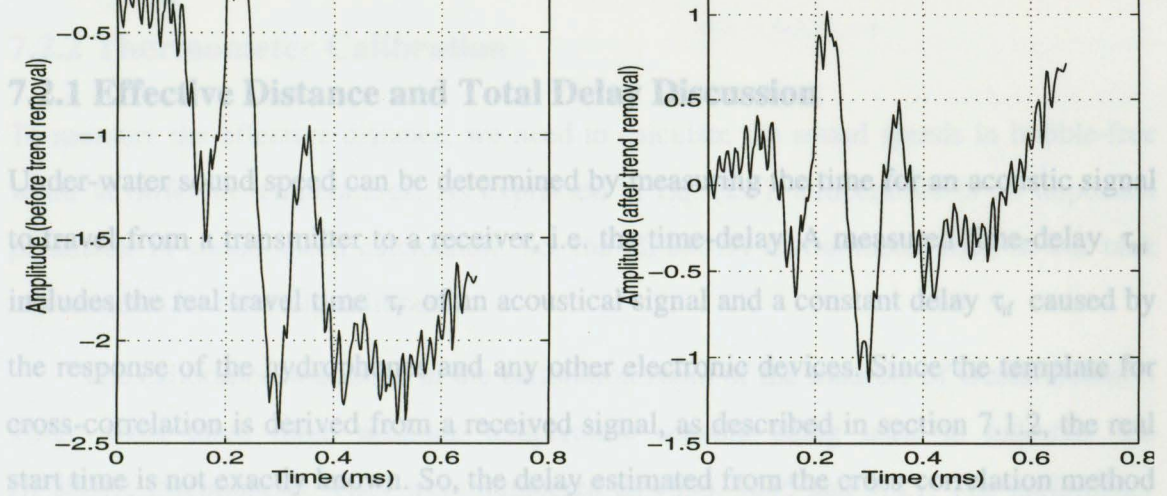


Figure 7.6 Demonstration of trend in real data.

Left: signal before trend removal; right: signal after linear trend removal.

time of an acoustical signal is

$$\tau = \tau_0 + \tau_1 + \tau_2 \quad (7.1)$$

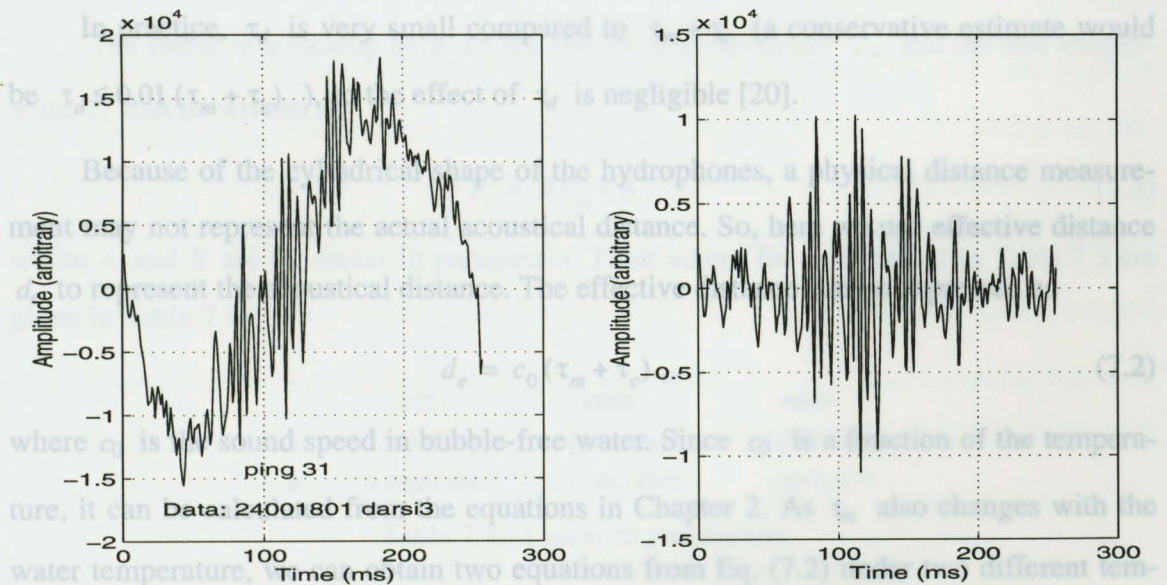


Figure 7.7 Demonstration of higher order trend removal

Left: signal before trend removal; Right: signal after trend removal with order

distance d_e and the compensation constant τ_c . In practice, more temperature measure-

7.2 Effective Distance and Sound Speeds at Different Temperatures.

7.2.2 Thermometer Calibration

7.2.1 Effective Distance and Total Delay Discussion

To measure the effective distance, we need to calculate the sound speeds in bubble-free water. Under-water sound speed can be determined by measuring the time for an acoustic signal to travel from a transmitter to a receiver, i.e. the time-delay. A measured time-delay τ_m includes the real travel time τ_r of an acoustical signal and a constant delay τ_d caused by the response of the hydrophones and any other electronic devices. Since the template for cross-correlation is derived from a received signal, as described in section 7.1.2, the real start time is not exactly known. So, the delay estimated from the cross-correlation method only gives us the relative delay to the template. Therefore, a compensated constant τ_c must be added to τ_m to eliminate the effect caused by the template. Then the real travel time of an acoustical signal is

$$\tau_r = \tau_m + \tau_c - \tau_d. \quad (7.1)$$

In practice, τ_d is very small compared to $\tau_m + \tau_c$ (a conservative estimate would be $\tau_d \leq 0.01 (\tau_m + \tau_c)$), so the effect of τ_d is negligible [20].

Because of the cylindrical shape of the hydrophones, a physical distance measurement may not represent the actual acoustical distance. So, here we use effective distance d_e to represent the acoustical distance. The effective distance can be expressed as given in Table 7.4.

$$d_e = c_0 (\tau_m + \tau_c), \quad (7.2)$$

where c_0 is the sound speed in bubble-free water. Since c_0 is a function of the temperature, it can be calculated from the equations in Chapter 2. As τ_m also changes with the water temperature, we can obtain two equations from Eq. (7.2) under two different temperatures. Then by solving the resulting two equations, we can determine the effective distance d_e and the compensation constant τ_c . In practice, more temperature measure-

ments may be needed to obtain the best estimates of the effective distance d_e and the compensative constant τ_c .

7.2.2 Thermometer Calibration

To measure the effective distance, we need to calculate the sound speeds in bubble-free water at different temperatures. As expressed in Eq. (2.9), temperature is an important parameter in sound-speed calculation. So, the HP2801A thermometer used in our tank test needs to be carefully calibrated.

The calibration was done in the calibration room of the Institute of Ocean Science. There were three more accurate temperature sensors being used to calibrate the HP2801A thermometer. They were numbered as #658, #645 and #521. The preliminary calibrations of those more accurate sensors are given in Table 7.3.

type	Real	#521	#658	#645
Temperature (c)	0.010	0.013	0.011	0.010
	26.868	26.866	26.873	26.871

Table 7.3. The preliminary calibrations of the higher standard sensors

The linear relationship between the measured temperature T_m and the real temperature T_r can be written as,

$$T_r = BT_m + A, \quad (7.3)$$

where A and B are the linear-fit parameters. Their values for calibrations in Table 7.3 are given in Table 7.4.

	#521	#658	#645
A	0.00300186	0.00099851	-0.00000112
B	0.99981384	1.00014893	1.00011170

Table 7.4. Linear fit parameters

Table 7.5. Calibration parameters of HP2801A

7.2.3 Measurement of Effective Distance and Sound Speeds at Different Temperatures

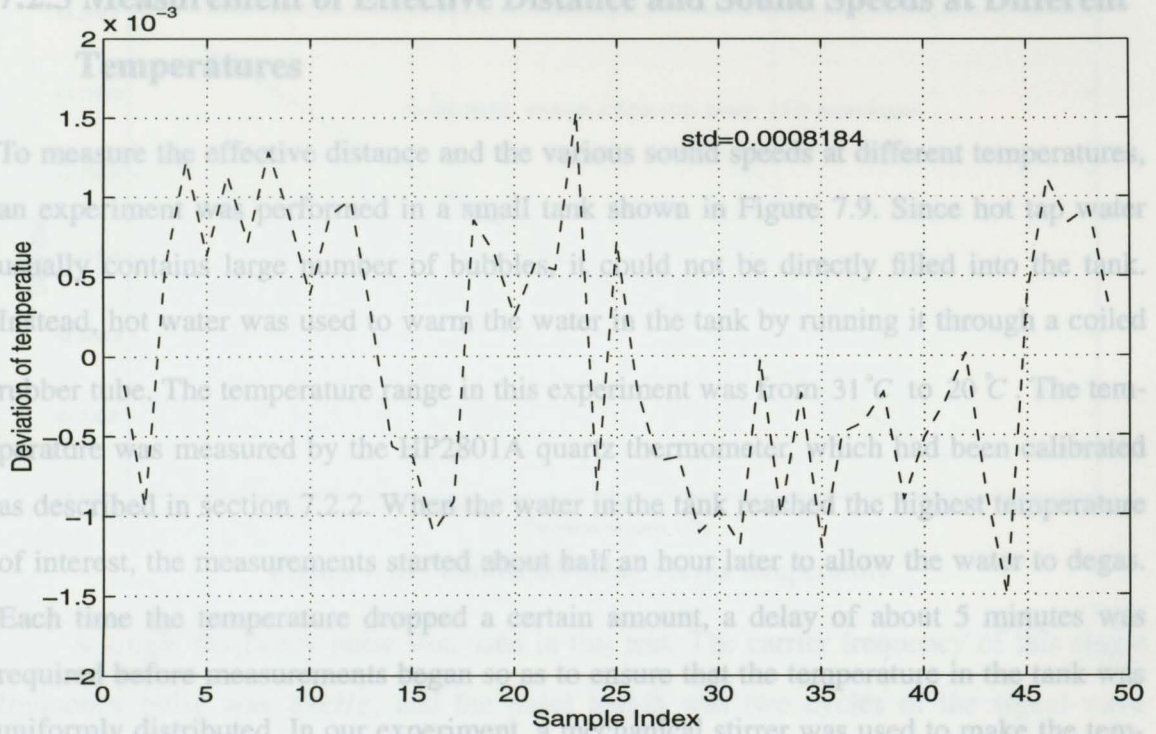


Figure 7.8 Temperature deviation of calibrated HP2801A

The HP2801A sensor was put into a tank with the more accurate sensors. The water temperature there was gradually decreased from 25°C to 3°C by 2°C steps and kept for 2 minutes for each measurement. The temperatures measured by the HP2801A are linearly fitted to the average of the more accurate sensors' calibrated measurements. The temperature deviation of the calibrated HP2801A is plotted in Figure 7.8. The standard deviation of the calibrated temperature is less than 10^{-3} °C. By using Eq. (2.9), we find that the accuracy of the sound speed calculation is about $\pm 5 \times 10^{-3}$ (m/s) under this temperature accuracy. The calibration parameters of the HP2801A are listed in Table 7.5, where A and B are the parameters in Eq. (7.3).

A	-0.264551642
B	0.997810031

Table 7.5. Calibration parameters of HP2801A

Figure 7.9 Demonstration of temperature test in a small tank

7.2.3 Measurement of Effective Distance and Sound Speeds at Different Temperatures

To measure the effective distance and the various sound speeds at different temperatures, an experiment was performed in a small tank shown in Figure 7.9. Since hot tap water usually contains large number of bubbles, it could not be directly filled into the tank. Instead, hot water was used to warm the water in the tank by running it through a coiled rubber tube. The temperature range in this experiment was from 31°C to 20°C . The temperature was measured by the HP2801A quartz thermometer, which had been calibrated as described in section 7.2.2. When the water in the tank reached the highest temperature of interest, the measurements started about half an hour later to allow the water to degas. Each time the temperature dropped a certain amount, a delay of about 5 minutes was required before measurements began so as to ensure that the temperature in the tank was uniformly distributed. In our experiment, a mechanical stirrer was used to make the temperature uniformly distributed, and ice cubes were used to drop the water temperature.

Using the cross-correlation method introduced in Chapter 5, the delay of the received signal was estimated. To obtain a better delay estimation, the signal-to-noise ratio needed to be improved by averaging every ten pings. The estimated delay versus temperature is plotted in Figure 7.10. The standard deviation of the estimated delay, 2.45×10^{-5} s, was obtained by averaging the standard deviation at different temperatures. It is very close to the Cramer-Rao lower bound which will be discussed in section 7.3.1. The compensation delay τ_c in Eq. (7.2) is $9 \mu\text{s}$ which was obtained by minimizing the variation of the effective distance at different temperatures. The effective distance calculated from Eq. (7.2) is 0.467 m. The variation of the effective distances at different temperatures is plotted in Figure 7.11. It shows that the standard deviation of the estimated effective distances at different temperatures is 2.5×10^{-5} m. These results are quite good. The variation of the effective distance estimation may be caused by minor temperature variation during the experiment.

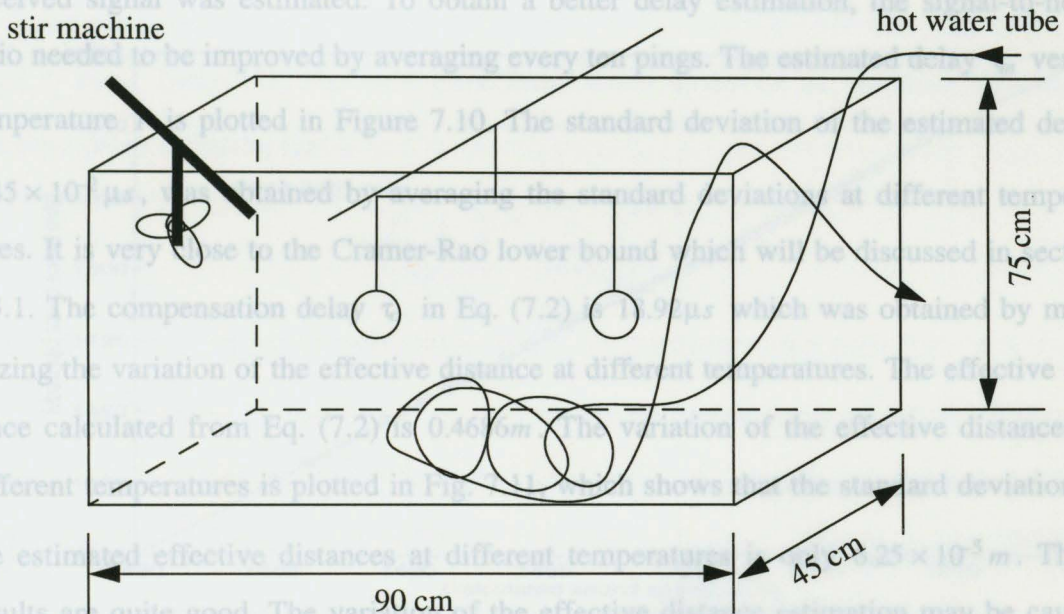


Figure 7.9 Demonstration of temperature test in a small tank

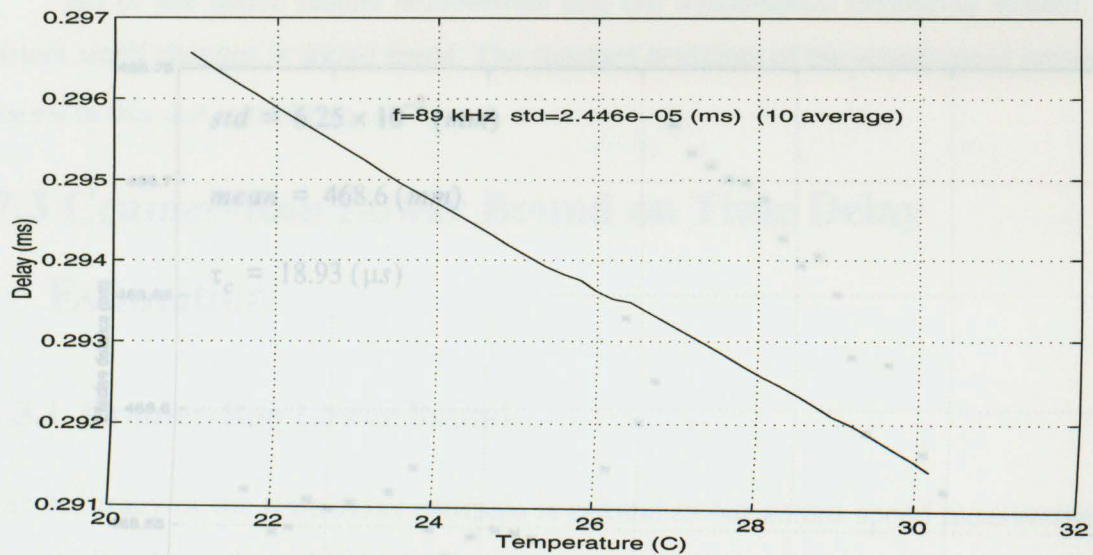


Figure 7.10 Estimated delay versus temperature

A single frequency pulse was used in this test. The carrier frequency of this single frequency pulse was 89kHz , and the pulse length was two cycles of the signal-wave length. The signal was transmitted at the rate of 4Hz .

Using the cross-correlation method introduced in Chapter 5, the delay of the received signal was estimated. To obtain a better delay estimation, the signal-to-noise ratio needed to be improved by averaging every ten pings. The estimated delay τ_m versus temperature T is plotted in Figure 7.10. The standard deviation of the estimated delay, $2.45 \times 10^{-2} \mu\text{s}$, was obtained by averaging the standard deviations at different temperatures. It is very close to the Cramer-Rao lower bound which will be discussed in section 7.3.1. The compensation delay τ_c in Eq. (7.2) is $18.92\mu\text{s}$ which was obtained by minimizing the variation of the effective distance at different temperatures. The effective distance calculated from Eq. (7.2) is 0.4686m . The variation of the effective distances at different temperatures is plotted in Fig. 7.11, which shows that the standard deviation of the estimated effective distances at different temperatures is only $6.25 \times 10^{-5}\text{m}$. These results are quite good. The variation of the effective distance estimation may be caused by minor temperature variation during the experiment.

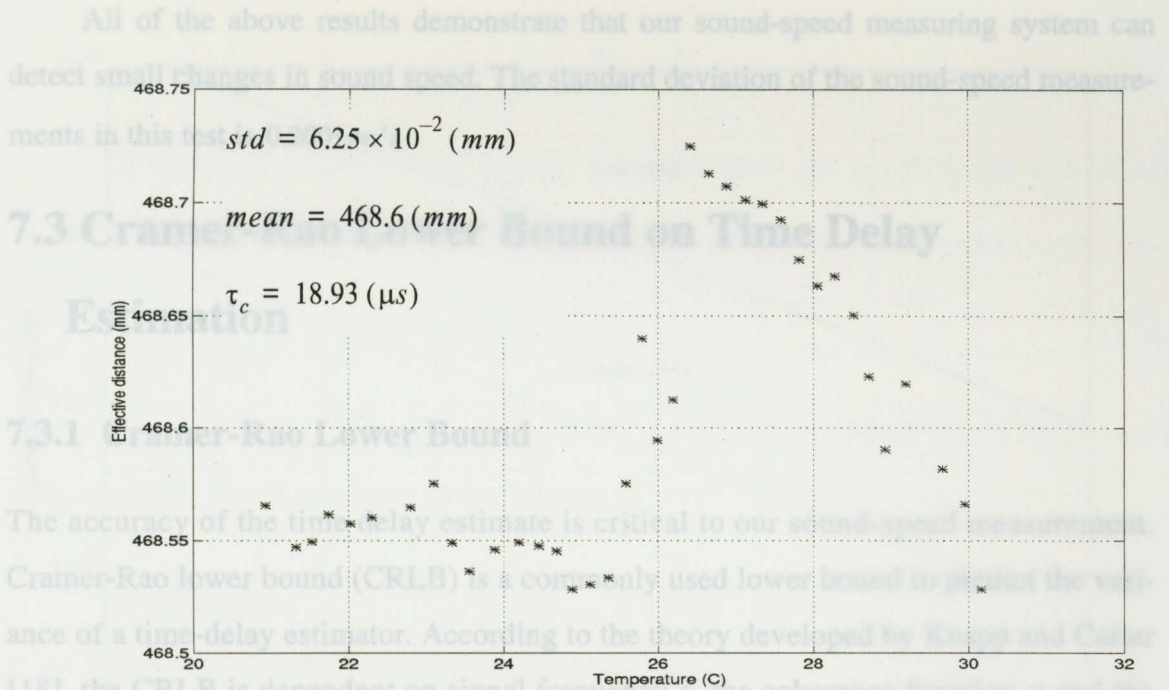


Figure 7.11 Variation of estimated effective distance versus temperature

A comparison between the calculated sound speeds using Eq. (2.33) and the estimated sound speeds are plotted in Figure 7.12, from which we can see that the results are very satisfactory.

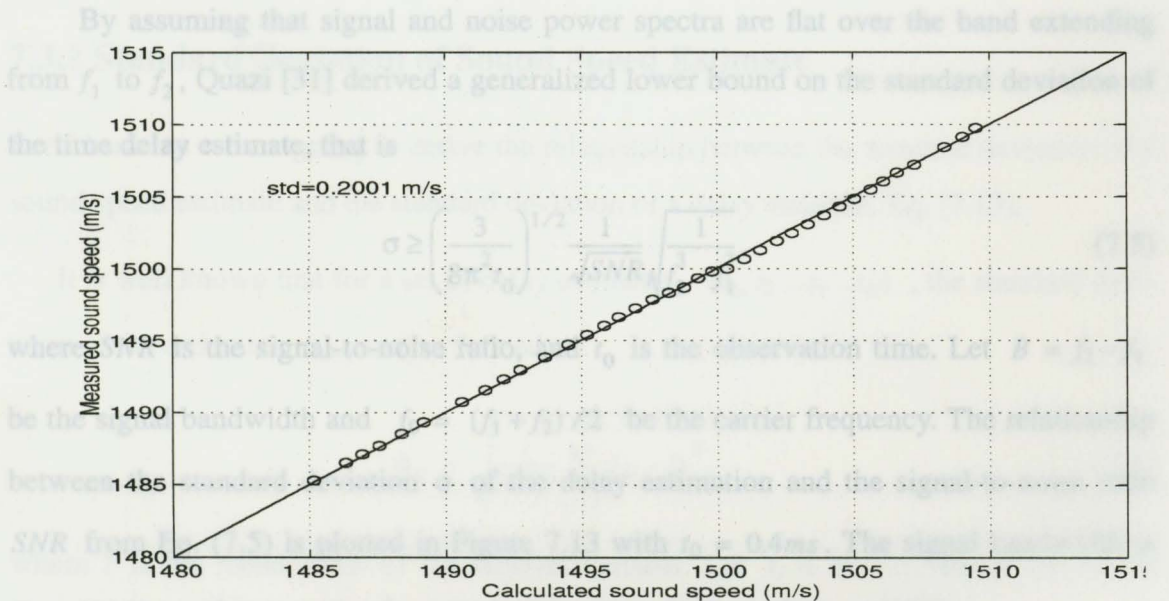


Figure 7.12 Comparison of measured sound speeds with the calculated sound speeds at different temperatures.

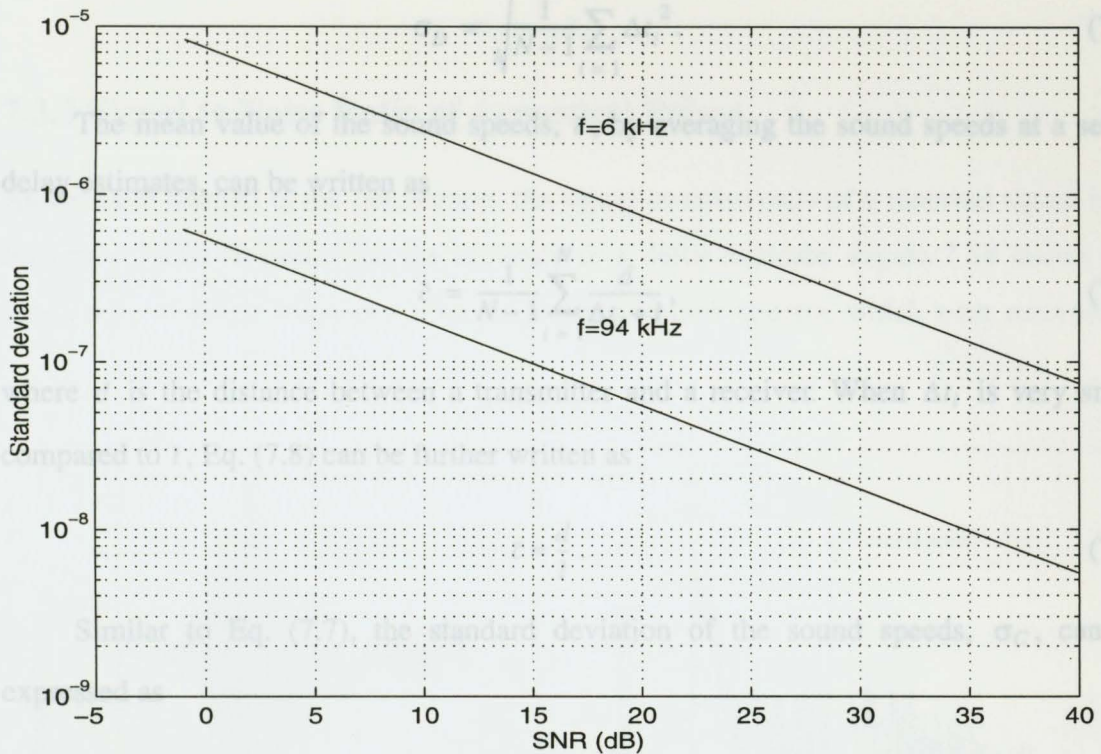


Figure 7.13 Cramer-Rao lower bound on the standard deviation of the time delay estimate (observation time $T=0.4$ ms; signal bandwidth $B=12$ kHz).

7.3.2 Standard Deviation of Sound Speed Estimate

In this section we are going to derive the relationship between the standard deviation of a sound speed estimate and the standard deviation of a delay estimate, Eq. (7.13).

It is well known that for a set of delay estimates, $(t_1, t_2 \dots t_i \dots t_N)$, the standard deviation of the estimates, σ_D , can be defined as

$$\sigma_D = \sqrt{\frac{1}{N-1} \sum_{i=1}^N (t_i - \bar{t})^2}, \quad (7.6)$$

where \bar{t} is the mean value of the random variable. Let $t_i = \Delta t_i + \bar{t}$, where Δt_i is the deviation of x_i , then Eq. (7.6) can be written as

$$\sigma_D = \sqrt{\frac{1}{N-1} \sum_{i=1}^N \Delta t_i^2}. \quad (7.7)$$

The mean value of the sound speeds, \bar{c} , by averaging the sound speeds at a set of delay estimates, can be written as

$$\bar{c} = \frac{1}{N-1} \sum_{i=1}^N \frac{d}{\Delta t_i + \bar{t}}, \quad (7.8)$$

where d is the distance between a transmitter and a receiver. When Δt_i is very small compared to \bar{t} , Eq. (7.8) can be further written as

$$\bar{c} \approx \frac{d}{\bar{t}}. \quad (7.9)$$

Similar to Eq. (7.7), the standard deviation of the sound speeds, σ_C , can be expressed as

$$\sigma_C = \sqrt{\frac{1}{N-1} \sum_{i=1}^N \Delta c_i^2}. \quad (7.10)$$

By using Eq. (7.9), it can be written as

$$\sigma_C \approx \sqrt{\frac{1}{N-1} \sum_{i=1}^N d^2 \left(\frac{1}{\Delta t_i + \bar{t}} - \frac{1}{\bar{t}} \right)^2}. \quad (7.11)$$

and further

$$\sigma_C \approx \sqrt{\frac{1}{N-1} \sum_{i=1}^N \left(\frac{d}{\bar{t}} \right)^2 \left(\frac{1}{1 + \frac{\Delta t_i}{\bar{t}}} - 1 \right)^2}. \quad (7.12)$$

Using Eq. (7.7) and Taylor series to $1/(1 + (\Delta t_i)/\bar{t})$, we can obtain the relationship between the standard deviation of sound speeds σ_C and that of the time-delay estimations σ_D , i.e.

Figure 7.14 Time-series of received acoustic pulses and their energy spectra. Recorded in the open ocean with a wind speed of about 6 m/s.

$$\sigma_C \approx \frac{\bar{c}^2}{d} \sigma_D \quad (7.13)$$

7.3.3 Signal to Noise Ratio of Acoustical Pulses

As we have learned in the last section, the signal-to-noise ratio of a received signal is an important factor to determine the accuracy of a delay estimate. Figure 7.14 shows two time series of single frequency acoustic pulses and their spectra, which were recorded in

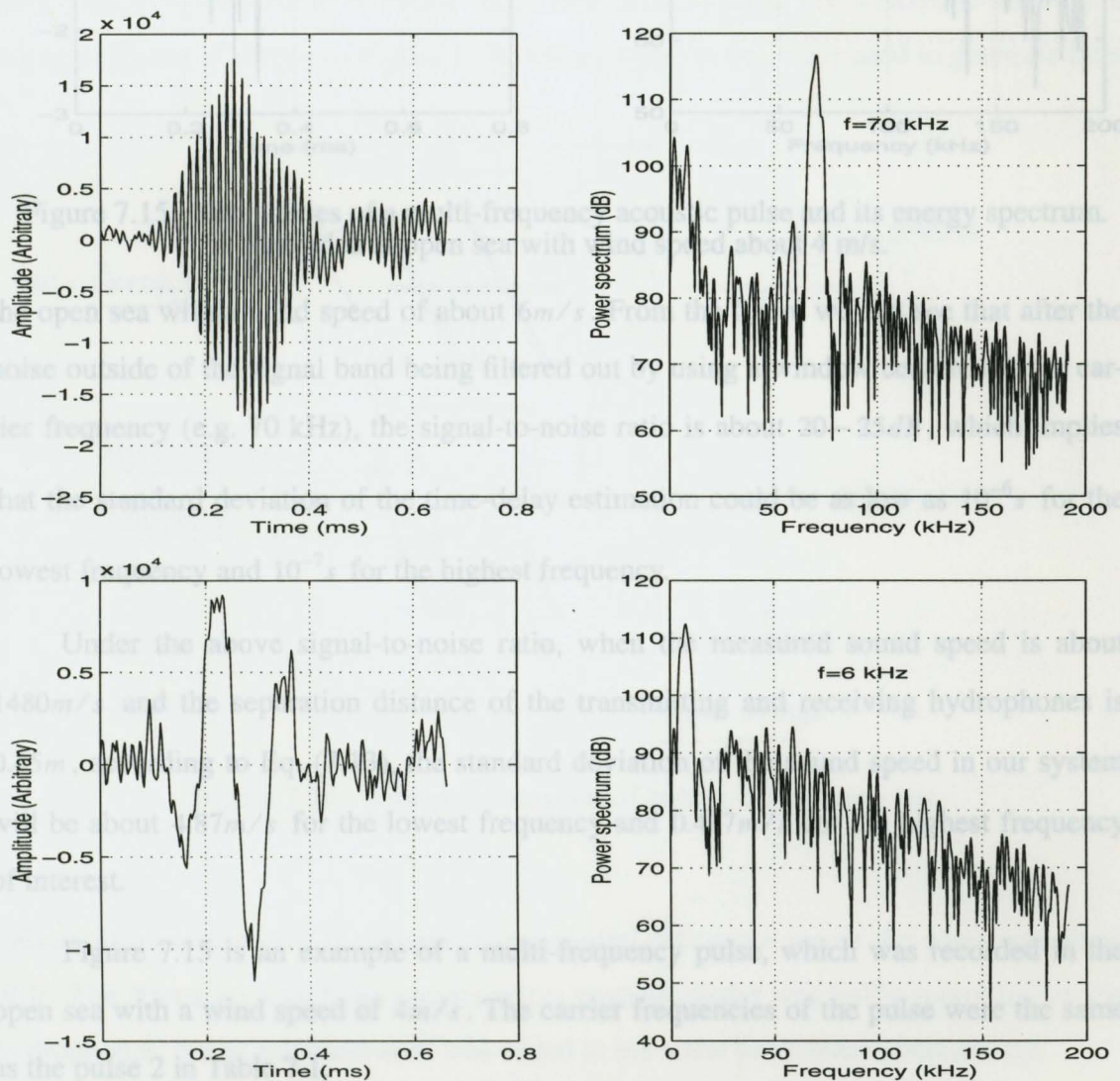


Figure 7.14 Time-series of received acoustic pulses and their energy spectra. Recorded in the open ocean with a wind speed of about 6 m/s.

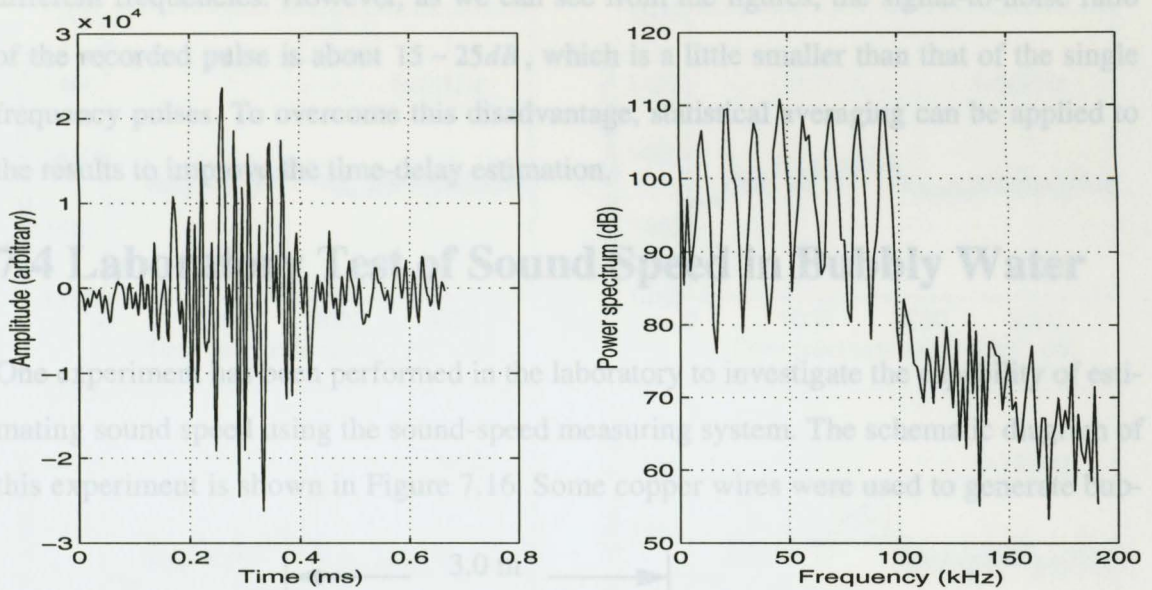


Figure 7.15 Time-series of a multi-frequency acoustic pulse and its energy spectrum. Recorded at open sea with wind speed about 4 m/s.

the open sea with a wind speed of about 6 m/s. From the figure we can see that after the noise outside of the signal band being filtered out by using a window centered at the carrier frequency (e.g. 70 kHz), the signal-to-noise ratio is about 20 ~ 25 dB, which implies that the standard deviation of the time-delay estimation could be as low as 10^{-6} s for the lowest frequency and 10^{-7} s for the highest frequency.

Under the above signal-to-noise ratio, when the measured sound speed is about 1480 m/s and the separation distance of the transmitting and receiving hydrophones is 0.45 m, according to Eq. (7.13), the standard deviation of the sound speed in our system will be about 4.87 m/s for the lowest frequency and 0.487 m/s for the highest frequency of interest.

Figure 7.15 is an example of a multi-frequency pulse, which was recorded in the open sea with a wind speed of 4 m/s. The carrier frequencies of the pulse were the same as the pulse 2 in Table 7.1.

Multi-frequency pulses can give us simultaneous measurements of sound speeds at

different frequencies. However, as we can see from the figures, the signal-to-noise ratio of the recorded pulse is about $15 \sim 25\text{dB}$, which is a little smaller than that of the single frequency pulses. To overcome this disadvantage, statistical averaging can be applied to the results to improve the time-delay estimation.

7.4 Laboratory Test of Sound Speed in Bubbly Water

One experiment has been performed in the laboratory to investigate the capability of estimating sound speed using the sound-speed measuring system. The schematic diagram of this experiment is shown in Figure 7.16. Some copper wires were used to generate bub-

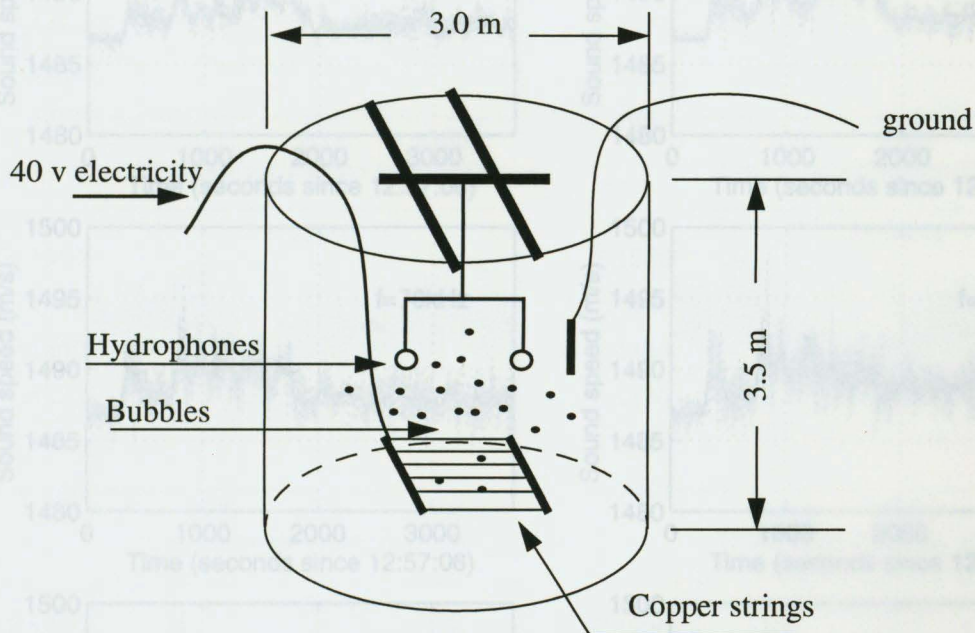


Figure 7.16 Schematic diagram of bubble distribution test.

bles using an electrolytic technique. The potential difference across the wires was about 40V. The frame on which the copper wires were mounted was half a metre below the hydrophones. Some sulphuric-acid was added to the water to increase conductivity.

The signals used in this experiment were two multi-frequency pulses, the initial

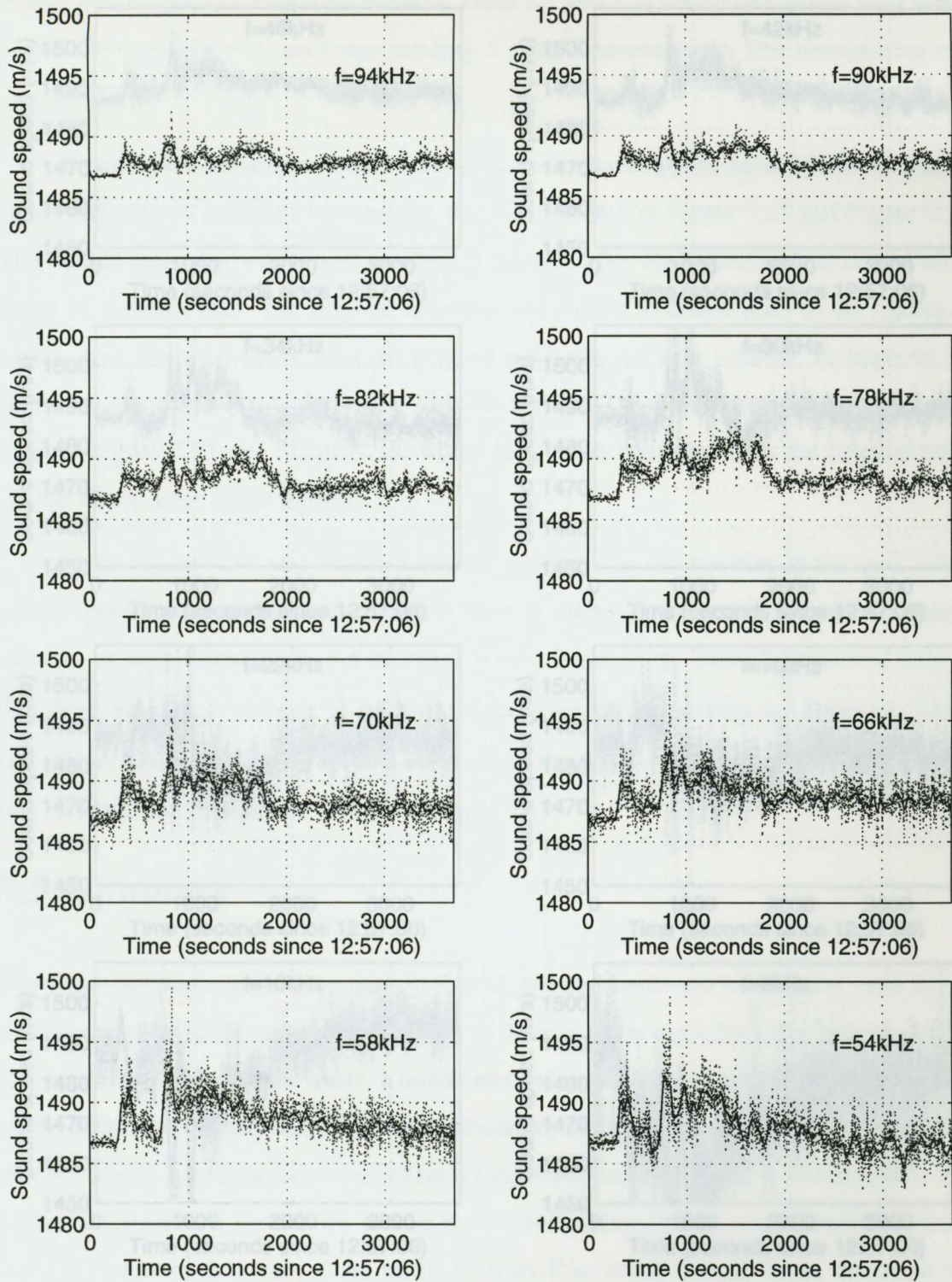


Figure 7.17 Sound speeds vs. time at different frequencies (laboratory study using electrolytically generated bubbles; Data: Nov22/94).
 Dash-dotted line: original estimates; solid line: lowpass filtered estimates.

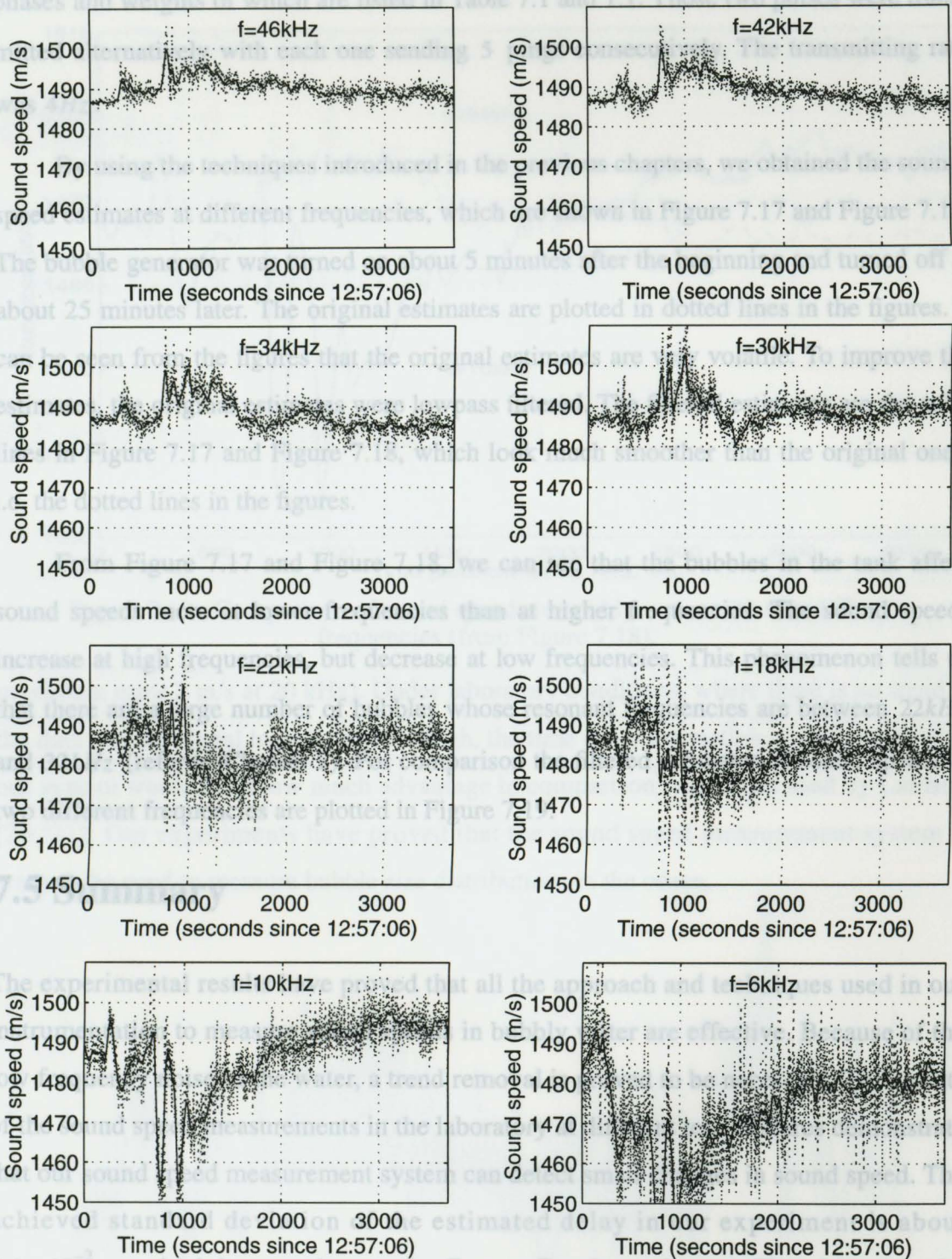


Figure 7.18 Sound speeds at different frequencies (laboratory study using electrolytically generated bubbles. Data: Nov.22/94).

Dash-dotted line: original estimates; solid line: lowpass filtered estimates.

phases and weights of which are listed in Table 7.1 and 7.1. Those two pulses were transmitted alternatively with each one sending 5 pings consecutively. The transmitting rate was 4Hz .

By using the techniques introduced in the previous chapters, we obtained the sound-speed estimates at different frequencies, which are shown in Figure 7.17 and Figure 7.18. The bubble generator was turned on about 5 minutes after the beginning and turned off at about 25 minutes later. The original estimates are plotted in dotted lines in the figures. It can be seen from the figures that the original estimates are very volatile. To improve the estimates, the original estimates were lowpass filtered. The filtered estimates are the solid lines in Figure 7.17 and Figure 7.18, which look much smoother than the original ones, i.e. the dotted lines in the figures.

From Figure 7.17 and Figure 7.18, we can see that the bubbles in the tank affect sound speeds more at lower frequencies than at higher frequencies. The sound speeds increase at high frequencies, but decrease at low frequencies. This phenomenon tells us that there are a large number of bubbles whose resonant frequencies are between 22kHz and 32kHz (refer to Chapter 2). For comparison the filtered estimates of sound speeds at two different frequencies are plotted in Figure 7.19.

7.5 Summary

The experimental results have proved that all the approach and techniques used in our instrumentation to measure sound speeds in bubbly water are effective. Because of the low frequency noise in the water, a trend removal is proved to be necessary. The results of the sound speed measurements in the laboratory at different temperatures demonstrate that our sound speed measurement system can detect small changes in sound speed. The achieved standard deviation of the estimated delay in our experiment is about $2.4 \times 10^{-2} \mu\text{s}$, which is very close to the Cramer-Rao lower bound. Thus, based on the accuracy of the delay estimation, we can measure a sound speed variation at the standard deviation as low as 0.2 m/s at 89 kHz . This result may be compared with Lamarre's (i.e.

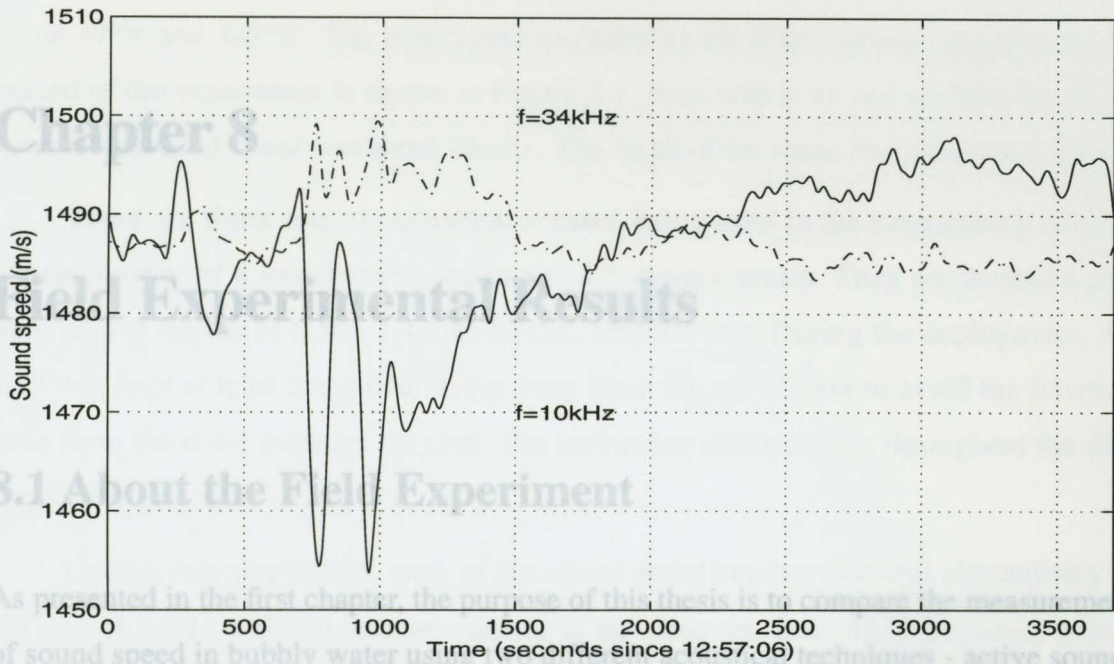


Figure 7.19 Comparison of sound speeds in bubbly water with two different frequencies (from Figure 7.18).

conduct the measurement with both techniques under the same conditions, has already been introduced in previous chapters. A field experiment with our instrument was conducted during the second two weeks of January 1995 off the west coast of Oregon. Our experiments have proved that the sound speed measurement system is ready to be used to measure bubble size distributions in the ocean.

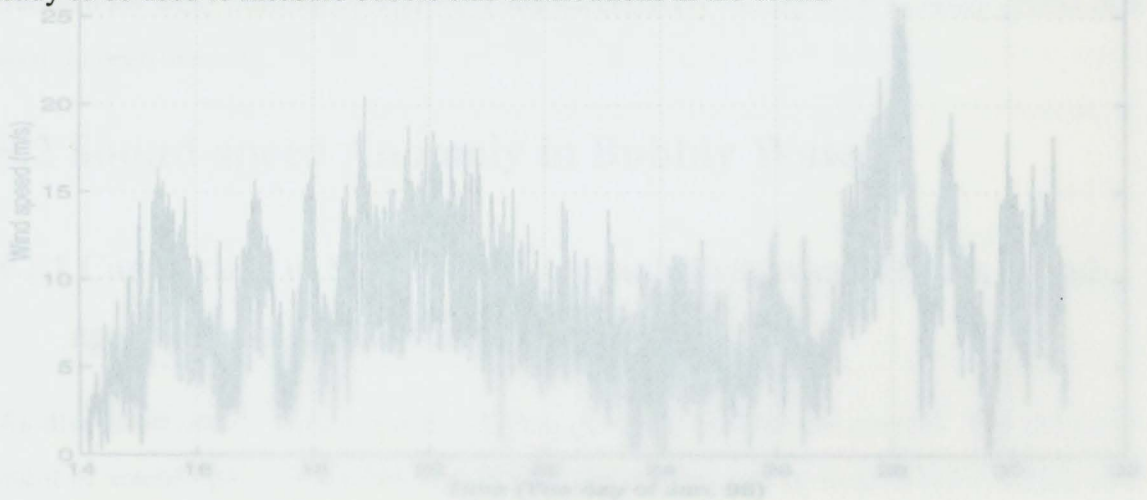


Figure 8.1 Wind speed during the experiment in January 1995.

State, about 50 nautical miles from Juan de Fuca Strait. The instrument was deployed at about 47°N and 128°W . The wind speed recorded by the ship's anemometer during the period of the experiment is shown in Figure 8.1, from which we can see that the maximum recorded was about 24m/s . The depth of the water was more than 2000m .

There are three sets of acoustical sensors being used in the experiment, each of which consists of a sound-speed sensor and a resonator sensor. They are mounted on a buoy and at depths of 0.5m , 1.4m and 3.2m , respectively. During the deployment, the ship was kept at least 5 nautical miles away from the instrument to avoid the interference from the noise made by the ship. The instrument drifted freely throughout the data

Field Experimental Results

8.1 About the Field Experiment

As presented in the first chapter, the purpose of this thesis is to compare the measurement of sound speed in bubbly water using two different acoustical techniques - active sound-speed measuring and resonator measuring techniques. Our instrument, which was used to conduct the measurement with both techniques under the same conditions, has already been introduced in previous chapters. A field experiment with our instrument was conducted during the second two weeks of January 1995 off the west coast of Washington

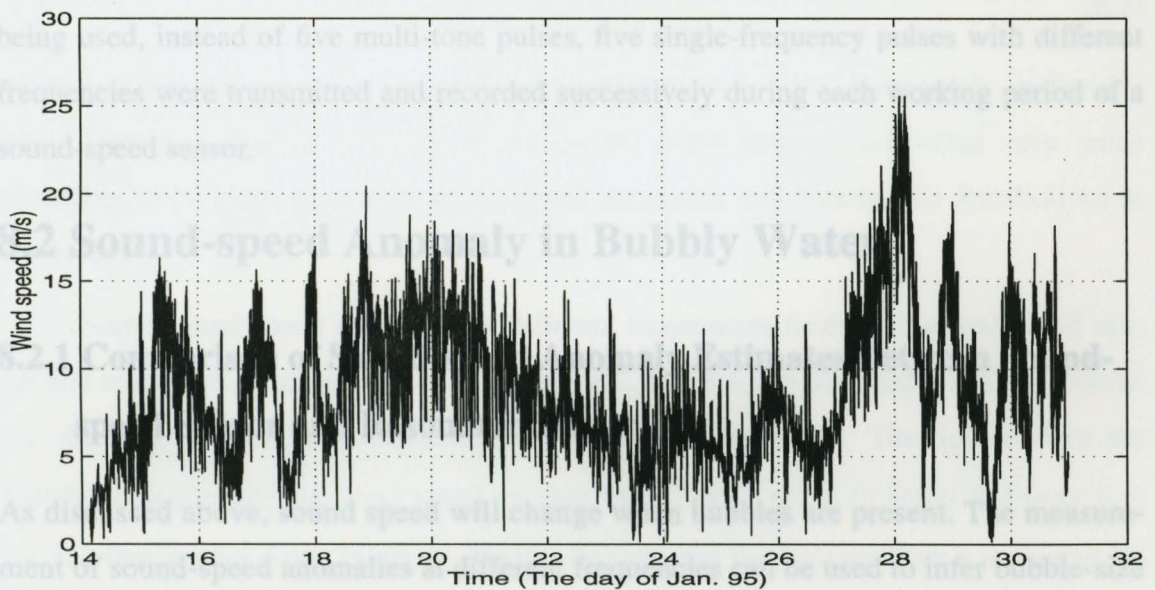


Figure 8.1 Wind speed during the experiment in January 1995.

State, about 50 nautical miles from Juan de Fuca Strait. The instrument was deployed at about $47^{\circ}N$ and $128^{\circ}W$. The wind speed recorded by the ship's anemometer during the period of the experiment is shown in Figure 8.1, from which we can see that the maximum steady wind speed was about $24m/s$. The depth of the water was more than $2000m$.

There are three sets of acoustical sensors being used in the experiment, each of which consists of a sound-speed sensor and a resonator sensor. They are mounted on a buoy and at depths of $0.5m$, $1.4m$ and $3.2m$, respectively. During the deployment, the ship was kept at least 5 nautical miles away from the instrument to avoid the interference from the noise made by the ship. The instrument drifted freely throughout the data acquisition period.

During data acquisition, each of the sound-speed sensors operated alternatively at the rate of $0.5Hz$ with the resonator sensor in the same set. Both multi-frequency pulses and single-frequency pulses for the sound-speed sensors were used. For the multi-frequency pulses, we used two pulses each of which has a different composition of frequencies as described in the last chapter. When multi-frequency pulses were being used, five pings were transmitted consecutively at a burst rate of $5Hz$ for each pulse during each working period of a sound-speed sensor. Similarly, when single-frequency pulses were being used, instead of five multi-tone pulses, five single-frequency pulses with different frequencies were transmitted and recorded successively during each working period of a sound-speed sensor.

8.2 Sound-speed Anomaly in Bubbly Water

8.2.1 Comparison of Sound-speed Anomaly Estimates Between Sound-speed Sensor and Resonator Sensor

As discussed above, sound speed will change when bubbles are present. The measurement of sound-speed anomalies at different frequencies can be used to infer bubble-size distribution. The sound-speed anomaly is defined as

$$\Delta c = c_m - c_0 \quad (8.1)$$

where c_m and c_0 are the sound speeds measured in bubbly and bubble free water, respectively. While the sound speed from a sound-speed sensor is determined by using the cross-correlation techniques introduced in chapter 5, the sound speed from a resonator is determined by the frequencies shifting away from its harmonic series in bubble-free water of known sound speed. According to Eq. (3.15), the sound-speed anomaly can be written as

$$\Delta c_n = \frac{2d}{n+1} [f_n - (n+1)f_b] = \frac{2d}{n+1} \Delta f \quad (8.2)$$

where n represents the n th harmonic frequency.

Note that when two neighboring harmonic peaks move toward each other, the maximum detectable frequency change Δf is $f_b/2$. From Eq. (8.2), we know that the detectable sound speed variation Δc_n is frequency dependent or depends on n , the order of the harmonics. The higher the frequency is, the smaller the detectable sound-speed variation will be. By using Eq. (3.15) and Eq. (8.2), we can see that

$$\Delta c_n < \frac{2d}{n+1} \cdot \frac{f_b}{2} = \frac{c_0}{2(n+1)} \quad (8.3)$$

when two neighboring harmonic peaks move toward each other. Fortunately, in the real world, two neighboring harmonic peaks do not move toward each other very much according to previous reports on sound-speed anomalies and bubble-size distributions in the ocean.

Some sound-speed anomalies at different frequencies from both sound-speed sensor and resonator sensor are shown in Figures 8.2, 8.3, 8.4, 8.5, 8.6, and 8.7. These results are obtained from the field experiment mentioned in Section 8.1. The figures show the four-hour results with the wind speed varying from $17m/s$ to $7m/s$ (refer to Figure 8.1) and the frequencies from $25kHz$ to $98kHz$. Because the frequencies from a resonator are determined by its harmonics, they may not be exactly the same as those from a sound-

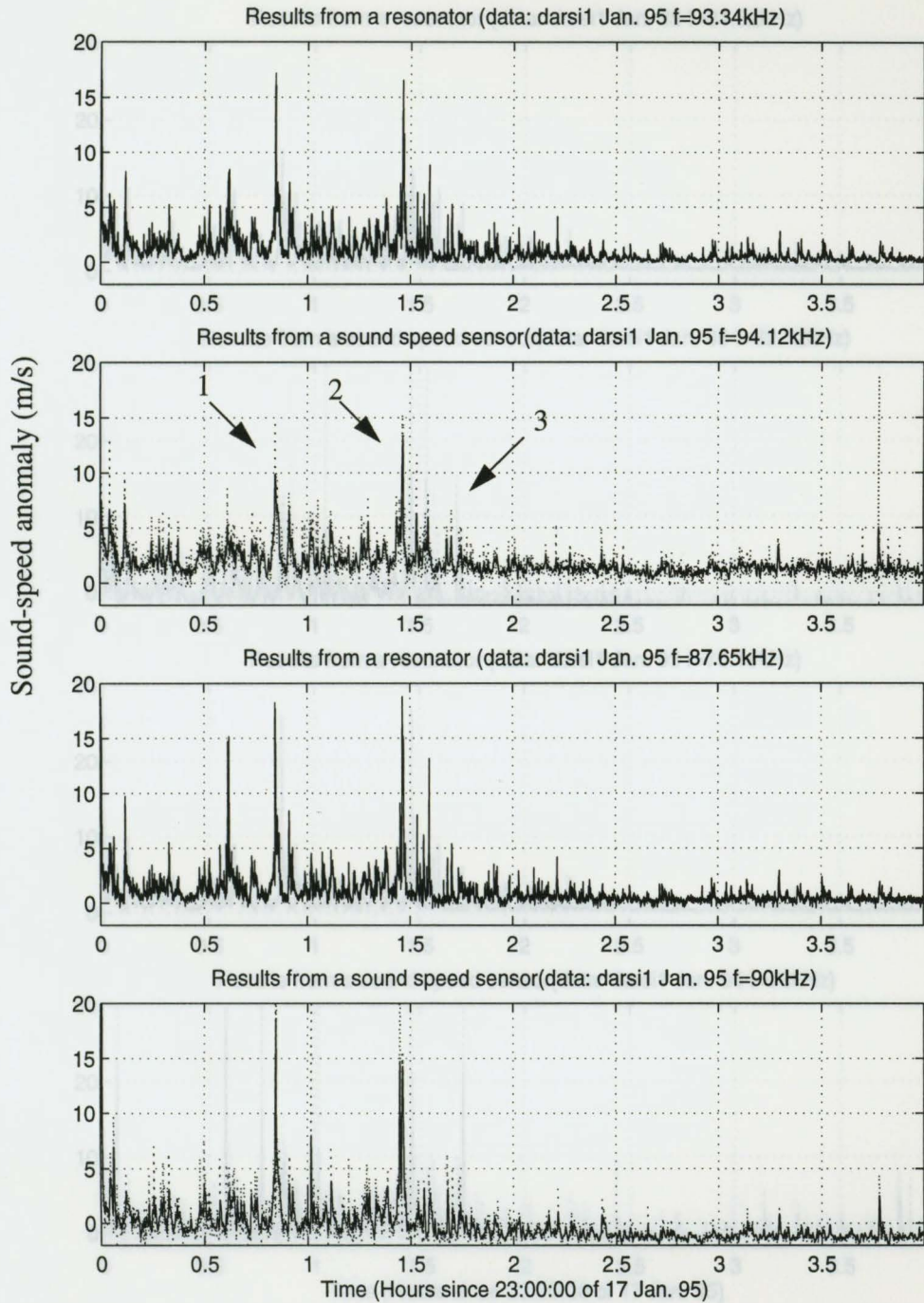


Figure 8.2 Comparison of sound-speed anomalies from a resonator sensor and a sound-speed frequencies at different frequencies; Depth=1.4 m.

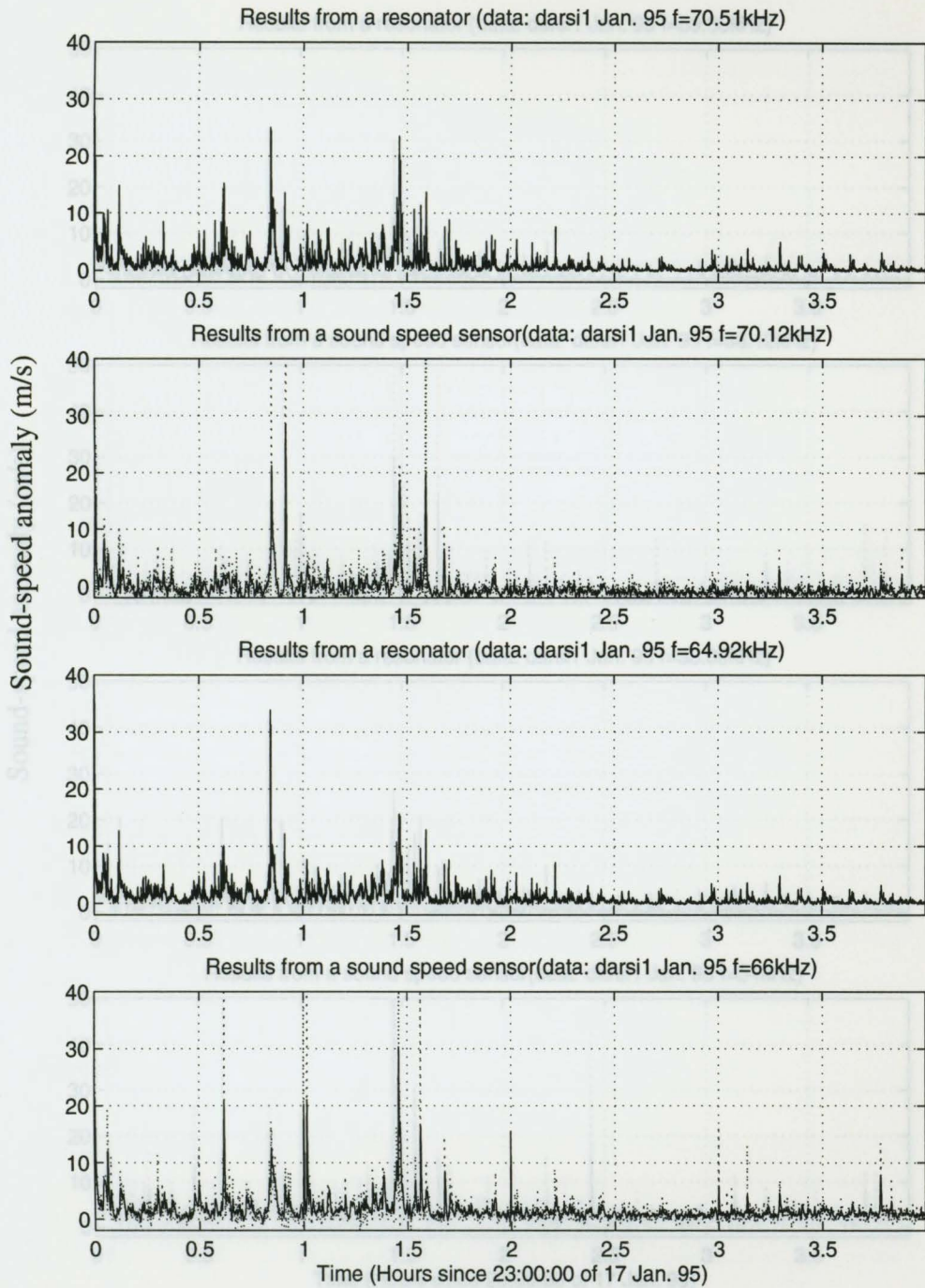


Figure 8.4 Comparison of sound-speed anomalies from a resonator sensor and a sound-speed sensor at different frequencies; Depth=1.4m. cont'd.

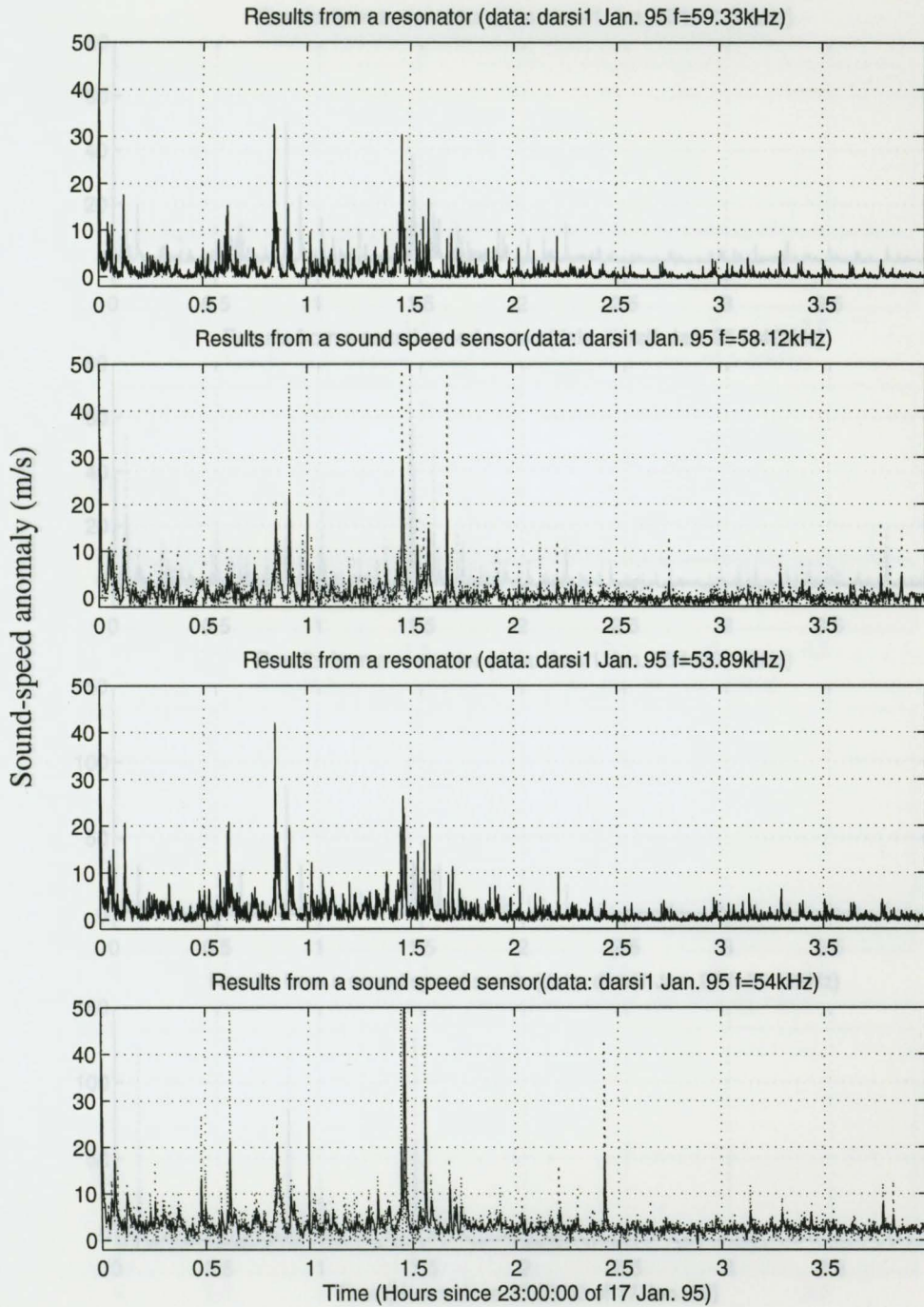


Figure 8.5 Comparison of sound-speed anomalies from a resonator sensor and sound-speed sensor at different frequencies; Depth=1.4m. cont'd.

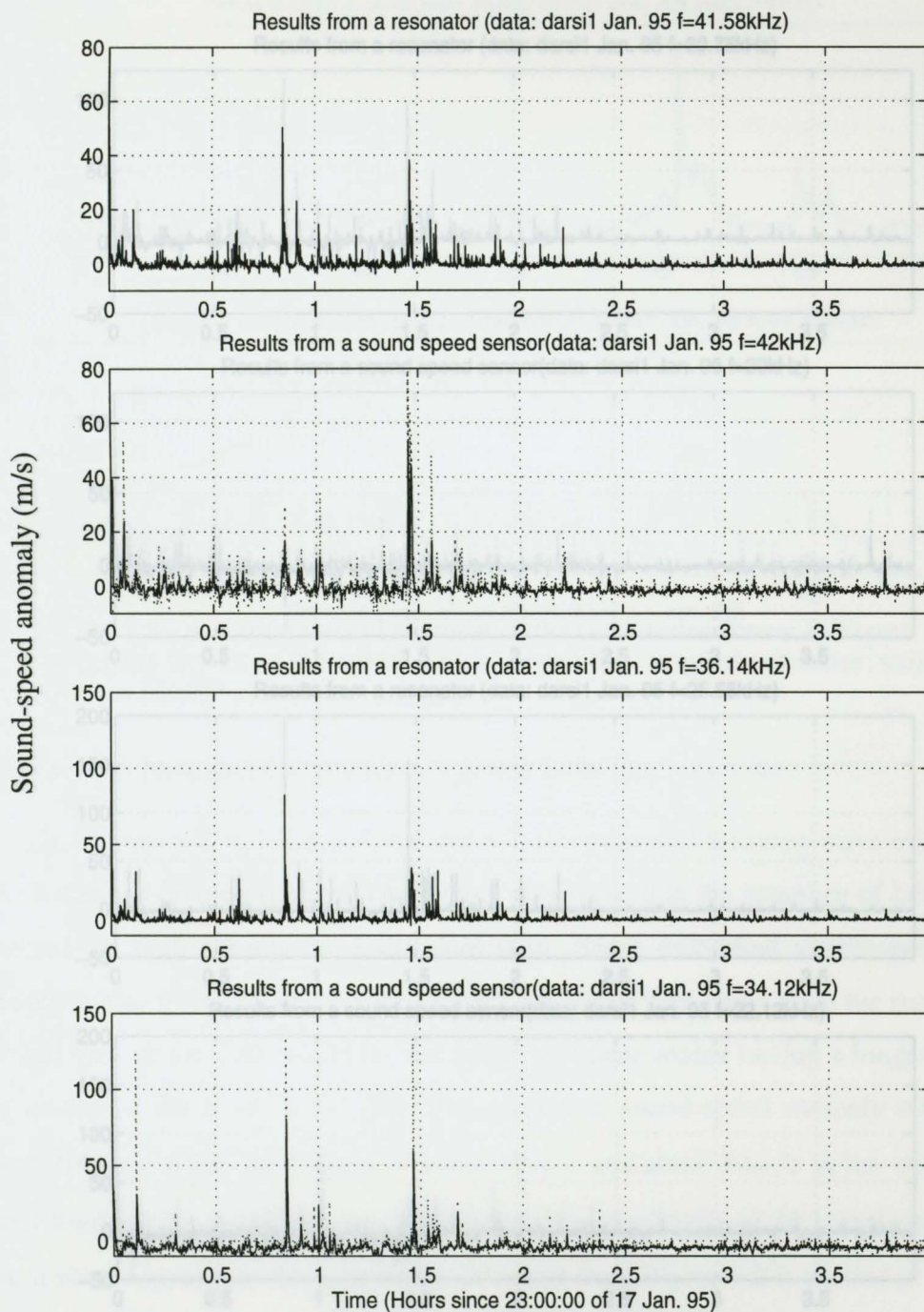


Figure 8.6 Comparison of sound-speed anomalies from a resonator sensor and a sound-speed sensor at different frequencies; Depth=1.4m. cont'd.

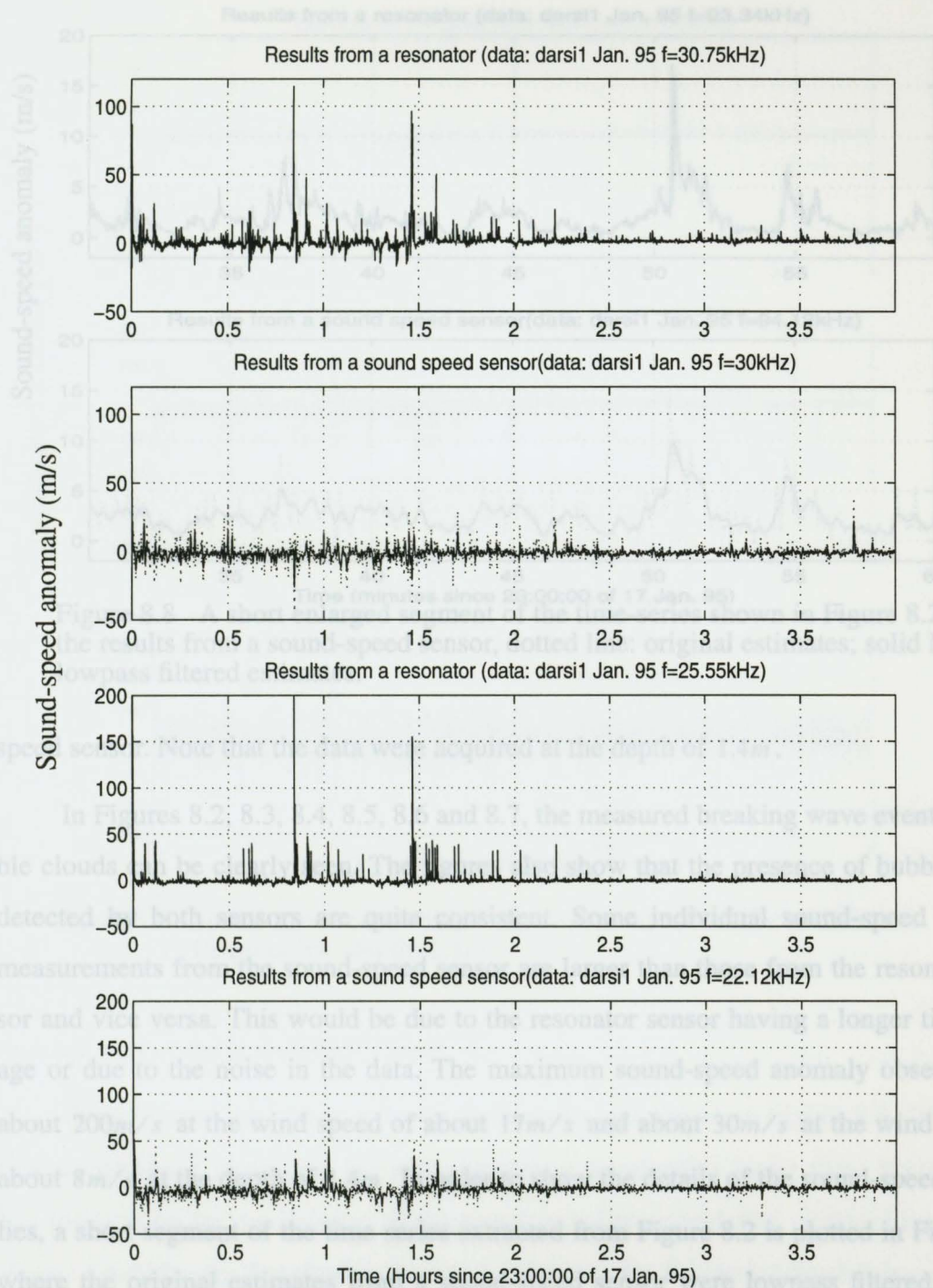


Figure 8.7 Comparison of sound-speed anomalies from a resonator sensor and a sound-speed sensor at different frequencies; Depth=1.4m. cont'd.

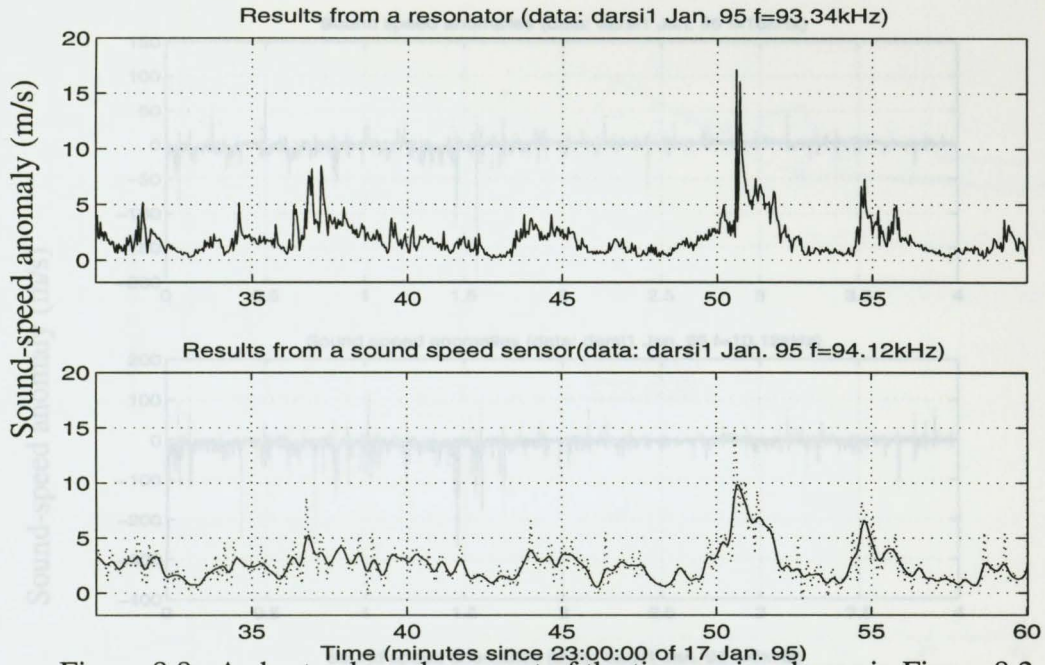


Figure 8.8 A short enlarged segment of the time-series shown in Figure 8.2. For the results from a sound-speed sensor, dotted line: original estimates; solid line: lowpass filtered estimates.

speed sensor. Note that the data were acquired at the depth of 1.4m .

In Figures 8.2, 8.3, 8.4, 8.5, 8.6 and 8.7, the measured breaking wave events or bubble clouds can be clearly seen. The figures also show that the presence of bubble clouds detected by both sensors are quite consistent. Some individual sound-speed anomaly measurements from the sound-speed sensor are larger than those from the resonator sensor and vice versa. This would be due to the resonator sensor having a longer time average or due to the noise in the data. The maximum sound-speed anomaly observed was about 200m/s at the wind speed of about 17m/s and about 30m/s at the wind speed of about 8m/s at the depth of 1.4m . In order to show the details of the sound-speed anomalies, a short segment of the time series extracted from Figure 8.2 is plotted in Figure 8.8, where the original estimates from a sound-speed sensor were lowpass filtered. A Hanning window was used for the lowpass filter. The window length of the lowpass filter

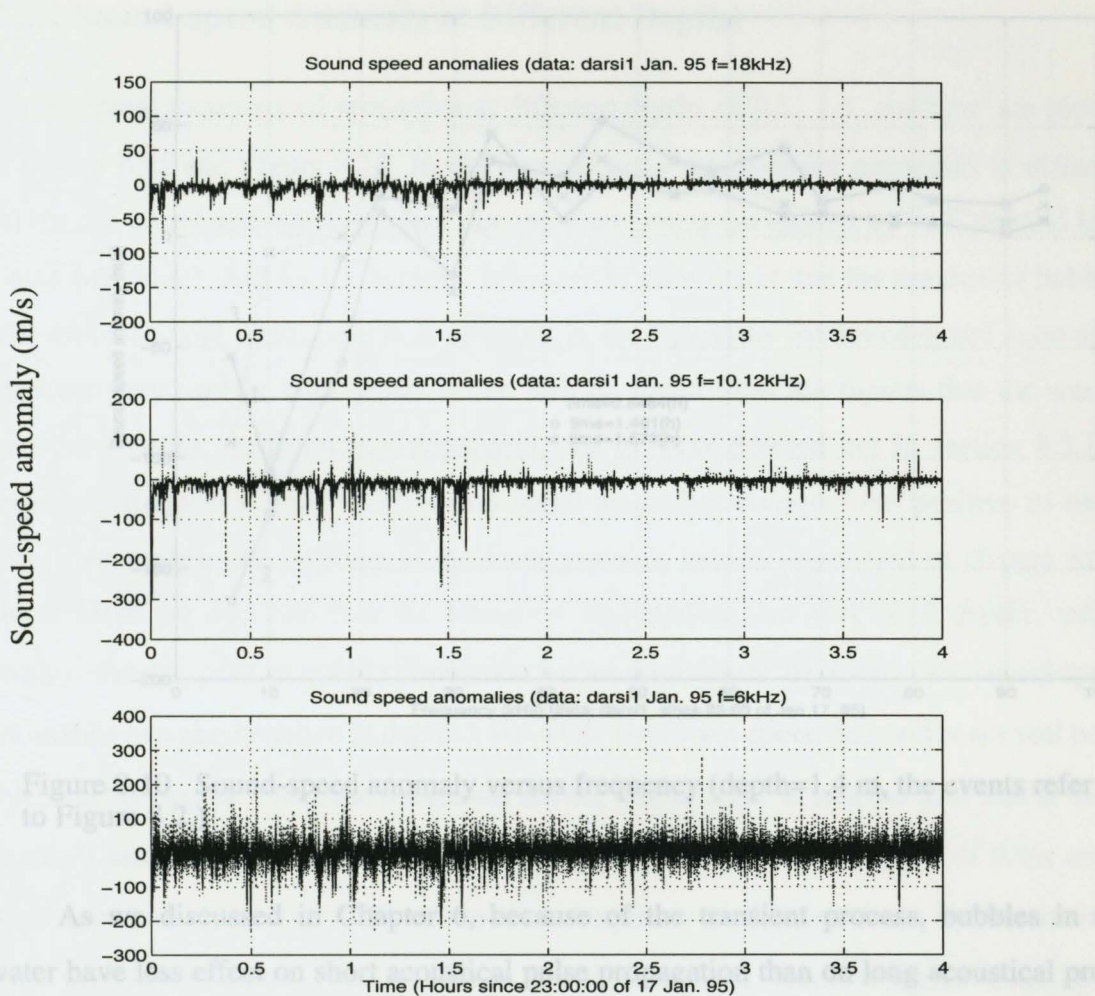


Figure 8.9 Sound-speed anomalies from a sound-speed sensor at different frequencies; Depth=1.4m.

was one half of the time-series' length.

Sound-speed anomalies at lower frequencies are shown in Figure 8.9. We can see that sound-speed anomalies become negative at frequencies lower than 18kHz , which has implication for the location of the peaks in bubble population or the changes in the slope of bubble-size distribution. Figure 8.10 shows the frequency dependence of sound-speed anomaly for specific events.

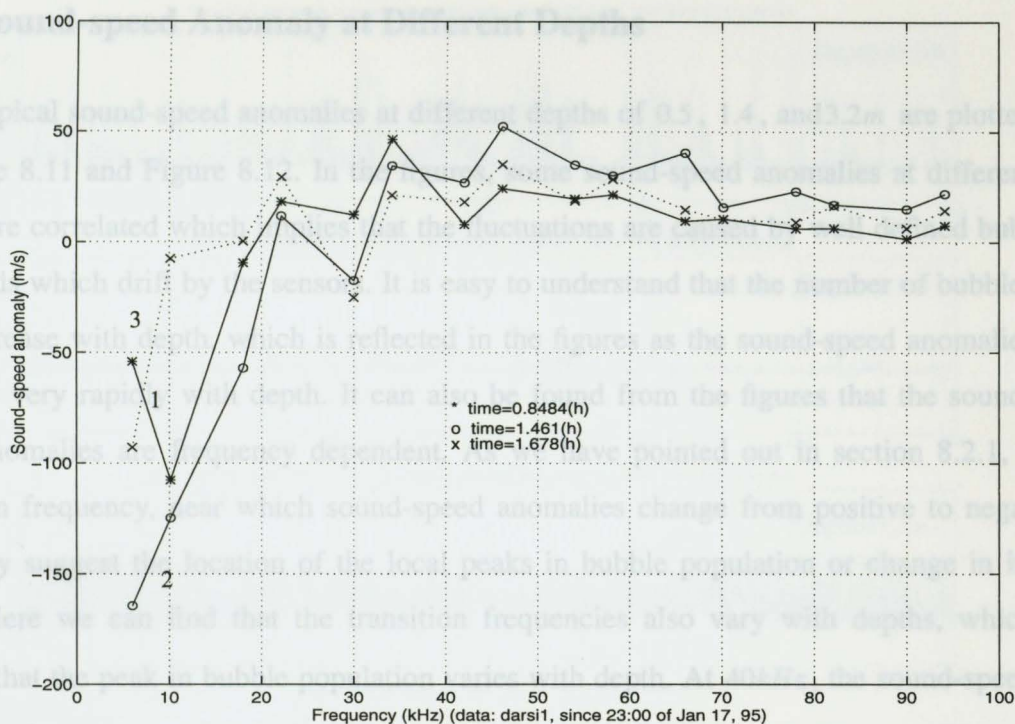


Figure 8.10 Sound-speed anomaly versus frequency (depth=1.4 m, the events refer to Figure 8.2.)

As we discussed in Chapter 6, because of the transient process, bubbles in the water have less effect on short acoustical pulse propagation than on long acoustical propagation, i.e. sound speeds estimated by using a short acoustical pulse will have less variation than that estimated by a long acoustical pulse. The duration of a transient process is determined by the initial phase of each individual bubble and the size of the bubble. When we apply Eq. (2.30) to a short acoustical pulse to infer bubble-size distribution, some error will be introduced. This is because Eq. (2.30) is for the sound speed in bubbly water and was derived from the steady state of bubble resonance. To obtain a correct bubble-size distribution estimation this error must be estimated. Since the lowest frequency of the resonator sensors available in this preliminary experiment is about 25kHz , the short pulse theory does not much affect the measurements for our current pulse length and the effect of short pulse can only be seen from the comparison in Figure 8.7 at fre-

quencies below 30kHz , consistent with the theoretical prediction.

8.2.2 Sound-speed Anomaly at Different Depths

Some typical sound-speed anomalies at different depths of 0.5 , 1.4 , and 3.2m are plotted in Figure 8.11 and Figure 8.12. In the figures, some sound-speed anomalies at different depths are correlated which implies that the fluctuations are caused by well defined bubble clouds which drift by the sensors. It is easy to understand that the number of bubbles will decrease with depth, which is reflected in the figures as the sound-speed anomalies decrease very rapidly with depth. It can also be found from the figures that the sound-speed anomalies are frequency dependent. As we have pointed out in section 8.2.1, a transition frequency, near which sound-speed anomalies change from positive to negative, may suggest the location of the local peaks in bubble population or change in its slope. Here we can find that the transition frequencies also vary with depths, which implies that the peak in bubble population varies with depth. At 40kHz , the sound-speed anomalies become negative at depth 3.4m while the sound-speed anomalies are still positive at other depths. Thus, the maximum bubble size at 3.2m is less than that at other depths. Lamarre [20, 21] reported a 40kHz transition frequency at a depth of 0.5m and a wind speed of about 8m/s . That transition frequency is different from the results here with wind speed about 17m/s . This is not unanticipated, since at higher wind speed larger bubbles are entrained, leading to a lower frequency separating sound speed increase from sound speed decrease. Moreover, large bubbles rise faster than small bubbles. Thus, the population of large bubbles close to the surface will exceed that in deeper water, with corresponding change in transition frequency. To show the details of the sound-speed anomalies at different depths, some short segments of the data extracted from the Figure 8.11 and Figure 8.12 are plotted in Figures 8.13 and Figure 8.14. For comparison, some examples of sound-speed anomaly versus frequency at different depths are plotted in Figure 8.15. .

Figure 8.11 Sound-speed anomaly at different depths. Wind speed= 17m/s .
 Dars1: 1.4m ; Dars2: 3.2m ; Dars3: 0.5m .

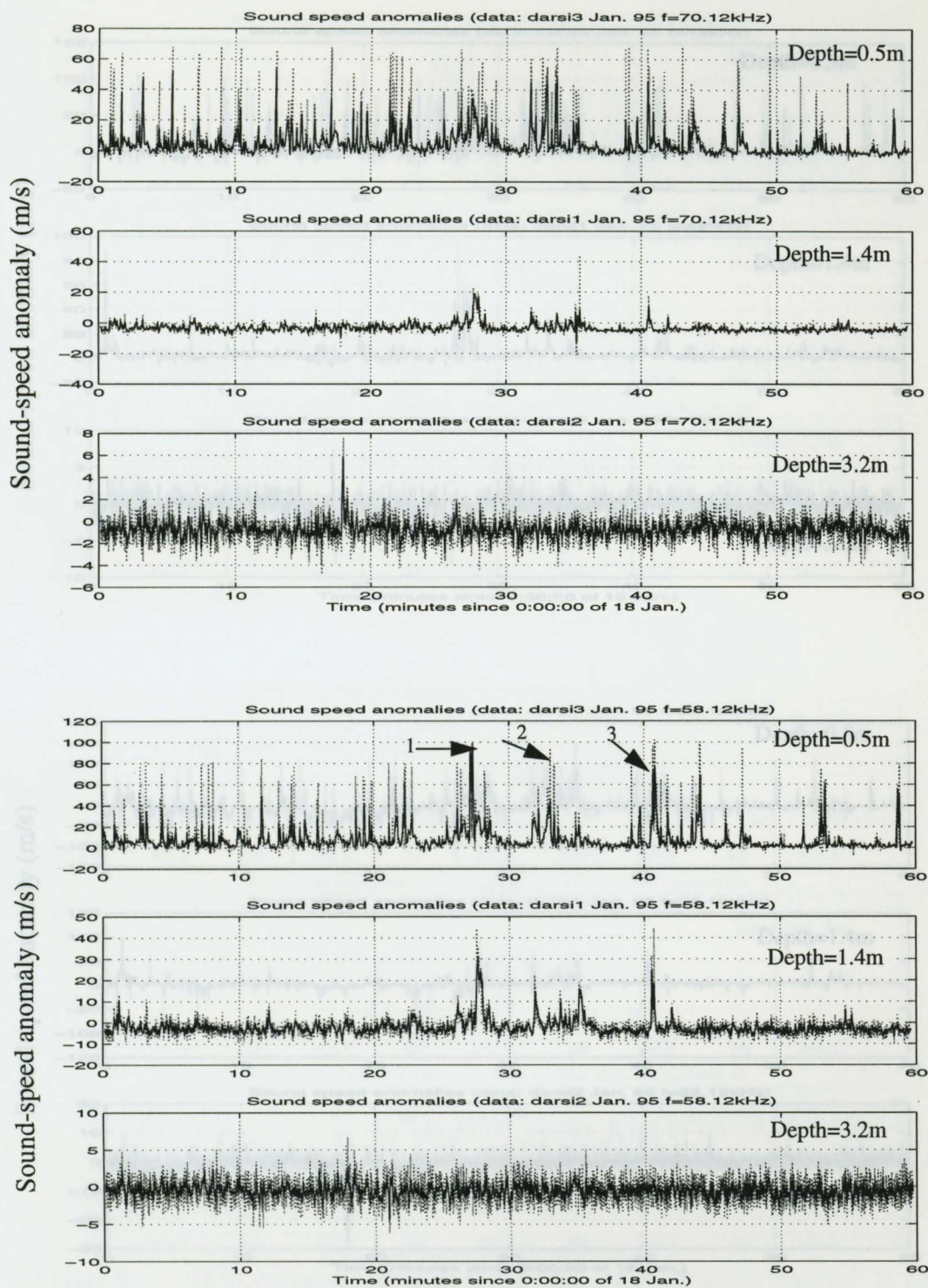


Figure 8.11 Sound-speed anomaly at different depths. Wind speed=17m/s.
Darsi1:1.4m; Darsi2: 3.2m; Darsi3: 0.5m.

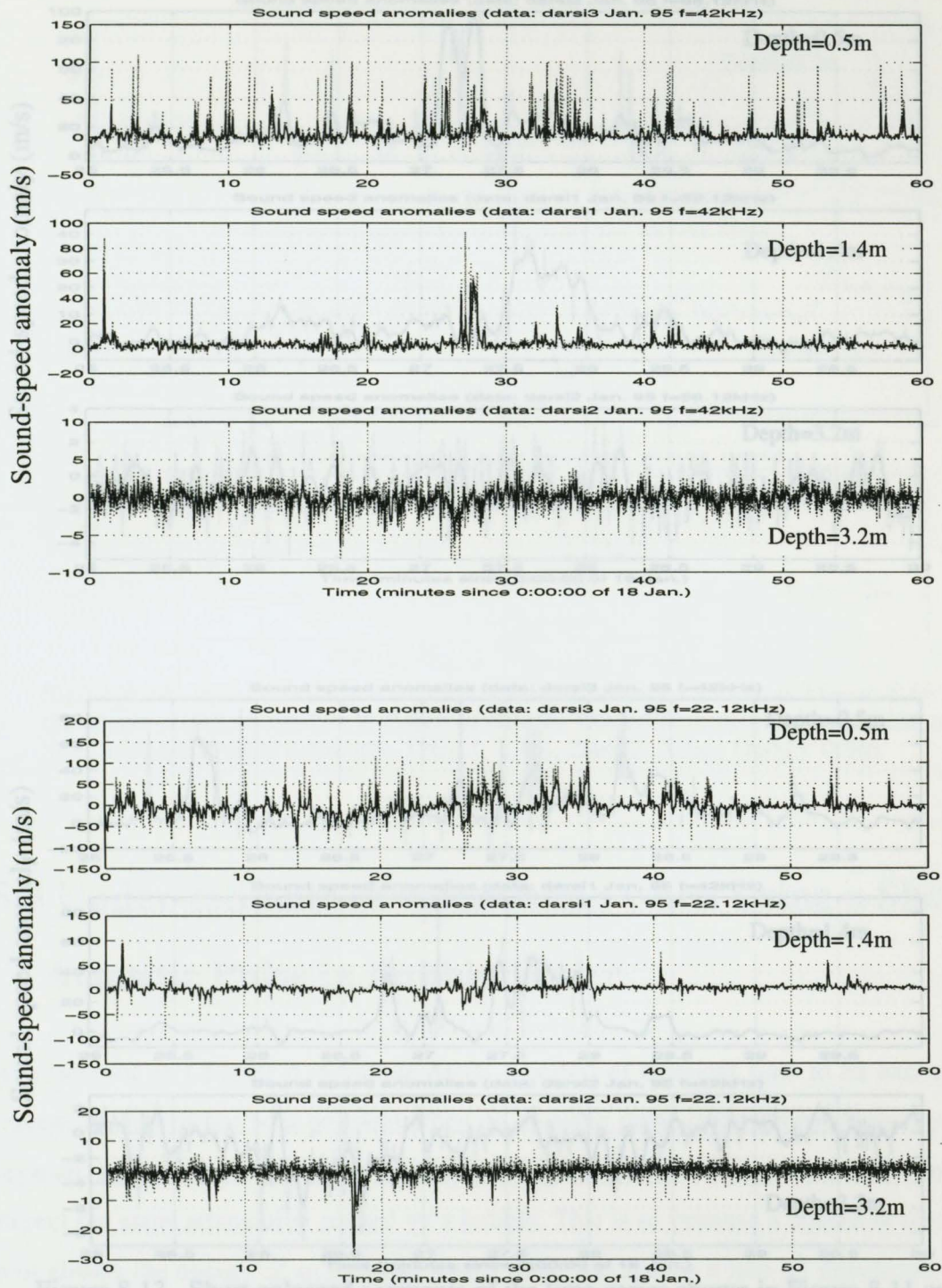


Figure 8.12 Sound-speed anomaly at different depths. Wind speed=17m/s.
Darsi1: 1.4m; Darsi2: 3.2m; Darsi3: 0.5m.

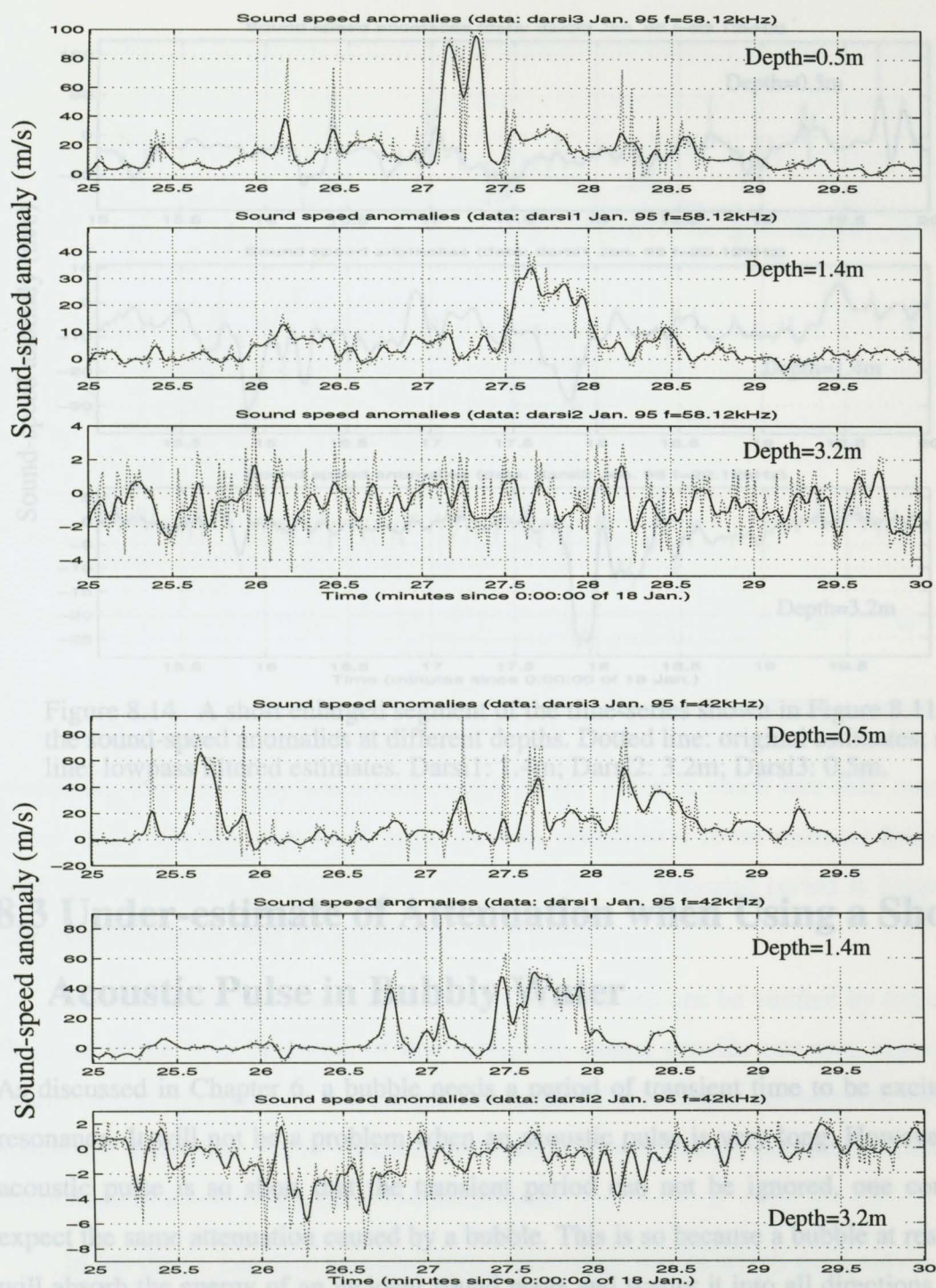


Figure 8.13 Short enlarged segments of the time-series shown in Figure 8.11 and Figure 8.12. Dotted line: original estimates; solid line: lowpass filtered estimates. Darsi1: 1.4m; Darsi2: 3.2m; Darsi3: 0.5 m.

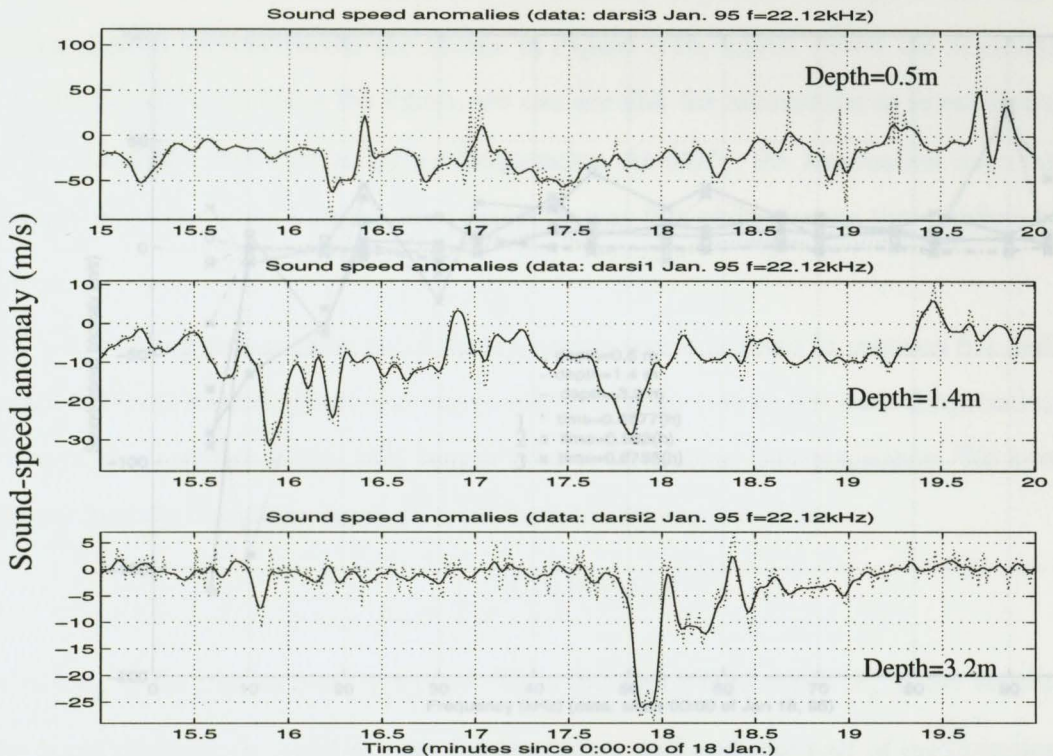


Figure 8.14 A short enlarged segment of the time-series shown in Figure 8.11 for the sound-speed anomalies at different depths. Dotted line: original estimates; solid line: lowpass filtered estimates. Darsi1: 1.4m; Darsi2: 3.2m; Darsi3: 0.5m.

8.3 Under-estimate of Attenuation when Using a Short

Acoustic Pulse in Bubbly Water

As discussed in Chapter 6, a bubble needs a period of transient time to be excited into resonance. It will not be a problem when an acoustic pulse is very long. However, if an acoustic pulse is so short that the transient period can not be ignored, one could not expect the same attenuation caused by a bubble. This is so because a bubble at resonance will absorb the energy of an incident sound wave and scatter it into all directions, which causes a major energy loss of a sound wave during propagation. While a bubble is not at

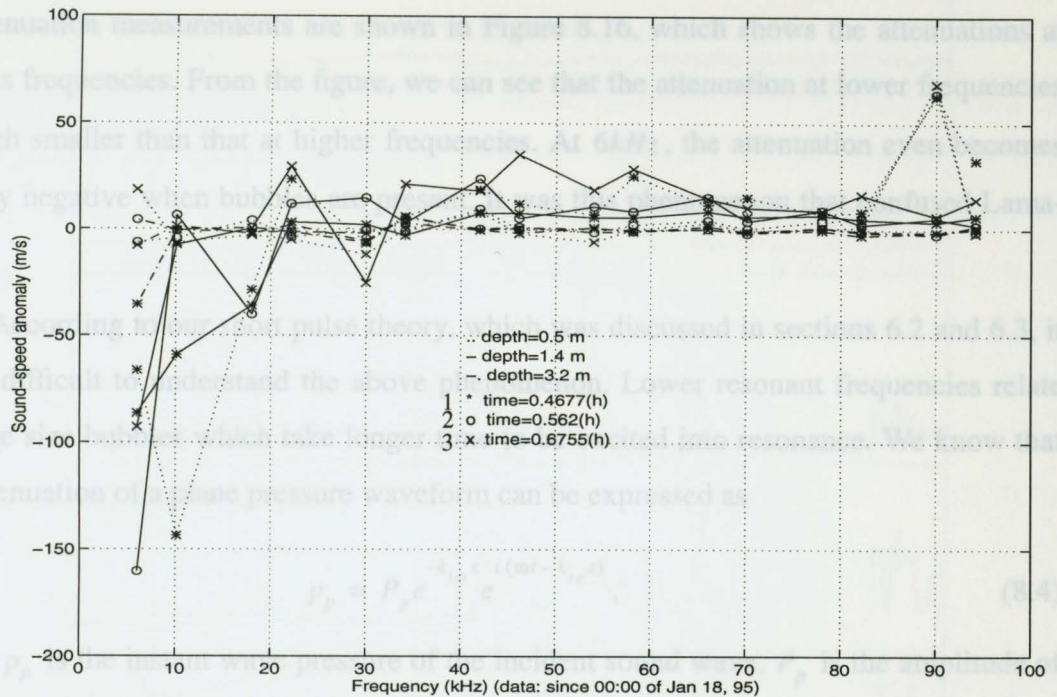


Figure 8.15 Sound-speed anomaly versus frequency at different depths (the events refer to Figure 8.11).

resonance, there are only some back-scatter losses which is much less than omnidirectional scatter. On the other hand, larger bubbles, which have lower resonant frequencies, need more energy to be excited into resonance. So, the transient period is longer for a low frequency pulse than for a high frequency pulse.

Above theory has been introduced in Chapter 6 and can be verified by experiment. Because of the time limitation of this thesis, we cannot provide our own experimental results here at this moment. But one good example of field results can be given here, from Lamarre's thesis [20, 21] in which he was puzzled by a strange phenomenon about the attenuation of sound propagation in bubble water.

In his thesis, Lamarre provided some attenuation results which were obtained from processing the data acquired near the coast of Woods Hole, Massachusetts in November 1992. The data were acquired at a depth of 0.5m, and the wind speed was 8m/s. A short

acoustical pulse was used in the experiment. The pulse length was about 2–3 cycles of the lowest frequency pulse, which was about 0.5ms as presented in his thesis. His results of attenuation measurements are shown in Figure 8.16, which shows the attenuations at various frequencies. From the figure, we can see that the attenuation at lower frequencies is much smaller than that at higher frequencies. At 6kHz, the attenuation even becomes slightly negative when bubbles are present. It was this phenomenon that confused Lamarre.

According to our short pulse theory, which was discussed in sections 6.2 and 6.3, it is not difficult to understand the above phenomenon. Lower resonant frequencies relate to large size bubbles which take longer time to be excited into resonance. We know that the attenuation of a plane pressure waveform can be expressed as

$$p_p = P_p e^{-k_{im}x} e^{i(\omega t - k_{re}x)}, \quad (8.4)$$

where p_p is the instant wave pressure of the incident sound wave, P_p is the amplitude of the wave pressure, k_{im} and k_{re} are the imaginary part and real part of the complex wave number. By using Eq. (6.37) and Eq. (8.4), the attenuation of the sound wave can be written as

$$Attenuation = e^{-k_{im}x} = e^{-\left(k_0 \frac{B}{2}\right)\theta x}. \quad (8.5)$$

Eq. (8.5) can be further written in logarithm and absolute value,

$$Attenuation (dB) = \left(k_0 \frac{B}{2} x \cdot 10 \log e\right) \theta. \quad (8.6)$$

To explain more explicitly, we plot the transient factor θ (see Eqs. 6.33, 6.36, 6.37) in Figure 8.17 with the same frequencies as those in Lamarre's attenuation plots. The transient factors at 500 μ s for those frequencies are also listed in Table 8.1. From Figure

Frequency	40 kHz	30 kHz	25 kHz	20 kHz	15 kHz	10 kHz	6 kHz
Transient factor	0.9942	0.9699	0.9348	0.8678	0.7490	0.5520	0.3360

Table 8.1. Frequency and transient factor.

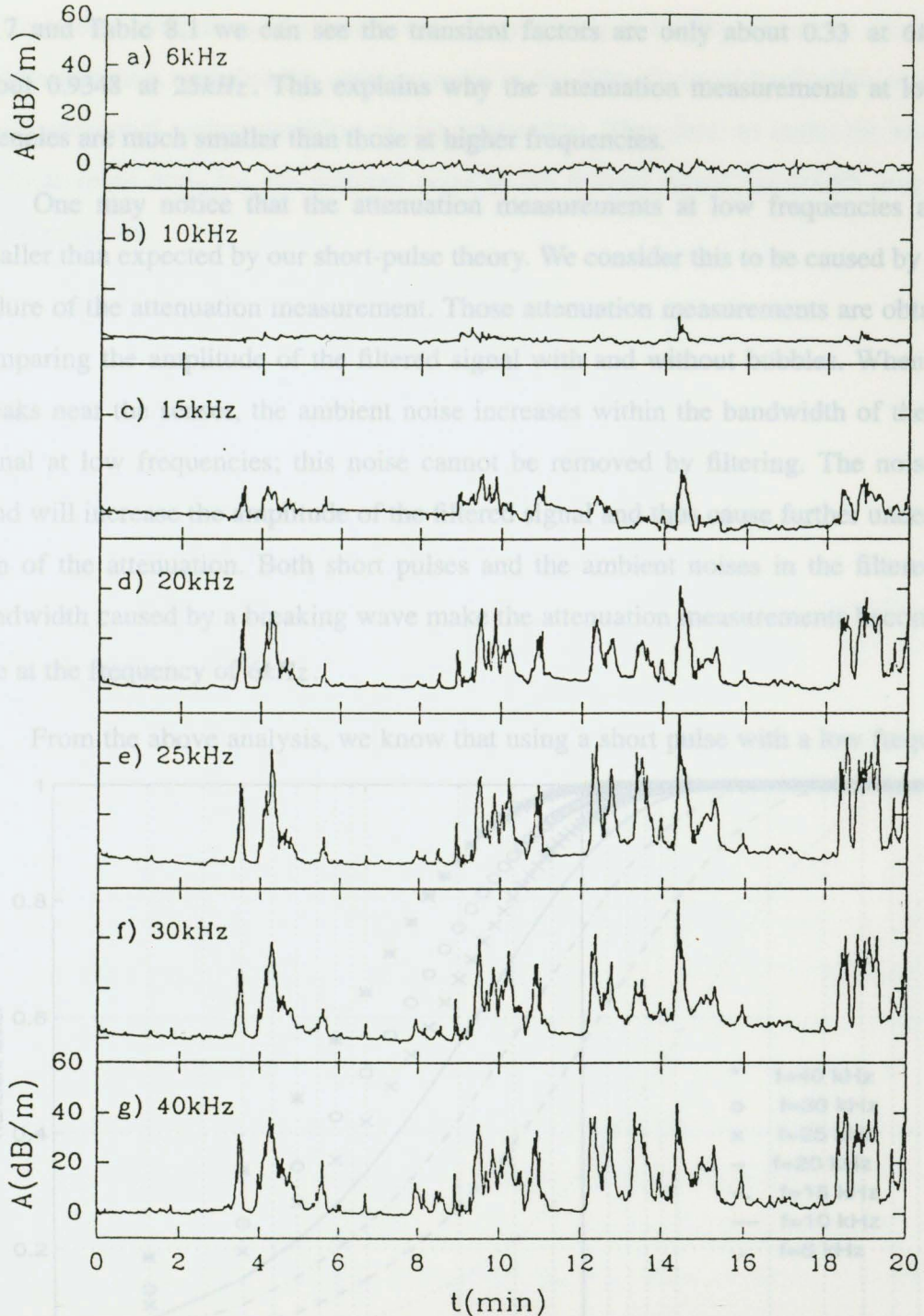


Figure 8.16 Attenuation at various frequencies obtained by band-pass filtering a 20 min. record of composite pulse data acquired at a depth of 0.5 m. The various band-pass frequencies are indicated on the plots. The wind speed and the SWH were 8 m/s and 0.46 m, respectively. From Lamarre's thesis [20].

8.17 and Table 8.1 we can see the transient factors are only about 0.33 at 6kHz and about 0.9348 at 25kHz . This explains why the attenuation measurements at lower frequencies are much smaller than those at higher frequencies.

One may notice that the attenuation measurements at low frequencies are even smaller than expected by our short-pulse theory. We consider this to be caused by the procedure of the attenuation measurement. Those attenuation measurements are obtained by comparing the amplitude of the filtered signal with and without bubbles. When a wave breaks near the sensor, the ambient noise increases within the bandwidth of the filtered signal at low frequencies; this noise cannot be removed by filtering. The noise in the band will increase the amplitude of the filtered signal and thus cause further underestimation of the attenuation. Both short pulses and the ambient noises in the filtered signal bandwidth caused by a breaking wave make the attenuation measurements become negative at the frequency of 6kHz .

From the above analysis, we know that using a short pulse with a low frequency to

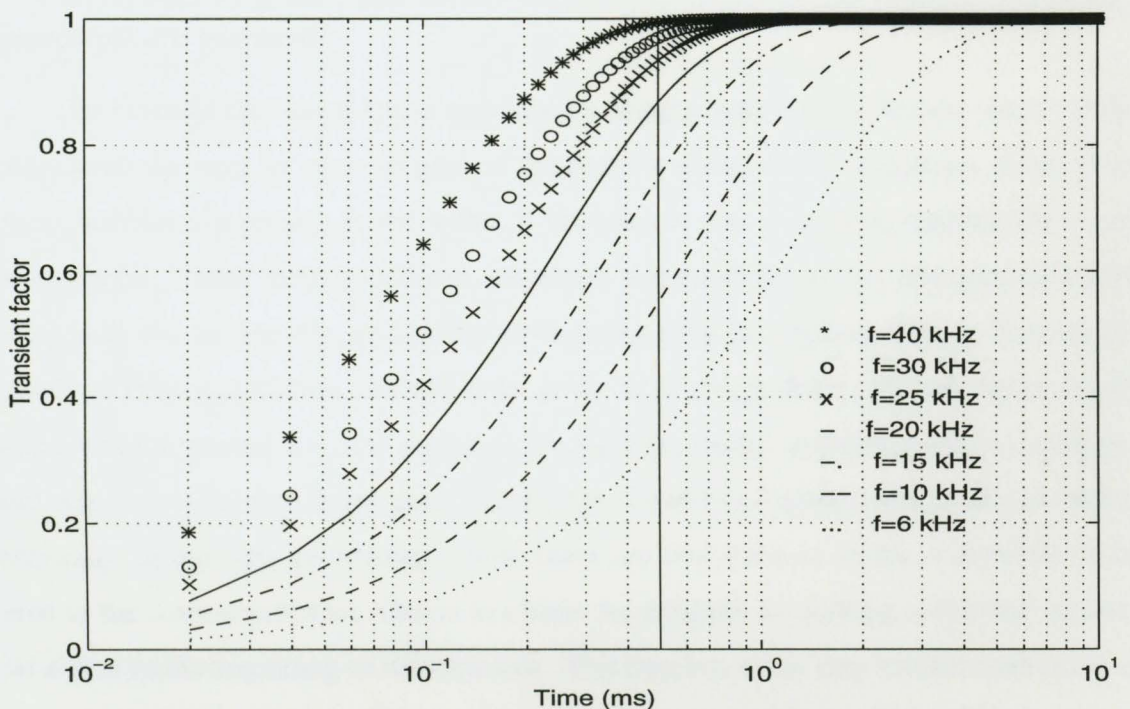


Figure 8.17 Transient factor versus transient time at different frequencies.

estimate the attenuation of a sound wave propagating in bubbly water can cause serious underestimation, and that the ambient noise in the filtered signal bandwidth could cause some additional underestimation of the attenuation. Therefore, to make the attenuation estimate more accurate, the ambient noise in the filtered signal bandwidth may need to be investigated.

Conclusions and Future Work

9.1 Summary and Conclusions

This thesis undertakes part of the work of developing a novel spectroscopy of an acoustical resonator sensor and a sound-speed sensor. The newly-developed sound-speed measurement sensor provides a very useful tool for acquiring sound speed estimates. To measure sound speeds at different frequencies simultaneously, an omnidirectional multi-frequency pulse is proposed.

To estimate the sound-speed anomaly by using a sound-speed sensor, some careful considerations must be taken to process the data for sound-speed estimation. *First*, when many bubbles are present in the water, it becomes a very dispersive medium for sound propagation. Under these conditions, envelope cross-correlation for determination time delay will not be feasible, and phase unwrapping must be applied. This is because the envelope cross-correlation method only gives us a group delay. *Second*, under rough ocean conditions and with the sensor at the shallow depths, ambient noise is significant and will cause a higher-order trend in our data. Therefore, higher-order trend removal is necessary in our data processing. *Third*, there are two ways to obtain a template to be used in the cross-correlation. One is to obtain the template by shifting a detected acoustical signal to the beginning of the time axis. This requires some very careful calibration to estimate the real beginning of the template. Another approach is to obtain a template from a computer generated electrical signal. This signal must pass through all the electronic

paths that a received signal will pass through to avoid any extra delay introduced by the system. When the time delay is approximately known, as in the laboratory calibration, the resolution of a delay estimate can be improved further by windowing the received sig-

Chapter 9

As one of the most important contributions of this thesis, a clear analysis has been made on the propagation of a short acoustical pulse in bubbly water. The analysis concludes that there will be an underestimate of sound-speed anomaly in bubbly water when a steady-state complex equation [27] is applied to a very short acoustical pulse. The ratio of the underestimation caused by a short pulse is given. Our short-pulse theory is verified

Conclusions and Future Work

9.1 Summary and Conclusions

This thesis undertakes part of the work of developing a novel system consisting of an acoustical resonator sensor and a sound-speed sensor. The newly developed sound-speed measurement sensor provides a very useful tool for acquiring sound-speed estimates. To measure sound speeds at different frequencies simultaneously, an optimized multi-frequency pulse is proposed. Besides presenting a series of laboratory tests of the instrumentation, a successful field experiment is reported, in which our newly developed instrument was used. The data acquired during the experiment are carefully analyzed.

To estimate the sound-speed anomaly by using a sound-speed sensor, some careful considerations must be taken to process the data for sound-speed estimation. *First*, when many bubbles are present in the water, it becomes a very dispersive medium for sound propagation. Under these conditions, envelope cross-correlation for determination time delay will not be feasible, and phase unwrapping must be applied. This is because the envelope cross-correlation method only gives us a group delay. *Second*, under rough ocean conditions and with the sensor at the shallow depths, ambient noise is significant and will cause a higher-order trend in our data. Therefore, higher-order trend removal is necessary in our data processing. *Third*, there are two ways to obtain a template to be used in the cross-correlation. One is to obtain the template by shifting a detected acoustical signal to the beginning of the time axis. This requires some very careful calibration to estimate the real beginning of the template. Another approach is to obtain a template from a computer generated electrical signal. This signal must pass through all the electronic

paths that a received signal will pass through to avoid any extra delay introduced by the system. When the time delay is approximately known, as in the laboratory calibration, the resolution of a delay estimate can be improved further by windowing the received signal in the time domain.

As one of the most important contributions of this thesis, a clear analysis has been given on the propagation of a short acoustical pulse in bubbly water. The analysis concludes that there will be an underestimate of sound-speed anomaly in bubbly water when a steady-state complex equation [27] is applied to a very short acoustical pulse. The ratio of the underestimation caused by a short pulse is given. Our short-pulse theory is verified by a good field experimental example given from the attenuation measurements in Lamarre's thesis [20, 21]. The analysis of this example also tells us that the ambient noise from breaking waves could increase the amplitude of the filtered signal used to compare the signal obtained in bubble-free water and thus will cause further underestimation of the sound attenuation.

Besides presenting a series of laboratory tests of the instrumentation, a successful field experiment is reported, in which our newly developed instrument was used. The data acquired during the experiment are carefully processed and analyzed. The results obtained from both sensors are compared, which shows very good consistency. From the results we know that sound-speed anomalies not only depend on depth and time but also on frequency. A turnover frequency, which implies the peak in bubble population when the sound-speed anomalies turn from positive to negative, is also depth and wind-speed dependent. Large wind speeds cause more and larger breaking waves and thus entrain more bubbles into the water. The fast rising large-size bubbles make the turnover frequencies lower in shallower water than in deeper water. Further, the short-pulse theory is verified by some field results.

9.2 Suggestions for Future Work

This thesis has led us to the following considerations regarding future work.

First, the short-pulse theory is helpful to improve the accuracy of bubble-size distribution estimations from the sound-speed sensor. As pointed out in this thesis, with our current pulse length, the short-pulse theory should be applied to frequencies below 25kHz to observe the effect of the transient process on the sound-speed anomaly and attenuation. Since a resonator sensor uses a long pulse acoustical technique, it would be interesting to compare the sound-speed anomaly and the attenuation from a sound-speed sensor with those from a resonator sensor at a lower frequency to observe their differences and thus further verify the short-pulse theory.

Second, as analyzed in the thesis, ambient noises from breaking waves within filtered signal bandwidth could increase the amplitude of the filtered signal, thus adding some bias to the estimation of the amplitude of the filtered signal. To further improve the attenuation estimate from a sound-speed sensor, ambient noise from breaking waves should be investigated to correct the estimation bias of the amplitude of a received signal.

Finally, based on the correctly estimated sound-speed anomalies and attenuations, bubble-size distributions could be inferred, which would be the most interesting and important work to be done next.

- [5] Julius S. Bendat and Allan G. Piersol. *Random Data Analysis and Measurement Procedures*. John Wiley & Sons, Inc., New York 1986.
- [6] D.C. Bachuber and A.H. Woodcock. Bubble formation and modification in the sea and its meteorological significance. *Tellus*, 9:145-148, 1957.
- [7] Siu-Kay Chow and Peter M. Schultheiss. Delay Estimation Using Narrow-Band Processes. *IEEE Trans. ASSP-29*, No. 3, 478-484, June 1981.
- [8] Clarence S. Clay and Herman Medwin. *Acoustical Oceanography: principles and applications*. Wiley-Interscience, USA, 1977.
- [9] Charles Jr. Devin. Survey of thermal, radiation and viscous damping of pulsating air bubbles in water. *The Journal of the Acoustical Society of America*, Vol. 31, No. 12:1654-1667, 1959.

Bibliography

- [1] V. A. Akulichev, V. A. Bulanov and S. A. Klenin. Acoustic Sensing of gas bubbles in the ocean medium. *Sov. Phys. Acoust.* 32(3), 177-180, May-June 1986.
- [2] Andreas Antoniou. *Digital Filters: Analysis and Design*. McGraw-Hill, Inc. New York, 1979.
- [3] S. Baldy. Bubbles in the close vicinity of breaking waves: Statistical characteristics of the generation and dispersion mechanism. *Journal of Geophysical Research*, 93:8239-8248, 1988.
- [4] Nigel Breitz and Herman Medwin. Instrumentation for in situ acoustical measurements of bubble spectra under breaking waves. *The Journal of the Acoustical Society of America*, 86(2):739-743, August 1989.
- [5] Julius S. Bendat and Allan G. Piersol. *Random Data Analysis and Measurement Procedures*. John Wiley & Sons, Inc., New York 1986.
- [6] D.C. Bachuber and A.H. Woodcock. Bubble formation and modification in the sea and its meteorological significance. *Tellus*, 9:145-148, 1957.
- [7] Siu-Kay Chow and Peter M. Schultheiss. Delay Estimation Using Narrow-Band Processes. *IEEE Trans. ASSP-29*, No. 3, 478-484, June 1981.
- [8] Clarence S. Clay and Herman Medwin. *Acoustical Oceanography: principles and applications*. Wiley-Interscience, USA, 1977.
- [9] Charles Jr. Devin. Survey of thermal, radiation and viscous damping of pulsating air bubbles in water. *The Journal of the Acoustical Society of America*, Vol. 31, No.12:1654-1667, 1959.

- [10] David M. Farmer and David D. Lemon. The influence of bubbles on ambient noise in the ocean at high wind speeds. *Journal of Physical Oceanography*, Vol. 14, 1762-1778, November 1984.
- [11] David M. Farmer and Svein Vagle. On the determination of Breaking surface wave distributions using ambient sound. *Journal of Geophysical Research*, Vol. 93, No. C4, 3591-3600, April 1988.
- [12] Francis E. Fox, Stranley R. Curley, and Glenn S. Larson. Phase velocity and absorption measurements in water containing air bubbles. *The Journal of the Acoustical Society of America*, 27 No.3:534-539, 1955.
- [13] Frederick W. Gibson. Measurement of the effect of air bubbles on the speed of sound in water. *The Journal of the Acoustical Society of America*, 48 No.5 (part:2):1195-1197, 1970.
- [14] V.A.Del Grosso and C.W. Mader. Speed of sound in pure water. *The Journal of the Acoustical Society of America*, 52:1442-1446, 1972.
- [15] C. Guy Suits. *The collected works of Irving Langmuir with contributions in memoriam including a complete bibliography of his works*. Pergamon Press. New York, 1962
- [16] Irving Langmuir. Surface motion of water induced by wind. *Science*, Vol. LXXXVII, No. 2250, 119, February (1938)
- [17] B.D. Johnson and R.C. Cooke. Bubble populations and spectra in coastal water: a photographic approach. *Journal of Geophysical Research*, 84:3761-3766, 1979.
- [18] Charles H. Knapp and G. Clifford Carter. The generalized correlation method for estimation of time delay. *IEEE Trans. ASSP-24*, No. 4, 320-327, August 1976.
- [19] Kolobayev. Investigation of the concentration and statistical size distribution of wind-produced bubbles in the near-surface ocean. *Oceanology*, Engl. Transl., 15:659-661, 1976.

- [20] Eric Lamarre. *An experimental study of air entrainment by breaking Wave*. Ph.D. thesis, MIT, Cambridge, Massachusetts, USA, June 1993.
- [21] Eric Lamarre and W.K. Melville. Sound-speed measurements near the ocean surface. *The Journal of the Acoustical Society of America*, 96(6): 3605-3616, Dec. 1994.
- [22] Haibo Ma. *Multi-Directional Search Method with Quadratic Model*. M.A.Sc. thesis, University of Victoria, Victoria, B.C., Canada, 1993.
- [23] Herman Medwin and Nigel Breitz. Ambient and transient bubble spectral densities in quiescent seas and under spilling breakers. *Journal of Geophysical Research*, Vol. 94, No.C9, 12,751-12,759. Sept. 1989.
- [24] Herman Medwin. In situ acoustic measurements of bubble populations in coastal ocean waters. *Journal of Geophysics*, 75:599-611, 1970.
- [25] Herman Medwin. Speed of sound in water: A simple equation for realistic parameters. *The Journal of the Acoustical Society of America*, 58:1318-1319, December 1975.
- [26] Herman Medwin. Acoustical determinations of bubble-size spectra. *The Journal of the Acoustical Society of America*, 62, No.4:1041-1044, 1977.
- [27] Herman Medwin. Counting bubbles acoustically: a review. *Ultrasonics*, January:7-13, 1977.
- [28] Herman Medwin. In situ acoustic measurements of microbubbles at sea. *Journal of Geophysical Research*, 82, No.6:971-975, 1977.
- [29] T.J. O'hearn, L.d'Agostino, and S.J. Acosta. Comparison of holographic and coulter counter measurements of cavitation nuclei in the ocean. *Journal of Fluids Engineering*, 110:200-207, 1988.
- [30] Alan V. Oppenheim and Ronald W. Schafer. *Digital Signal Processing*. Prentice-Hall, Inc., Englewood Cliffs, New Jersey, 1975.

- [31] Azizul H. Quazi. An overview on the time delay estimate in active and passive systems for target location. *IEEE Trans. ASSP-29*, No. 3, 527-533, June 1981.
- [32] Edward Silberman. Sound velocity and attenuation in bubbly mixtures measured in standing wave tubes. *The Journal of the Acoustical Society of America*, 29 No.8:925-933, 1957.
- [33] M.Strasberg. Gas bubbles as sources of sound in liquids. *The Journal of the Acoustical Society of America*, 28 No. 1:20-26, 1955.
- [34] S. A. Thorpe. Bubble clouds and the dynamics of the upper-ocean. *Q. J. R. Meteorol. Soc.* 118, 1-22, 1992.
- [35] Svein Vagle. *An Acoustic Study of the upper-ocean boundary layer*. Ph.D. thesis, University of Victoria & Institute of Ocean Science, B.C., Canada, Aug 1989.
- [36] Svein Vagle and David M. Farmer. The measurement of bubble-size distribution by acoustical backscatter. *Journal of Atmospheric and Oceanic Technology*, 9:630-644, 1992.
- [37] R.Wildt. Physics of sound in the sea. *Summary Technical Report of Div. 6 N.D.R.C, Washington, D.C.*, Vol.8, Chpt.28:460-477, 1946.
- [38] A.L.Walsh and M.J. Mulhern. Photographic measurements of bubble populations from breaking wind waves at sea. *Journal of Geophysical Research*, 92:14553-14565, 1987.
- [39] A.B.Wood. *A text book of sound*. G.Bell & Son, 1941.
- [40] Jin Wu. Bubble populations and spectra in near-surface ocean: summary and review of field measurements. *Journal of Geophysical Research*, 86:457-463, 1981.

VITA

Surname: Mao Given Names: Victor Yi-Xin

Place of Birth: Shanghai, China Date of Birth: _____

Educational Institutions Attended:

Shanghai Jiao Tong University. 1978 to 1982

Degrees Awarded: Dissertation: A Comparison of Two Acoustic Techniques for

B. Eng. Measurement of Bu Shanghai Jiao Tong University Oct 1982

Honours and Awards:

The Third Class Award for Science and Technology Advancement issued by the Chinese National Shipbuilding Industry Corporation in 1988.

The Excellent New Product Design Award issued by Shanghai Municipality (P.R. China)

Sept 29 1985
(Date)

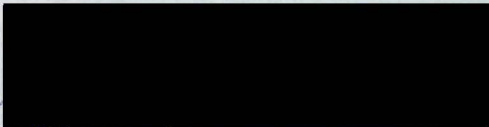
Publications:

Partial Copyright License

I hereby grant the right to lend my thesis (or dissertation) to users of the University of Victoria Library, and to make single copies only for such users or in response to a request from the Library of any other university, or similar institution, on its behalf or for one of its users. I further agree that permission for extensive copying of this thesis for scholarly purposes may be granted by me or a member of the University designated by me. It is understood that copying or publication of this thesis for financial gain shall not be allowed without my written permission.

Title of Thesis/Dissertation: **A Comparison of Two Acoustic Techniques for the Measurement of Bubble Distributions in the Ocean**

Author


(Signature)

Victor Yi-Xin Mao

(Name in Block Letters)

Sept 29 / 95
(Date)